UNIVERSIDADE ESTADUAL DE CAMPINAS

FACULDADE DE ENGENHARIA ELÉTRICA E DE COMPUTAÇÃO

EDNA MARINA DE SOUZA

DEVELOPMENT OF A PHANTOM FOR QUALITY CONTROL OF DIFFUSION TENSOR IMAGES

DESENVOLVIMENTO DE UM PHANTOM PARA CONTROLE DE QUALIDADE DE IMAGENS DO TENSOR DE DIFUSÃO

CAMPINAS

2017

UNIVERSIDADE ESTADUAL DE CAMPINAS
FACULDADE DE ENGENHARIA ELÉTRICA E DE COMPUTAÇÃO

EDNA MARINA DE SOUZA

DEVELOPMENT OF A PHANTOM FOR QUALITY CONTROL OF DIFFUSION TENSOR IMAGES

Orientadora: Profa. Dra. Gabriela Castellano
Coorientador: Prof. Dr. Eduardo Tavares Costa

DESENVOLVIMENTO DE UM PHANTOM PARA CONTROLE DE QUALIDADE DE IMAGENS DO TENSOR DE DIFUSÃO

Doctorate thesis presented to the Electrical Engineering Postgraduation Program of the School of Electrical and Computer Engineering of the University of Campinas to obtain the Ph.D. grade in Electrical Engineering. Concentration area: Biomedical Engineering.

Tese de Doutorado apresentada ao Programa de Pós-Graduação em Engenharia Elétrica da Faculdade de Engenharia Elétrica e de Computação da Universidade Estadual de Campinas para obtenção do título de Doutora em Engenharia Elétrica. Área de concentração: Engenharia Biomédica.

ESTE EXEMPLAR CORRESPONDE À VERSÃO FINAL DA TESE
DEFENDIDA PELA ALUNA EDNA MARINA DE SOUZA,
E ORIENTADA PELA PROFA. DRA. GABRIELA CASTELLANO

_____

CAMPINAS
2017

Informações para Biblioteca Digital

Título em outro idioma: Desenvolvimento de um phantom para controle de qualidade de imagens do tensor de difusão
Palavras-chave em inglês:
Magnetic resonance imaging
Diffusion tensor imaging
Quality control
Diffusion
Medical imaging
Área de concentração: Engenharia Biomédica
Titulação: Doutor em Engenharia Elétrica
Banca examinadora:
Gabriela Castellano [Orientador]
Letícia Rittner
José Wilson Magalhães Bassani
Antônio Adilton Oliveira Carneiro
Diana Rodrigues de Pina Miranda
Data de defesa: 22-02-2017
Programa de Pós-Graduação: Engenharia Elétrica

COMISSÃO JULGADORA – TESE DE DOUTORADO

Candidata: Edna Marina de Souza

Data da defesa: 22 de fevereiro de 2017

Título da Tese: "Development of a Phantom for Quality Control of Diffusion Tensor Images"

Profa. Dra. Gabriela Castellano (presidente, IFGW-UNICAMP)

Prof. Dr. Antônio Adilton Oliveira Carneiro (FFCLRP-USP)

Profa. Dra. Diana Rodrigues de Pina Miranda (FMB-UNESP)

Profa. Dra. Letícia Rittner (FEEC-UNICAMP)

Prof. Dr. José Wilson Magalhães Bassani (FEEC-UNICAMP)

A ata da defesa, com as respectivas assinaturas dos membros da Comissão Julgadora, encontra-se no processo de vida acadêmica da aluna.

DEDICATION

To God and my family. My mother, Maria Cristina de Souza, my aunt Maria Joana de Souza (in memoriam) and my grandparents Osvaldo de Souza (in memoriam) and Zilda Pires de Souza (in memoriam), that always allow me to dream with this moment and gave me the basis to be who I am and to look for what I want to live and learn.

ACKNOWLEDGMENTS

First of all, I would like to thank Prof. Dr. Gabriela Castellano for her guidance, incentive, friendship and patience in this journey. Prof. Dr. Eduardo Tavares Costa for his friendship, and always encourage me in this project, at work and life. Their supervision and support were decisive to complete this thesis.

Many thanks to Prof. Dr. Fernando Cendes and all team of CEPID BRAINN - UNICAMP for all structure and support to imaging acquisitions. Many thanks to Renato Moura and Mauro Martinazzo, from Biomedical Engineering Centre of UNICAMP, that spent many hours of work to build the devices projected and applied in the study. Thanks to professors and workers of Biomedical Engineering Department of School of Electrical and Computer Engineering, UNICAMP, for show me what is Biomedical Engineering and allow me to develop my research.

Special thanks to Sergio Brunetto, a great supervisor, friend and professor, for all the knowledge that he has shared in the field of medical images, as well as his comprehension when I had to do my experiments and other activities to reach this graduation. Thanks to all students and friends of Medical Physics Area of Biomedical Engineering Center, UNICAMP, a place where I found structure to learn more day-to-day, improving my knowledge and life experience.

After all, I would like to thank my mother Cristina for her support all over these years of study, care, motivation, comprehension and unconditional love that always have brought me back to road when I feel lost.

CNPq and FAPESP for funding support.

ABSTRACT

Diffusion-weighted imaging (DWI) and diffusion tensor imaging (DTI) combine magnetic resonance imaging (MRI) techniques and diffusion measures. In DWI, the contrast is defined by the microscopic motion of water protons. Nowadays, DWI has become important for early diagnose of acute stroke. DT images are calculated from DW images acquired in at least six directions, which give information of diffusion directionality, making it possible to reconstruct axonal or muscle fiber images. Both techniques have been applied to study body structures in healthy and pathological conditions. Currently, it is known that these images and derived parameters are quite sensitive to factors related to acquisition and processing. Magnetic field non-homogeneity, susceptibility, chemical shift, radiofrequency (RF) interference, eddy currents and low signal-to-noise ratio (SNR) can have a more harmful effect in diffusion data than in T1- or T2-weighted image data. However, even today there are no standard phantoms or protocols for DWI or DTI quality control (QC). The aim of this work was to build a low-cost multipurpose DTI phantom to evaluate parameters that can compromise the quality of DTI data. Different fishing lines and setups were tested to define the kind of fibers to be used. Subsequently, a multipurpose phantom was developed and tested. We found that Dyneema® fishing lines are the best option to build the phantom. Dyneema® fishing lines bundles have FA values similar to those found in the main brain tracts and do not compromise other MRI QC measurements. Our tests showed that the multipurpose phantom built is stable and can be used for QC in clinical routine.

Keywords*: Magnetic Resonance Imaging, Diffusion Tensor Imaging, Multipurpose Phantom, Quality Control.*

RESUMO

Imagens de ressonância magnética ponderadas por difusão (imagens DW) e imagens do tensor de difusão (imagens DT) combinam técnicas de ressonância magnética (MRI) e medidas de difusão. Nas imagens DW, o contraste é definido pelo movimento microscópico dos prótons de água. Atualmente, imagens DW tornaram-se populares em função de sua capacidade de detectar o AVC ainda na fase aguda. As imagens DT são calculadas a partir de imagens DW adquiridas em pelo menos seis direções, fornecendo informações de direcionalidade de difusão e tornando assim possível a reconstrução de imagens de fibras axonais ou musculares. Ambas as técnicas têm sido aplicadas ao estudo das estruturas corporais em condições saudáveis e patológicas. Atualmente, sabe-se que essas imagens e seus parâmetros são bastante sujeitos a fatores relacionados à aquisição e processamento. Heterogeneidades do campo magnético, suscetibilidade, deslocamento químico, interferência de radiofrequência (RF), correntes parasitárias e a razão sinal/ruído (SNR) têm efeitos mais nocivos em imagens DW do que em imagens ponderadas em T1 ou T2. No entanto, ainda hoje não existem phantoms ou protocolos padrão para controle de qualidade (QC) de imagens DW ou DT. Assim, o objetivo deste trabalho foi construir um phantom multipropósito, de baixo custo, para o QC de imagens DT. Diferentes linhas de pesca e configurações foram testadas para definir o tipo de fibras a ser usado. Em seguida, um phantom multipropósito foi desenvolvido e testado. Descobrimos que as linhas de pesca Dyneema® são a melhor opção para a construção do phantom. Os feixes obtidos a partir destas linhas têm valores de FA semelhantes aos encontrados nos tratos cerebrais principais e além disso não atrapalham outras medições de QC em MRI. O phantom multipropósito desenvolvido mostrou-se estável e pode ser usado para QC na rotina clínica.

Palavras-chave: Imagens de Ressonância Magnética, Imagens do Tensor de Difusão, Phantom Multipropósito, Controle de Qualidade.

LIST OF FIGURES

LIST OF TABLES

ACRONYMS

AAPM	American Association of Physicists in Medicine
ACR	American College of Radiology
CEB	Center of Biomedical Engineering
CNR	Contrast-to-Noise Ratio
CL	Linearity
CT	Computed Tomography
CP	Planarity
CS	Sphericity
CV	Coefficient of Variation
DSI	Diffusion Spectral Imaging
DT	Diffusion Tensor
DTI	Diffusion Tensor Imaging
DTIi	DTI indexes
DW	Diffusion-Weighted
DWI	Diffusion-Weighted Imaging
EPI	Echo-Planar Imaging
FA	Fractional Anisotropy
FWHM	Full Width at Half Maximum
GM	Gray matter
HARDI	High Angular Resolution Diffusion Imaging
HASTE	Half-Fourier Acquisition Single-Shot Turbo Spin-Echo
HC	Clinics Hospital
LNI	Neuroimaging Laboratory
MD	Mean Diffusivity

MRI	Magnetic Resonance Imaging
NDGD	Number of Directions of Diffusion Gradients
NMR	Nuclear Magnetic Resonance
NSA	Number of Averages
PD	Proton Density
QC	Quality Control
RA	Relative Anisotropy
RF	Radiofrequency
S	Signal
SE	Spin-Echo
SENSE	Sensitivity Encoding
SNR	Signal-to-Noise Ratio
TE	Time of echo
TR	Time of repetition
UNICAMP	University of Campinas
VR	Volume Ratio
WM	White matter

CONTENTS

1 INTRODUCTION

Diffusion-weighted (DW) and diffusion tensor (DT) images have nowadays applications in many areas of medicine. However, there is no standard phantom and/or standard protocol for quality control (QC) of these kinds of images, as occurs for QC of proton density (PD), T1 and T2-weighted image acquisitions. Many studies have explored this subject in different ways and have brought useful information for QC for water diffusion-based images, given the need for standardization of multicenter/multiscanner studies and to obtain reliable data for diagnosis in clinical practice. However, there hasn't been agreement about the phantom to be used or the QC acquisition protocol to be applied to detect changes in these images before clinical data degradation.

Currently, it is known that DT images and their indexes are quite sensitive to factors related to imaging acquisition and processing. The reliability of results obtained from these images depends on the quality of the acquired data. Low SNR, patient motion during the scan, chemical shift, non-homogeneity of the magnetic field B_0, RF interference, eddy currents and magnetic susceptibility effects can degrade the quality of DW and DT images. Standard QC MRI phantoms, such as American College of Radiology (ACR) head or knee MRI phantoms, have diffusivities and relaxation parameters different from biological tissues and are isotropic. They can be helpful to follow parameters such as B_0 homogeneity, SNR, contrast-to-noise ratio (CNR), low-contrast structure detectability, uniformity, presence of ghost and distortions, slice thickness and spatial resolution of those images, but not for DTI QC. Furthermore, DW and DT images are more sensitive to bias compared to conventional MR images and consequently data corruption occurs first on these images. In other words, when a problem is detected on T1, T2 and PD images, probably DW and DT images are already much degraded.

Thinking about QC in MRI, considering the diversity of techniques available (diffusion, perfusion, functional images etc.), it is important to find methods and to develop devices that allow the quality of many different imaging techniques to be checked at once (that is, using the same device). To the best of our knowledge, this type of device did not exist before this work. Therefore, the main goals of this work were: 1) to develop a low-cost, DWI/DTI phantom, as well as a DWI/DTI QC protocol adaptable to the clinical and

research routines of MRI services, and 2) to improve the phantom, including modules to evaluation of parameters relevant to MRI acquisition techniques such as T1, T2 and PD-weighted images. The first phantom had modules to measure DTI indexes (DTIi); the phantom improved had, in addition to those, other modules, to measure spatial resolution, slice thickness, geometric distortion as well as SNR. A QC protocol for T1, T2, PD and DTI acquisitions using just one device is also proposed.

This thesis is organized as follows. Chapter 2 brings the theoretical background related to DWI and DTI and a literature review about phantoms for QC of these kinds of images. Chapter 3 describes the methodologies used in each part of the study, that comprised of the following steps:

1) Building an anisotropic diffusion phantom using Dyneema® fishing lines to simulate biological tracts and fibers, and application of this device to investigate how the acquisition parameters can change the DTIi, for 8-channel and 32-channel head coils.

2) Performance evaluation of different materials to compose the anisotropic diffusion phantom.

3) Proposition, building and test of a multipurpose DTI phantom to evaluate the performance of DTI acquisitions and spatial resolution, SNR, geometric distortions and slice thickness.

Chapter 4 describes and discusses the results reached. Finally, Chapter 5 summarizes the main achievements and conclusions from this research, pointing out the future research perspectives from these results. The last one summarizes the main and original contributions of this work that are listed below:

- The application of fishing lines to simulate brain tracts in the DTI phantom.
- The use of phantom developed to study the influence of the acquisition parameters on DTIi.
- The proposition of a multipurpose phantom to QC of DTI and evaluation of other scanner performance characteristics, as such as SNR, slice thickness and spatial resolution.

2 THEORETICAL BACKGROUND AND LITERATURE REVIEW

This chapter brings a background related to DWI and DTI and a review about the QC phantoms already proposed to evaluate the quality of data obtained from these techniques, highlighting their advantages and disadvantages.

2.1 DIFFUSION-WEIGHTED IMAGING AND DIFFUSION TENSOR IMAGING

DW images reveals microscopic characteristics of water molecules' diffusion across and between biological tissues (1). In these images, the contrast is based on molecular random motion of water protons. It is known that in biological tissues, diffusion can be isotropic (having same magnitude in all directions) or anisotropic (following a specific direction). The DWI acquisition involves the application of diffusion-weighting gradients in pulse sequences, creating a signal attenuation due to microscopic water protons' motion (2). Figure 2.1 shows the first pulse sequence designed for acquisition of these images.

Rectangular diffusion gradients applied before and after the 180º refocusing pulse have the same magnitude and duration. Thus, if all spins are coherently moving around the magnetic field of the scanner, they will have identical phase and there is no signal related to diffusion. On the other side, when water proton diffusion occurs, static and diffusing spins accumulate different phases, leading to a signal attenuation related to diffusion.
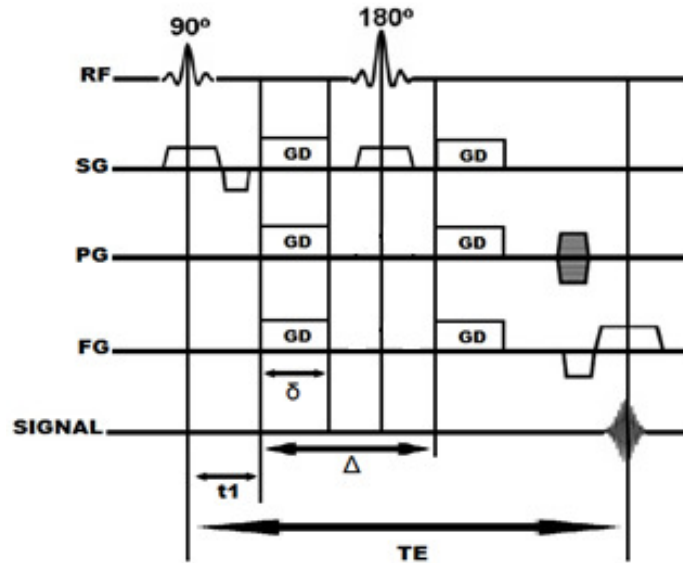
Figure 2.1 - Spin-Echo (SE) Pulse Sequence for DWI Acquisition. RF: radiofrequency; SG: slice selection direction gradient; PG: phase codification direction gradient; FG: frequency codification direction gradient; GD: diffusion-weighting gradient; δ: duration of GD; Δ: interval between application of two diffusion-weighting gradients; t1: time from application of RF excitation pulse to the first diffusion-weighting gradient; TE: echo time. The diffusion attenuation of the MRI signal is only dependent on GD, Δ and δ, but does not depend on t1.

In clinical practice, DWI showed its ability to detect acute stroke (when the symptoms begin) and classify it as ischemic or non-ischemic, while other imaging techniques just reveal brain changes hours after the onset (1). From DW images the Apparent Diffusion Coefficient (ADC) map and DT images can be obtained. ADC maps are so called because measured values are lower than those observed when free water diffusion occurs (without interference of compartments and barriers found in biological tissues). The ADC calculation is based on two DWI (DWI_i and DWI_0) obtained with same TE and different diffusion-sensitizing factors (b-values, which units are s/mm^2). In this case, TE should be long enough to be compatible with the duration of diffusion gradients, being the T2-weighted image commonly used. The Equation 2.1 shows how to calculate ADC values.

$$\text{ADC}_i = -\frac{1}{b_{\text{DWI}_i} - b_{\text{DWI}_0}} \ln \frac{\text{DWI}_i}{\text{DWI}_0}, \qquad (2.1)$$

where the i index refers to the specific diffusion gradient direction, and b_{DWI_i} and b_{DWI_0} are the b-values of DWI_i and DWI_0, respectively. Normally, b_{DWI_0} is taken as 0, being the DWI_0 a typical T2-weighted image. For brain studies, b typically ranges from 600 s/mm² to 1000 s/mm². In diffusion pulse sequences, TE should be long enough to be compatible with the duration of diffusion gradients. Consequently, DW images are also based on T2 contrast. In terms of contrast, high diffusion areas are typically hypointense and low diffusion areas are hyperintense in DW images (3). The opposite is seen in ADC maps, as shown in Figure 2.2.
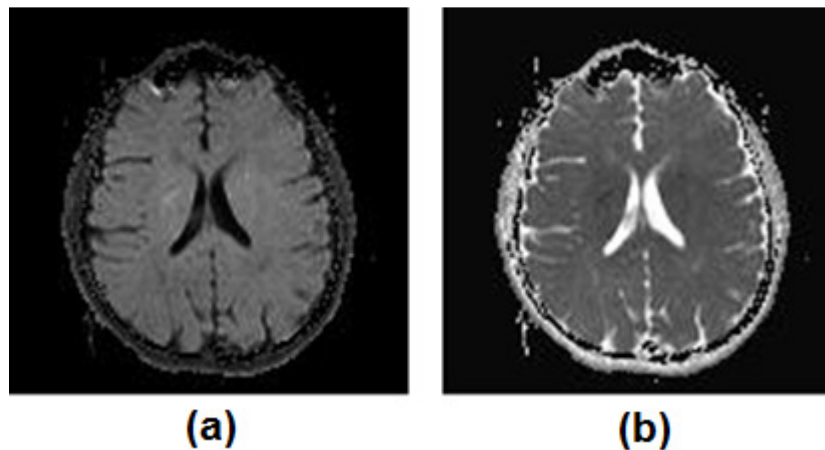
Figure 2.2 - DW Image and ADC Map. Examples of DW image (a) and ADC map (b) of an adult human brain. Scanner Siemens Verio 3T, acquisition parameters of DWI: TR/TE = 5300/85 ms, b-values: 0 s/mm² and 800 s/mm².

In the tensor model, principle of DTI, diffusion is described as a multivariate Gaussian distribution and the tensor is a 3 × 3 covariance matrix, as shown below:

$$T = \begin{pmatrix} D_{xx} & D_{xy} & D_{xz} \\ D_{yx} & D_{yy} & D_{yz} \\ D_{zx} & D_{zy} & D_{zz} \end{pmatrix} \qquad (2.2)$$

This matrix describes the displacement of water molecules in three dimensions normalized by diffusion time. The diagonal elements are variances of diffusion along the axes x, y and z, and off-diagonal elements are covariance symmetrical terms. Given the tensor symmetry, its construction demands DW images acquired in at least six directions, to obtain the six independent components. However, it is common to acquire DW images in 16, 32 or 64 directions, which improves the accuracy of each component of tensor. The tensor can also be displayed as an image; and the technique consisting of acquiring DW images in several directions to build the tensor is called diffusion tensor imaging, or DTI (4). From DT images, scalar parameters, or DTIi), such as fractional anisotropy (FA), relative anisotropy (RA), mean diffusivity (MD), volume ratio (VR), Sphericity (CS), Linearity (CL) and Planarity (CP), can be obtained. Table 2.1 shows the mathematical expressions and meanings of main DTIi.

Table 2.1 - DTI Indexes and Their Meanings.

DTI index	Mathematical Expression	Meaning
Mean Diffusivity	$MD = <\lambda> = \dfrac{\lambda_1 + \lambda_2 + \lambda_3}{3}$	Magnitude of diffusion, in units of mm^2/s]
Fractional Anisotropy	$FA = \sqrt{\dfrac{3}{2}} \dfrac{\sqrt{(\lambda_1 - \langle\lambda\rangle)^2 + (\lambda_2 - \langle\lambda\rangle)^2 + (\lambda_3 - \langle\lambda\rangle)^2}}{\sqrt{\lambda_1^2 + \lambda_2^2 + \lambda_3^2}}$	Grade of anisotropy; ranging from 0 (isotropic diffusion) to 1 (anisotropic diffusion)
Relative Anisotropy	$RA = \sqrt{\dfrac{1}{3}} \dfrac{\sqrt{(\lambda_1 - \langle\lambda\rangle)^2 + (\lambda_2 - \langle\lambda\rangle)^2 + (\lambda_3 - \langle\lambda\rangle)^2}}{\langle\lambda\rangle}$	Ratio of anisotropic and isotropic portions of tensor
Volume Ratio	$VR = \dfrac{\lambda_1 \lambda_2 \lambda_3}{\langle\lambda\rangle^3}$	Ratio of an ellipsoid and a sphere volume; ranges from 0 (isotropic diffusion) to 1 (anisotropic diffusion). Indicates if the tensor is oblate or prolate.
Sphericity, Linearity and Planarity	$CS = \dfrac{\lambda_3}{\langle\lambda\rangle}$ $CL = \dfrac{(\lambda_1 - \lambda_2)}{\langle\lambda\rangle}$ $CP = \dfrac{2(\lambda_2 - \lambda_3)}{3\langle\lambda\rangle}$	Geometric indexes that provide information about shape of the tensor; they can be plotted in a barycentric coordinate system. Each one ranges between 0 and 1 and their sum is equal to 1

λ_1, λ_2 and λ_3 are the eigenvalues of the tensor and $<\lambda>$ is the trace of the tensor.

DTI data can be used to reconstruct images of axonal fibers (5), skeletal muscle (6), and cardiac muscle fibers (7), through tractography techniques. Figure 2.3 shows a FA image, as well as a color map indicating axonal directions of diffusion in human brain. Figure 2.4 shows examples of fibers reconstruction and directional maps of cardiac and skeletal muscle.
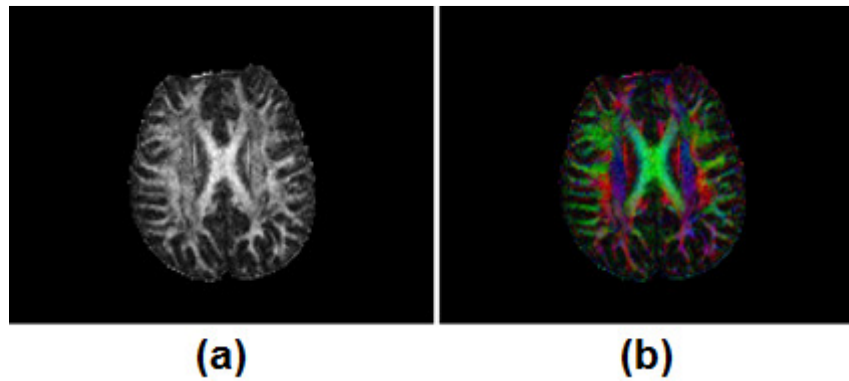
Figure 2.3 - Images Calculated from DTI Data of Adult Brain. (a) FA map. (b): FA color map showing the axonal diffusion directions: red: right-left; green: posterior-anterior; blue: superior-inferior.
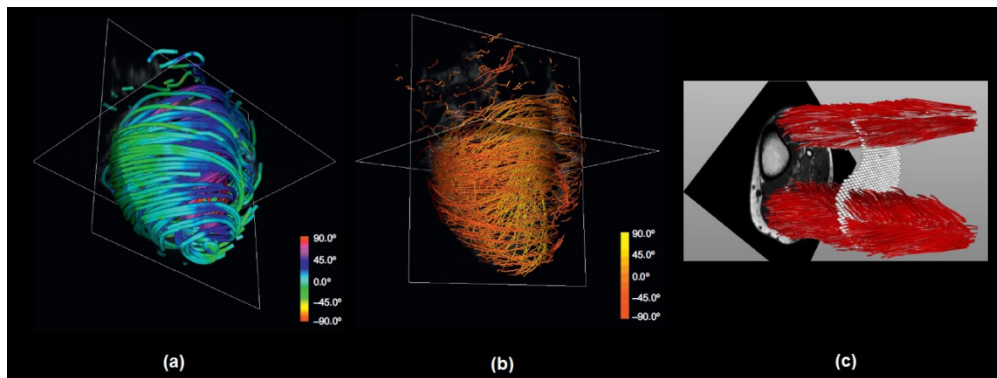
Figure 2.4 - DTI of cardiac and skeletal muscle fibers. (a) and (b): Fibers reconstruction and directional color map, respectively, of diffusion through the cardiac muscle fibers (7). (c): Tractography of leg's muscle fibers (8).

Currently, it is known that DT images and their indexes are quite sensitive to factors related to imaging acquisition and processing. The reliability of results obtained from these images depends on the quality of the acquired data. Low SNR, patient motion during the scan, chemical shift, inhomogeneity of the magnetic field B_0, RF interference, eddy currents and magnetic susceptibility effects can degrade the quality of DW and DT images (9). However, there is not a standard phantom or routine for quality control (QC) of these images, as occurs for QC of proton density (PD), T1 and T2-weighted image acquisitions. Development of QC techniques for diffusion images is necessary given the extension of their applications, as well as because these images are more sensitive to artifacts when compared to T1, T2 and PD-weighted images, depending on the magnitude and number of short diffusion gradients applied. In other words, changes in the MRI scanner tend to de-

grade DW and DT images before they compromise T1, T2 and PD-weighted scans. Recent studies have suggested phantoms for QC of diffusion acquisitions, based on different kinds of materials and a variety of geometries (10-13), as will be discussed below.

2.2 DWI AND DTI PHANTOMS

2.2.1 MRI Phantoms Described in Literature

Phantoms are devices that simulate the human body or their regions. In medical imaging, these devices are specially designed for calibration, performance evaluation and QC of different kinds of acquisition and processing methods. Ideally, the phantoms should respond in the same way as biological tissues when submitted to a specific technique (14). They can be physical (an object designed to test some medical imaging machine) or computational (mathematical models to evaluate the performance of processing and analysis' algorithms). Physical phantoms whose geometry are like human body are denominated anthropomorphic phantoms, commonly applied to dosimetry and radiation therapy QC. Figure 2.5 shows some examples of medical imaging phantoms.
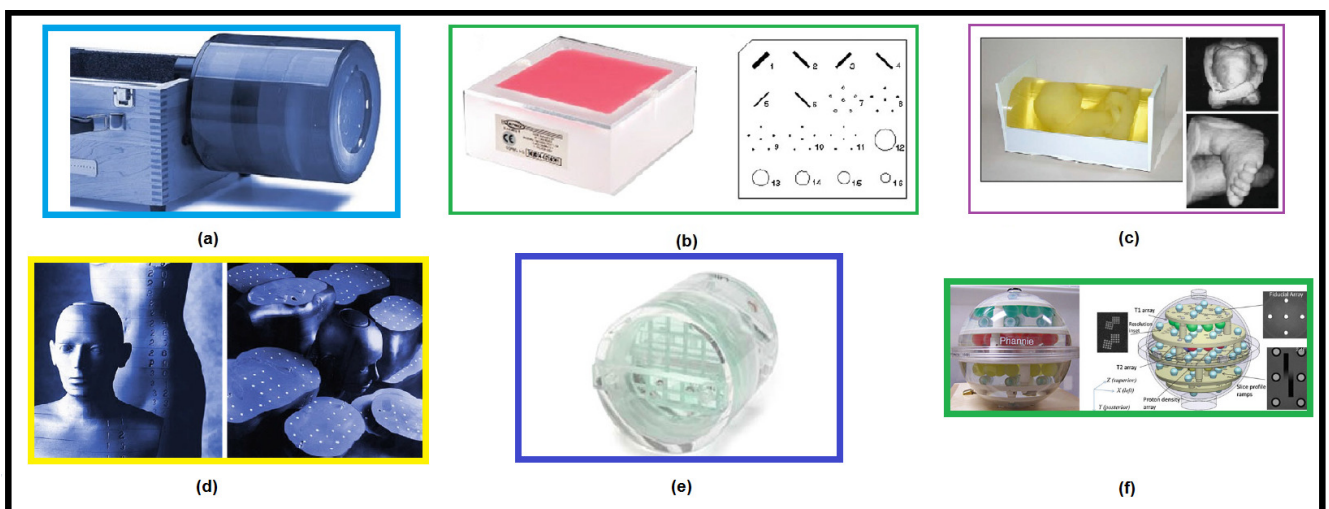
Figure 2.5 Phantoms for QC of Medical Imaging Devices. (a): Catphan - quality imaging phantom for QC in Computed Tomography (CT) (15). (b): ACR mammography phantom and their internal structures (16). (c): Ultrasound anthropomorphic phantom simulating an in-uterus fetus (17). (d): "Rando" anthropomorphic phantom, composed of urethane

formulation for mimicking human soft tissue (18). (e): ACR MRI knee phantom (19). (f): Phantom "Phannie" (National Institute of Standards and Technology, USA) containing inserts to evaluate relaxation times and spatial resolution in MRI (20).

The phantoms commonly used in MRI QC routine are not the best option for DW and DT images because of their high diffusivity, unlike what occurs in biological tissues. In addition, the compound that fills them is, generally, an aqueous paramagnetic solution containing $CuSO_4$, $NiCl_2$, $MnCl_2$ or $GdCl_3$, because of its long-term stability and relaxation time. However, these solutions have T1 very close to T2 (except the $MnCl_2$), which does not occur in biological tissues. The results from images of these solutions also depend on the geometry of the container that holds them. Desirable characteristics for a DWI or DTI phantom are covering of a large range of diffusivities, long-term stability, low cost, low toxicity, T1 and T2 values similar to biological tissues, and high viscosity in order to minimize vibration and convective motions effects (21).

Researchers suggest different kinds of phantoms for DWI and DTI QC, as well as different compounds and solutions to fill them (22-24). There are phantoms of isotropic diffusion for DWI (typically spheres or cylinders filled by liquid) (24-26); fiber phantoms to simulate axonal tracts or cardiac muscle (11, 13, 27); phantoms made of capillary or microcapillary arrays permeated by liquid with diffusion properties and/or relaxation times similar to biological tissues (28) test tubes with different solutions (23, 24); biological phantoms, such as green asparagus inside a water container (29); or animal tissues (axons of pigs or mice) (30, 31). There are gels, for isotropic or anisotropic diffusion studies, whose magnetic properties are similar to healthy or pathological tissue (10, 21). Some authors propose applying the ACR phantom, showed at Figure 2.6, to the evaluation of scanner parameters related to degradation of DW and DT images, such as SNR, low contrast detectability and uniformity (32). Computational phantoms can also contribute to QC of DW and DT image processing algorithms, being useful to evaluate tractography based on High-Resolution Angle Diffusion Imaging (HARDI), Q-Ball and Diffusion Spectral Imaging (DSI), applicable to analysis of crossing fibers in a voxel (33).
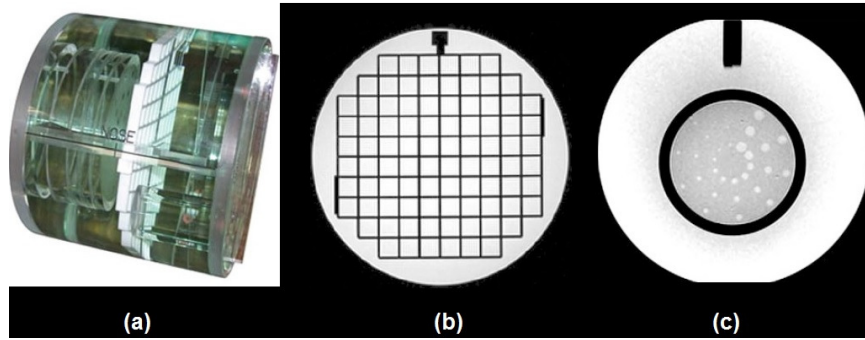
Figure 2.6 - ACR MRI Phantom and its Images. (a) Large ACR head phantom. (b) and (c): Images of the grid for geometric distortion and low-contrast detection evaluation, respectively (34).

2.2.2 Isotropic Diffusion Phantoms

Typically, these phantoms consist of spheres, cylinders or tubes filled by liquids or gels whose relaxation and/or diffusion properties are similar to biological tissues in the MRI environment. A 4.7 T nuclear magnetic resonance (NMR) spectrometer and a 1.5T MRI scanner were used to measure, respectively, self-diffusion coefficients and ADC values of 15 liquid compounds: 3 cyclic alkanes (from cliclohexane to cyclooctane), 9 n-alkanes (from n-octane to n-hexadecane), and 3 alcohols (from ethanol to 1-propanol). n-Tridecane showed ADC values close to normal white matter (WM), in agreement with measures of self-diffusion coefficients obtained from NMR. Nonetheless, despite the advantage of these compounds having defined NMR spectral lines, their use in clinical routine is limited by toxicity and inflammability (23). Non-toxic and stable compounds, such as aqueous solutions of polyvinylpyrrolidone (PVP), can be an alternative to agarose or alkanes. PVP showed long-term stability during a 15 months period (24).

Gels whose dielectric relaxation properties have values close to those found for biological tissue have been tested as filling for isotropic diffusion phantoms. Two gels based on polysaccharide carrageenan (CAG and CAGN) have been explored for isotropic phantoms. CAG consists of carrageenan as a gelling agent, agarose and $GdCl_3$ as T2 and T1 modifiers, respectively, in addition to distilled water and the antiseptic NaN_3, to reduce gel degradation by microbial agents. The CAGN phantom, besides the compounds already mentioned, also has NaCl to change electrical conductivity. The concentration of each

compound to reach the desirable diffusion properties is defined by an equation set. Those equations can be useful for the development of gels for DWI and DTI QC (21). Gels of sodium alginate, xanthan gum, FAVOR-PAC-300, PNC, Carbomer-980 and Carbopol-974P have also been tested as an alternative to agar or agarose (10). It was observed that images of gels had less distortion than images of liquids due to reduction of the macroscopic flow effect. Pathological conditions such as stroke can also be simulated by gels. A human brain phantom filled by agar-based gel has been applied to analyze DWI pulse sequences' performance to discriminate acute stroke and normal gray matter (GM). It was observed that ADC variation between stroke-like areas and GM was similar to that found in human brain (26).

Other kind of container used in DWI phantoms are test tubes. Tubes with different concentrations of a polyacrylamide gel and a sucrose solution were applied to check the performance of Echo-Planar Imaging (EPI) and Half-Fourier Acquisition Single-Shot Turbo Spin-Echo (HASTE) pulse sequences. There were not significant differences between ADC values of both pulse sequences. However, HASTE leads to less ghost and is better to characterize high-value ADC regions (35). Tubes filled by different concentrations of polyethylene glycol (PEG), to control diffusivity, and Gadobutrol, to control T2, were also tested as isotropic diffusion phantoms (36). From all studies of isotropic diffusion phantoms, the agar or agarose is the most applied compound. Figure 2.7 shows an example of a gel-based isotropic diffusion phantom for DWI evaluation.
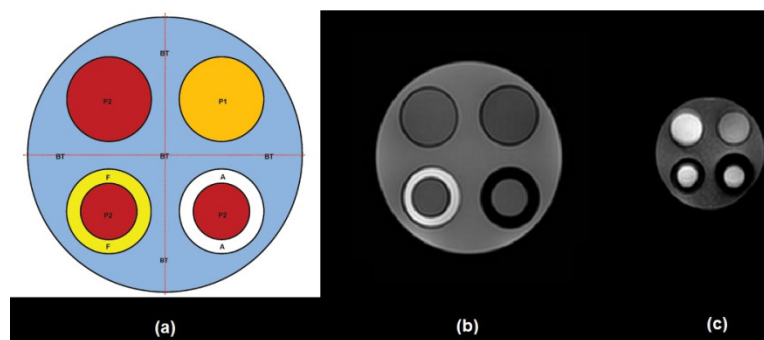
Figure 2.7 - Example of isotropic diffusion phantom. Four-Compartments Isotropic Diffusion Phantom. The compartments of disk can be filled by gels simulating different kinds of tissues. (b) and (c): T1 and T2 images of phantom (25).

2.2.3 Anisotropic Diffusion Phantoms

Anisotropic diffusion phantoms are useful for DTI QC. A DTI phantom was made of layers of an agar-based isotropic gel, each layer having a different conductivity. It was shown that gels make the setup more stable and reduce imaging artifacts due to reduction of the macroscopic water flux (12).

Polycaprolactone (PCL) and polyethylene oxide were used to make axon-like structures using the co-electrospinning technique. The phantom was tested in a preclinical 7T MRI scanner, and it was found that MD increases when the fiber diameter increases and FA decreases when the fiber internal diameter increases. The setup remained stable for 1 month; however, it was a small phantom, incompatible with clinical scanners (12). The co-electrospinning technique was also used to develop an anisotropic phantoms to simulate cardiac muscle tissue (13). Phantoms made using lithography and other microfabrication techniques have also been reported to be useful for DTI QC and pulse-sequence tests (28, 37).

Dyneema® fibers are a good option to build DTI phantoms. These fibers have multiple filaments, being more anisotropic than nylon, polyester, polyamide or linen. A phantom consisting of 780 parallel Dyneema® fibers 20 mm thick, packed inside a polyolefin tube, was proposed for DTI QC (11). The FA values of Dyneema® fiber bundles are close to those found in human brain axons and few artifacts are observed on DTI images and tractography. However, the phantom relaxation times differ from those from biological tissues. This may occur because diffusion is limited to the interstitial space between the fibers, where proton density is lower when compared to tubular axons. Despite this, the phantom seems useful to DWI and DTI QC. Parallel and perpendicular Dyneema® fibers were applied to build a multilayer DTI phantom. For DTI images obtained in a 3T scanner, the FA values were also close to those seen in brain WM (27). Figure 2.8 shows an example of phantom made of this fibers and the corresponding tracts' reconstruction.
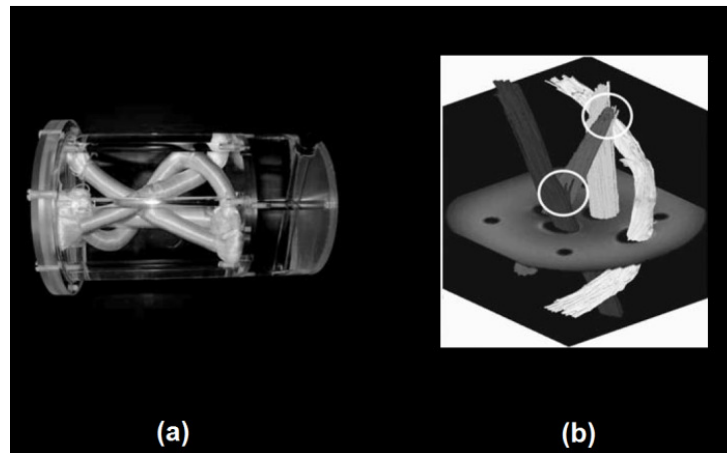
Figure 2.8 - Example of anisotropic fiber bundle found in literature. (a) Cylinder with bundles simulating axonal fibers. (b): Tracts reconstructions of fibers' phantom (38).

The stability and reproducibility of DTI parameters have also been checked with organic animal or vegetal phantoms, such as green asparagus inside a water container (29), mice nerves (31) or pig spinal cord (30).

The development of phantoms and protocols for QC of DW and DT images is a subject currently covered by several research groups, given the need for standardization of multicenter/multiscanner studies and to obtain reliable data for diagnosis in clinical practice. However, there hasn't been agreement about the phantom to be applied or the QC acquisition protocol to detect changes in these images before clinical data degradation. This is due to the wide variety of scanner settings and acquisition techniques. In the reviewed studies, the range of B_0 goes from 0.5T to 9.4T. Most studies apply SE-EPI sequences or their clinical/research routines (13, 27). New sequences, such as d-PSGE, are being proposed and tested (30, 38). The d-PSGE sequence was developed for detecting GM microscopic anisotropy, while only macroscopic isotropy is seen with conventional DTI pulse sequences. The former sequences may be helpful for studies of diseases which degrade GM, such as multiple sclerosis, Alzheimer's disease, Huntington's disease, epilepsy and demyelinating diseases. Out of the brain, these sequences may also be applied to study conditions which lead to degradation of skeletal, cardiac or smooth muscle (30).

The studies of DWI and DTI QC tested a variety of setups and materials to build phantoms, although many configurations have received more attention, such as Dyneema® fiber bundles, capillary arrays and containers filled by liquids whose relaxation times are similar to those of biological tissues. QC phantoms for medical imaging, in general, consist of containers filled by liquid to simulate a specific biological tissue or physiological

condition being studied. Thinking about water molecules' diffusion, it is possible to simulate their motion both on interstitial and intracellular environments.

Despite the improvement on shimming methods and parallel acquisition techniques, B_0 inhomogeneities lead to geometric distortions in DW and DT images. Therefore, to build MRI phantoms, it is better to choose containers with well-defined geometry, such as spheres or cylinders which enable identification of imaging distortions without corrupting SNR. Their filling solutions should have relaxation times close to those found for biological tissues. Among some liquids tested, n-tridecane has ADC similar to brain WM. However, cyclic alkanes are toxic and flammable compounds, hindering their use in clinical routine (23). On the other side, sugar-based solutions, despite not being toxic, undergo biological degradation and are not useful for long-term follow-up scanning. The same goes for agarose gels, which are degraded despite the addition of anti-septic agents (39). PEG and gadobutrol are compounds applied to fill both isotropic and anisotropic phantoms. Alone, PEG has a moderate effect on T2 compared to agarose/sucrose. However, it is efficient to control the range of ADC values. Independently changing concentrations of these compounds can produce different ADC and T2 values, respectively, simulating different kinds of biological tissues. To evaluate the performance of these compounds to follow anisotropic diffusion parameters, a cylindrical arrangement made of nylon or acrylic can be built, which cross section around already proposed values (38). This cross section can be divided into four quadrants, in which circular cavities of different diameters are made and filled with test tubes or capillaries open at both ends. Each quadrant structure must have the same dimensions. This setup may be put in a Plexiglas cylinder filled by PEG and gadobutrol and sealed. The PEG and gadobutrol concentrations, as well as the dimensions of the phantom and capillaries/test tubes should be chosen according to the acquisition coil and biological tissue to be simulated. To avoid air bubbles in the phantom a syringe can be used for inserting the solution in the container; also, remaining bubbles can be removed with a vacuum pump. It is important to look for and remove air bubbles to minimize magnetic susceptibility effects. Laundry detergent can remove bubbles, due to its ability to move them to the phantom surface, where they can be eliminated. One quadrant of the phantom must remain without tubes or capillaries for assessing isotropic scattering.

It is observed that synthetic polymer-based gels can be a good alternative to agar, because of their long-term stability and easy synthesis (10). The main advantages of gel applications in DWI and DTI phantoms (which have fiber bundles and/or other structures where diffusion is anisotropic) is the reduction of flow and convective effects, that cause

image artifacts (10). Therefore, it is necessary to control gel compounds' concentrations and consequently the T2 and diffusion parameters of the phantom. T2 control its necessary because it is the basic weighting of all diffusion images. So, controlling T2, the SNR is controlled. In addition, at the acquisition preparation stage (pre-scan), there are adjustments of the signal reception and transmission systems (RF coils, gradients, shimming). The gain of these devices is related to how acquired data are converted into image. For each scan, such gains are recalibrated, and there may be variations of scale factors between different acquisitions.

The use of a microcapillary-based phantom for DTI QC at the same time of patient acquisition is quite interesting, but microcapillaries or other microscopic structures are not the best alternative for QC of these images. Microscopic structures enable the construction of arrangements where water molecules' diffusion is closer to diffusion seen at biological tissues, both in the interstitial and intracellular environments (28). Nonetheless, their use as QC devices shows limitations such as device irreproducibility (their construction is complex) and dependence on microscopy to properly evaluate their structural integrity. Moreover, smaller air bubbles may not be detected and their removal is not easy. In addition, MD and FA values of these phantoms differ significantly from those obtained from biological tissues in most cases, because when phantom structures have dimensions lower than the scanner spatial resolution, bias in MD and FA values may occur (13). It is also worth mentioning that the pattern of magnetic field distortion due to the patient's head and to the phantom in the scanner is different from that seen in images of one or the other independently (40).

3 MATERIALS AND METHODS

In this chapter, we initially describe the first designed DTI phantom, the tests performed with it and the encountered problems. Subsequently, a description of tests performed with new materials is described. Concluding, a multipurpose fiber phantom is proposed, being its design showed and their test routines detailed.

3.1   THE FIRST DTI PHANTOM DESIGNED

In the first stage of the study, the dimensions of the phantom, possible geometries and materials to be applied were defined. It was known that none of the phantom's components could contain ferromagnetic elements, due to the high intensity magnetic field of the MRI scanner. Ferromagnetic materials can be strongly attracted by the magnet, putting at risk the scanner and people around it. After some previous assays with three kinds of fishing lines (polyamide, Kevlar® and Dyneema®) and two geometries of containers (cylindrical and rectangular), a DTI fiber phantom consisting of an acrylic cylinder with 200 mm height and external and internal diameters of 180 mm and 170 mm respectively was built. Inside the cylinder a hollow acrylic block was inserted, composed of two sides of 120 × 120 × 10 mm^3 and two sides of 180 × 120 × 10 mm^3. The block had 18 circular holes of 10 mm diameter and 18 circular holes of 20 mm diameter regularly distributed at the sides, where it was possible to put and steady fiber bundles. The holes could also be useful to visualize geometric distortion effects. Figure 3.1 shows the diagram of the cylinder and of the rectangular insert.
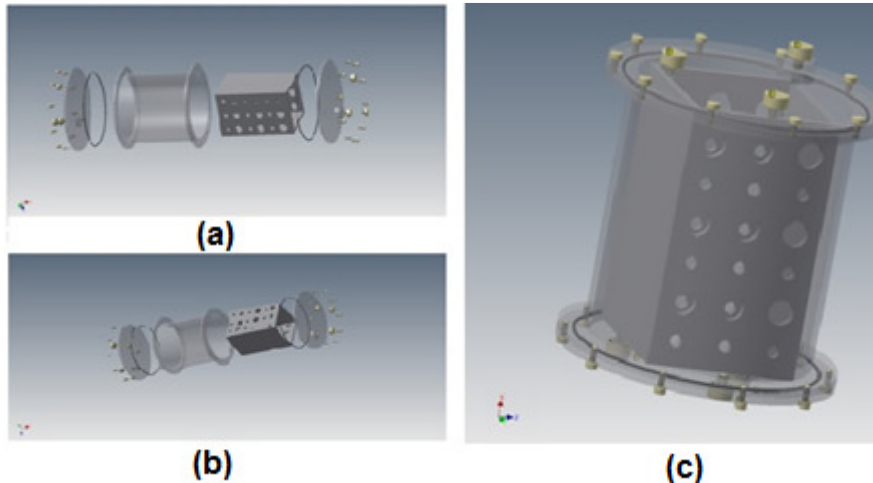
Figure 3.1 3D layout of acrylic structures of phantom. (a) and (b): Main cylinder and rectangular insert. (C): Rectangular insert positioned inside the cylinder. The cover of the cylinder is fixed using nylon screws.

In three of the 20 mm diameter holes three fiber bundles of length of 190 mm and thickness of 10 mm were positioned. These bundles were composed by multifilament Dyneema® fishing lines, and were identified as 1, 2 and 3. Each one contained, respectively, 200 fibers of 0,25 mm thickness, 150 fibers of 0,35 mm and 130 fibers of 0,40 mm. The compression and fixation of the bundles were made using nylon cable ties, so that the three bundles had approximately the same average thickness: (74,90 ± 1,20) mm for bundle 1, (75,48 ± 0,95) mm for bundle 2 and (75,62 ± 2,01) mm for bundle 3, measured using a digital caliper. A shown in Figure 3.2, the bundles were intentionally not completely straight, given that for most biological tissues tracts are disposed following anatomical contours. The phantom was built by the technicians of the Biomedical Engineering Center (CEB) of University of Campinas (UNICAMP). Dyneema® fishing lines were chosen for these experiments because several studies have demonstrated that their raw material is useful to build fiber bundles whose FA values are similar to those of biological tissues (11, 27, 38). However, fishing lines can be easily found in shops. The fishing lines applied have diameters larger than most of neuronal fibers, but are less susceptible to effects of magnetic susceptibility and field distortions than microscopic fibers and structures (28, 40).
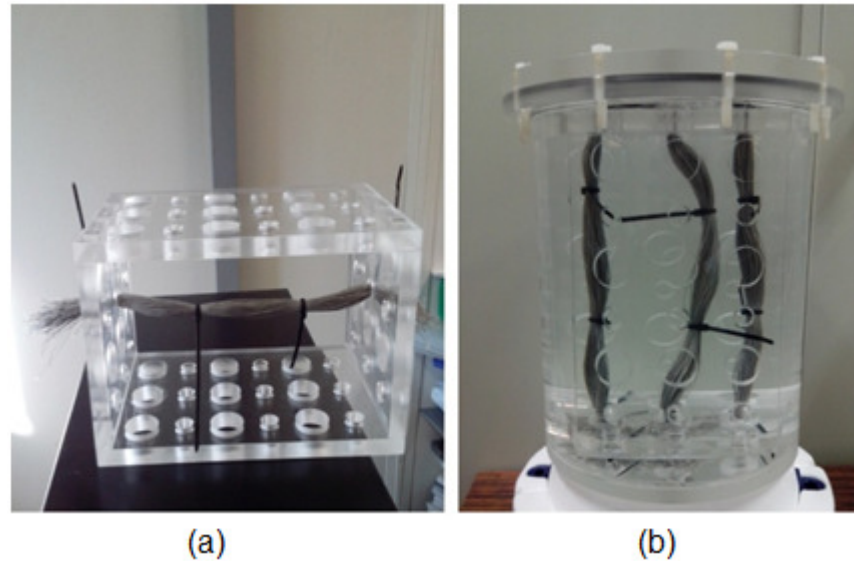
Figure 3.2 - **Pictures of the first DTI phantom built.** (a) Rectangular block for fiber bundles fit. (b) The phantom is settled on a Styrofoam support, mounted and then filled with distilled water. The support is not used in scans. On the left, middle and right are the bundles 1, 2 and 3, respectively.

3.1.1 DTI Phantom Study

To evaluate the stability of DTI acquisitions using the phantom of Figure 3.2 (b), images were acquired to verify how changes in the acquisition parameters could modify the DT images. Recently, the influence of some DTI acquisition parameters on MD and FA has been studied (41-44). However, there has been no detailed investigation of the role of acquisition parameters in other DTIi described in Table 2.1.

All images were acquired with the Achieva® 3T MRI scanner (Philips, The Netherlands) of the Clinics Hospital (HC) of UNICAMP using an 8-channel and a 32-channel phased-array receive-only head coil. The phantom was placed at the scanner's room 72 hours before acquisitions to minimize effects of temperature variation. The position of the phantom was the same in all acquisitions, with its center aligned with the center of each coil. The DT images were acquired changing the following parameters: the diffusion sensitizing factor b, the time of echo (TE), Number of Averages (NSA), Sensitivity Encoding (SENSE), voxel size and Number of Directions of Gradient Diffusion (NDGD), one at a time, taking as reference the clinical acquisition protocol for brain. TE is the time between the application of the excitation RF pulse and the echo generation; NSA is the number of

signal measurements (or number of excitations) from which to compute an average (for SNR improvement purposes). SENSE is a parallel imaging acquisition technique which can reduce susceptibility artifacts from Echo-Planar (EPI) techniques (33), such as SE-EPI, applied in this study. It is done skipping lines in k-space while acquiring data from different channels simultaneously. The channels consist of receiver coils with known sensitivities (45). The acquisition parameter changes were the same for both coils, as described in Table 3.1.

Table 3.1 - DTI acquisition standard parameters for both coils and the variations tested in this study.

Acquisition Parameter	8-channel head coil Standard Protocol	32-channel head coil Standard Protocol	Variations
b (s/mm^2)	1000	1000	500/800/1000/ 1200/1500/2000/2500
TE (ms)	85	70	70/80/85/90/100
NSA	1	2	1/2/4/6
SENSE	2.5	3	2/2.5/2.8/3/3.5/3.8
Voxel Size (mm^3)	2	2	1/1,5/2/2.5/3
NDGD	32	32	6/15/32

The Field-of-View (FOV) and flip angle applied were, respectively, 224 x 224 x 120 mm and 90°. FOV, radiofrequency (RF) receiver bandwidth and receiver gain were not changed in relation to standard protocols for both coil. All acquisitions were doing with isotropic voxel. Figure 3.3 shows a diagram of the main steps of this part of study.
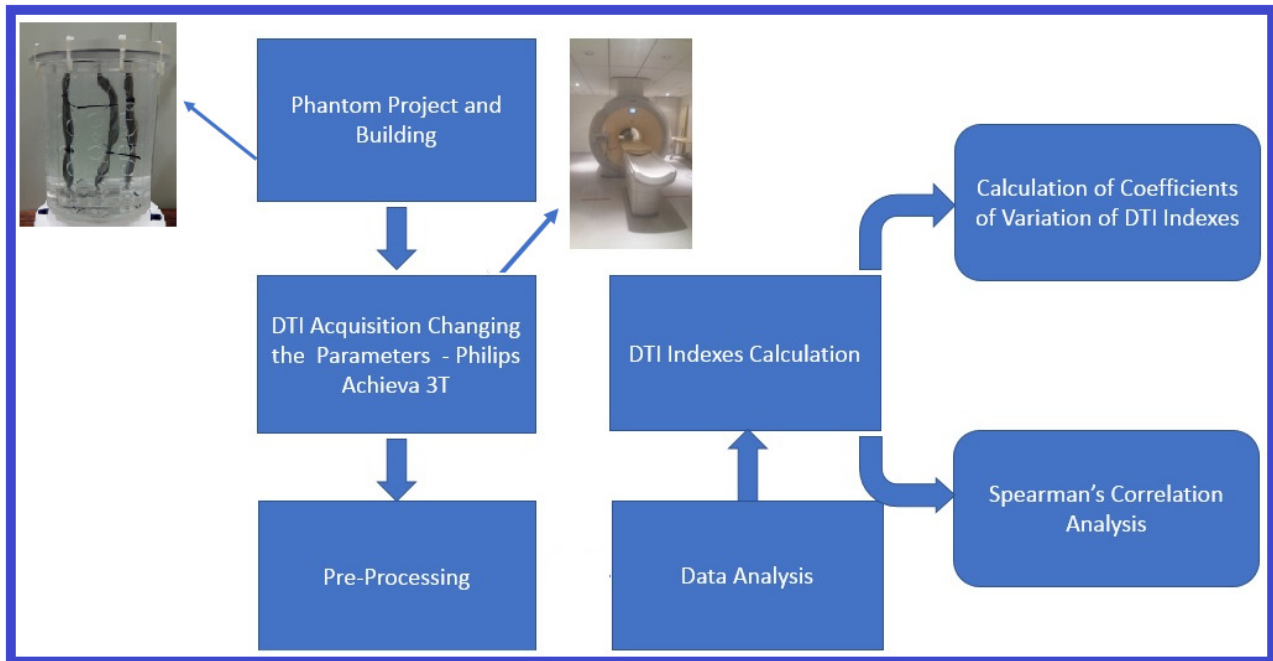
Figure 3.3 – Diagram showing the main steps of this part of study.

3.1.2 Pre-Processing: Data Quality Control

The Figure 3.4 summarizes the main steps of pre-processing applied to all DT images of this thesis. The images are obtained in both DICOM and PAR/REC formats (the latter being a Philips specific format). Before any calculation was performed, the non-diffusion-weighted image (T2) and all DW images acquired in different directions within a protocol (i.e., in same acquisition conditions) were co-registered. This step reduces effects of vibration and motion during scanning, which might affect the outcome of the study. All images were then submitted to the QC routines of the ExploreDTI software (46), which employs calculations based on a residual model and creates image outliers maps (47). These routines can identify possible distortions that might lead to bias in DTIi.
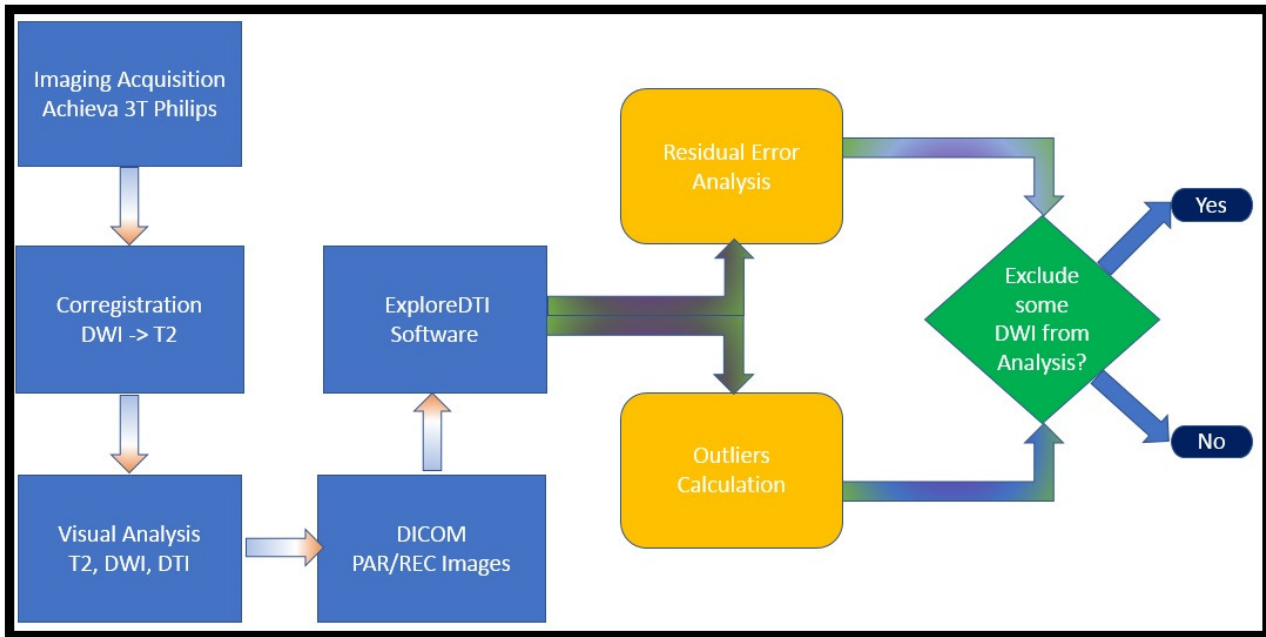
Figure 3.4 – **Block diagram showing the steps of imaging pre-processing.**

A residual can be defined as the difference between a modeled and a measured signal. Large residuals indicate that the applied model (the second-rank diffusion tensor) is not able to characterize the observed signal accurately, reflecting either the inadequacy of the model or the presence of signal intensities related to artifacts. Assuming the latter, a residual map R can show artifacts that are not always visible on the FA map or the individual DW images. Mathematically, R is defined as the average residual of the observed signal DWI_{obs} to the modeled signal DWI_{mod}, i.e.,

$$R = \frac{1}{K}\sum_{k=1}^{K}\left|DWI_{obs}^{k} - DWI_{mod}^{k}\right| \tag{3.1}$$

where the K modeled DWI signals, with corresponding **B** matrices $\mathbf{B_k}$ (k = 1…, K), are derived from the fitted diffusion tensor $\mathbf{D_{fit}}$, and the T2 (b = 0) image:

$$DWI_{mod}^{k} = T2 \times e^{-\mathbf{B}_k\,\mathbf{D_{fit}}} \tag{3.2}$$

In general, a poor diffusion tensor fit, assumed to be caused by artifacts, results in higher residuals, and a uniformly appearing R map reflects good quality image data. The residual calculations, residual maps and outlier maps were applied as QC of acquired data.

3.1.3 Processing: ROI Delineation, DTIi Calculation and Tracts Reconstruction

For images without significant outliers or high-amplitude residual errors, ExploreDTI was also used to manually draw Regions of Interest (ROIs), one ROI for each fiber bundle, for each DT image acquired. 2D seed-based ROIs were applied. Seeding consists of defining the points from which the fiber bundles will be drawn (in this case the points were located around the visible bundles) (48). From these ROIs, we calculated the eigenvalues (λ's) and eigenvectors of diffusion tensors and the tracts' reconstruction was made, as well as the MD, FA, diffusion ellipsoids and directional diffusion maps were computed. ExploreDTI gives MD and FA values; the calculation of other DTIi (RA, VR, CS, CL and CP) was performed getting the obtained λ values and using them in home-developed Matlab® routines (version R2014b; Matlab Inc., Natick, MA, USA). The DTIi calculated were organized in spreadsheets using Office Excel® software (Microsoft Inc., 2007). The λ, MD and FA values obtained were compared to values obtained from Achieva® FiberTrak processing software (Philips, The Netherlands), where the tracts reconstruction was also done using 3D seed ROIs. These ROIs were defined from three 2D manual ROIs positioned in the middle and in the extremities of visible fiber bundles.

3.1.4 Data Analysis

The statistical analyses were performed using SPSS (version 22; SPSS Inc., Chicago, IL, USA). In this software, we calculated the following statistical measures: mean, standard deviation and coefficient of variation of DTIi for each bundle, each coil, and acquisition parameter changed. Using this software, we also made the two-tailed Spearman's Correlation Analysis to evaluate the existence of correlations between acquisition parameter variations and the DTIi calculated, for each fiber bundle and each head coil used.

3.2 TESTING NEW MATERIALS

Despite Dyneema® having shown excellent properties to simulate biological anisotropic structures, other materials were also tested. Conduits, bundles of catheters filled by

distilled water and other kinds of fishing lines (Kevlar® and Spectra®) were fixed on the phantom's rectangular block as shown in Figure 3.2. This setup had the following characteristics: 2 conduits of 10 mm diameter and 180 mm length; a bundle of 10 catheters of 2 mm diameter and 140 mm length; a bundle of 10 catheters of 1 mm diameter and 140 mm length; a bundle of 200 Spectra® fishing lines of 0.178 mm diameter (bundle diameter: 14 mm, 185 mm length); a bundle of 46 Kevlar® fishing lines of 0.34 mm diameter (bundle diameter: 16 mm, 185 mm length); a bundle of 46 Kevlar® fishing lines of 0.25 mm diameter (bundle diameter: 10 mm, 185 mm length). Spectra® is a multifiber line made of polyethylene by a patented gel-spinning process, being on average stronger than steel and aramid. All the fishing line bundles were wrapped using shrinking tubes. The setup is shown in Figure 3.5.
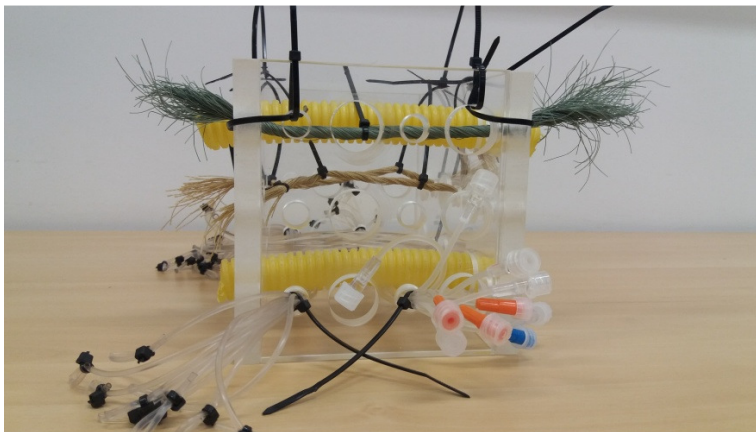
(a)

(b)
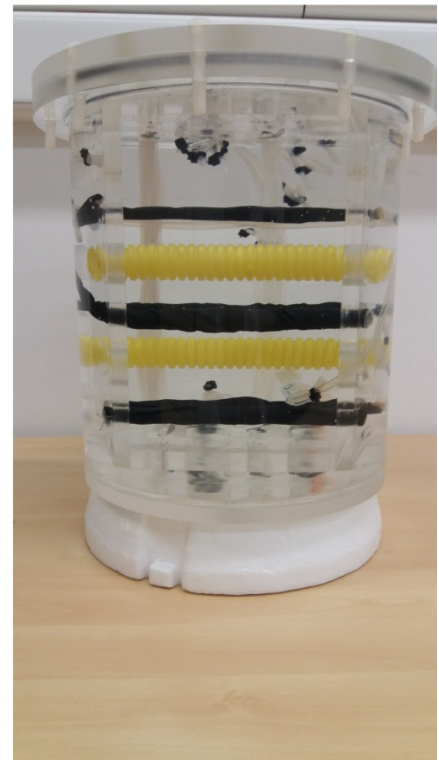
(c)

Figure 3.5 - **DTI phantom setup using different kinds of materials and fishing lines.** (a) Rectangular block with conduits, catheters and fishing line bundles. (b) and (c): transversal and frontal views of the phantom. The fishing line bundles were wrapped by shrinking tubes.

This setup was tested in DTI acquisitions with the 8-channel head coil changing NDGD (6, 15 and 32 diffusion gradients directions). All three acquisitions were made using the SE-EPI pulse sequence with the following parameters: TR/TE (ms) = 7000/shortest; b = 1000 s/mm^2; voxel size = 2 × 2 × 2 mm^3; FOV = 224 × 224 × 120 mm^3.

3.3 EVALUATING CLINICAL PROTOCOLS

Based on the results obtained with the setups and materials described previously, this step applied fiber bundles based on Dyneema®, Spectra® and Polyamide to study how the DTIi changes for different clinical brain DTI acquisition protocols, using the 8-channel head coil. Table 3.2 shows the characteristics of each fiber bundle built. Figure 3.6 shows the bundles positioning in the rectangular block. All the fiber bundles were compressed and wrapped using shrinking tubes. A piece of shrinking tube was also used as a positional reference. Figure 3.7 shows pictures of the bundles fixed in the rectangular block, as well as the phantom ready for imaging acquisitions.

Table 3.2 - Characteristics of fiber bundles used in the setup to evaluate DTIi behavior for different clinical protocols.

Fiber Bundle	Reference Code	Number of Fibers	Fibers Diameter (mm)	Bundle Diameter (mm)	Bundle Length (mm)
REF		Just a 5-mm length and 10 mm diameter piece of shrinking tube for positional reference; no fibers inside			
SPECTRA	B1	400	0.178	10	190
POLYAMIDE	B2	300	0.485	12	190
DYNEEMA 1	B3	300	0.40	10	190
DYNEEMA 2	B4	300	0.35	10	190
DYNEEMA 3	B5	300	0.25	10	190
DYNEEMA CROSSING	B6	130	0.40	10	120
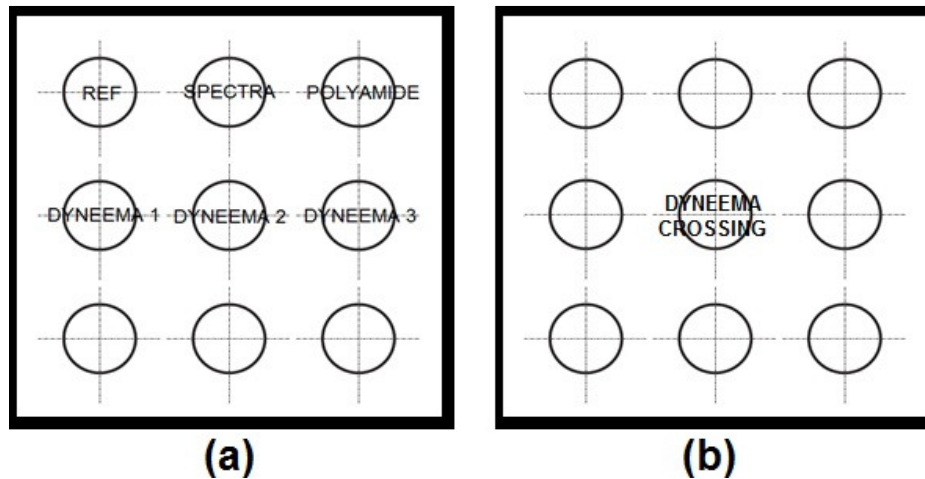
Figure 3.6 - **Fiber bundles positioning in the rectangular block.** (a): frontal view (b): lateral view, showing the Dyneema® bundle that crossing with bundles Spectra® and Dyneema®. The holes without identification are empty (do not have fiber bundles).

With the setup described above, five different brain protocols were tested, using the 8-channel head coil. All protocols used the SE-EPI sequence, with TR = 8500 ms, TE = shortest, and b = 1000. The parameters that were varied among protocols are detailed in Table 3.3.

Table 3.3 - Acquisition parameters for each DTI protocol studied. All protocols used the SE-EPI sequence, with TR = 8500 ms, TE = shortest, and b = 1000.

Protocol	NDGD	FOV (mm)	Voxel Size (mm)	Number of Slices
DTI-Low	6	224 × 224 × 120	2 × 2 × 2	60
DTI-Medium	15	224 × 224 × 120	2 × 2 × 2	60
DTI-High	32	224 × 224 × 120	2 × 2 × 2	60
Precocious Epilepsy	32	256 × 256 × 140	2 × 2 × 1	70
Primary Tumor	32	256 × 256 × 140	2 × 2 × 2	70
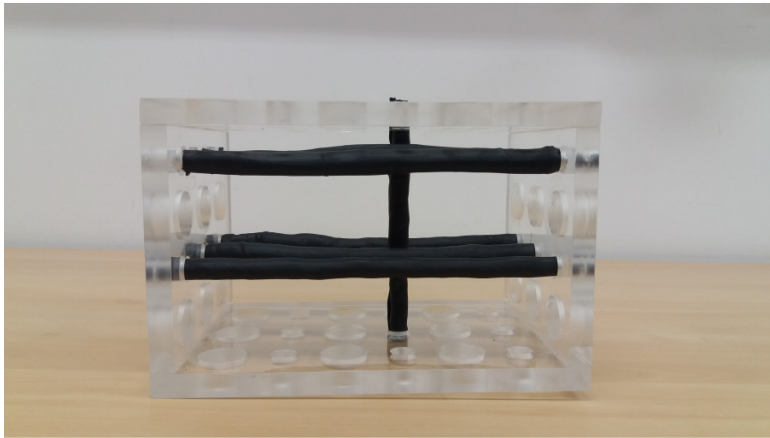
(a)

(b)

(c)

Figure 3.7 - DTI phantom applying Dyneema®, Spectra® and Polyamide fiber bundles. (a) and (b): pictures of the rectangular block were the bundles were fixed. (c): Picture of the phantom finished and ready for imaging acquisitions.

Besides the first three protocols (DTI-Low, DTI-Medium and DTI-High; see Table 3.3) changing NDGD, we tested just the clinical protocols for precocious epilepsy and for primary tumor, since they are the most representative of all clinical protocols. In other words, all other protocols for brain DTI using the 8-channel head coil are similar to the chosen ones, changing sometimes just the slice direction.

3.4 BUILDING A MULTIPURPOSE DTI PHANTOM

A multipurpose phantom is a device designed to evaluate many performance characteristics of MRI scanner using the same setup and positioning, only changing the imaging acquisition protocol (14). With the aim of doing DTI QC and other MRI QC measurements using the same setup, in this stage a multipurpose phantom was designed. This phantom was expected to provide maximum amount of information in a reproducible manner with the shortest data acquisition time. The developed device has modules to evaluate DTI acquisitions and slice thickness, spatial resolution and geometric distortions. It joins characteristics of the DTI phantom showed in previous steps and of the MRI QC rectangular phantom proposed by Fluke® Biomedical (49), shown in Figure 3.8. The manufacture of this product was discontinued.

(a)   (b)
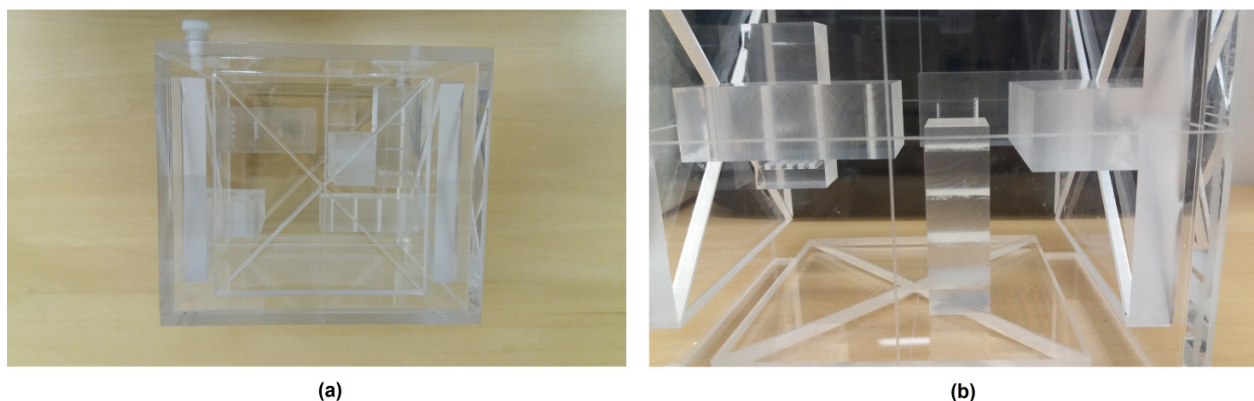
Figure 3.8 - **Commercial MRI phantom from Fluke® Biomedical for slice thickness and spatial resolution evaluation.** Pictures of phantom (a) and its internal structures (b). It is possible to see ramps for slice thickness (three larger squares with crosses) and the three blocks with small squared holes for spatial resolution measurements.

The multipurpose phantom built was based on an acrylic cylinder with 180 mm height and external and internal diameters of 170 mm and 160 mm respectively, where it is possible to put modules to evaluate different MRI performance aspects. For DTI QC, a hollow acrylic block was inserted, composed by two sides of $100 \times 100 \times 5$ mm^3 and two sides of $60 \times 60 \times 5$ mm^3. The block has nine circular holes of 10 mm diameter regularly distributed at the block sides, where it is possible to put and steady different fiber bundles' settings. Holes of this block may also be useful to detect geometric distortion effects,

which are more specifically evaluated by the rectangular acrylic plate of 120 × 100 × 5 mm³, where there are holes of 10 mm diameter regularly distributed. Slice thickness can be evaluated in three directions (axial, sagittal and coronal), using three square plates of 100 × 100 × 8 mm³ with 1 mm and 2 mm of thickness diagonal gaps. In turn, the spatial resolution can also be evaluated in three directions using three blocks of 20 × 25 × 5 mm³, where four holes with 0.5 mm, 1 mm, 2 mm and 2.5 mm diameter are disposed, with the holes having one specific dimension in each row. The phantom modules are positioned in the cylinder using polyacetal spindles fixed on its cover. The different modules can also be used stand alone. Figure 3.9 shows the diagram of the positioning of structures in the phantom, and Figure 3.10 shows the pictures of the phantom and a setup for imaging acquisitions.
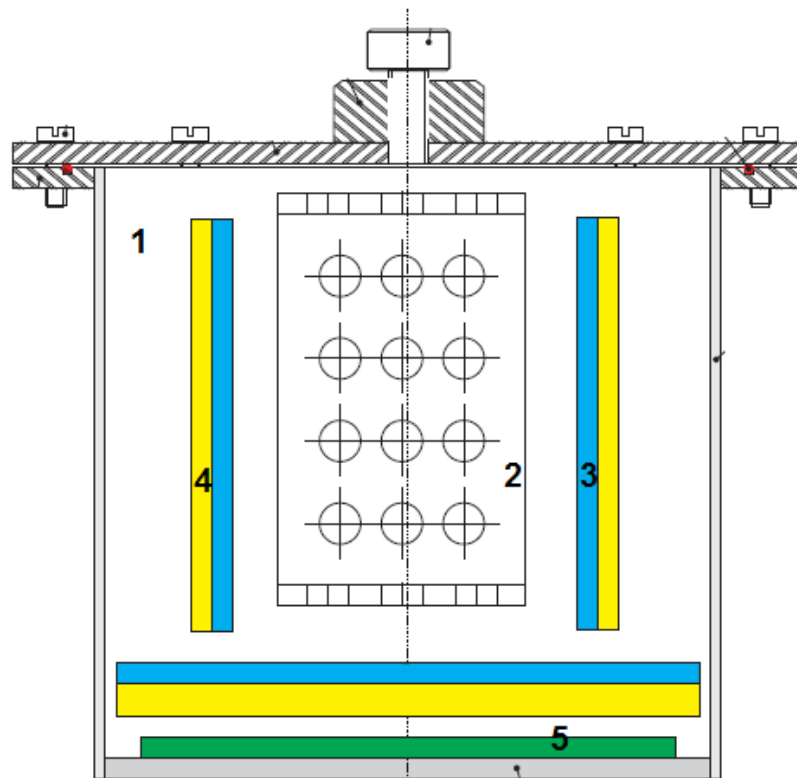
Figure 3.9 - **Diagram of the multipurpose phantom built and its structures' positions.** 1: Acrylic cylinder; 2: DTI acrylic block module; 3: spatial resolution block; 4: slice thickness plate; 5: geometric distortion plate.
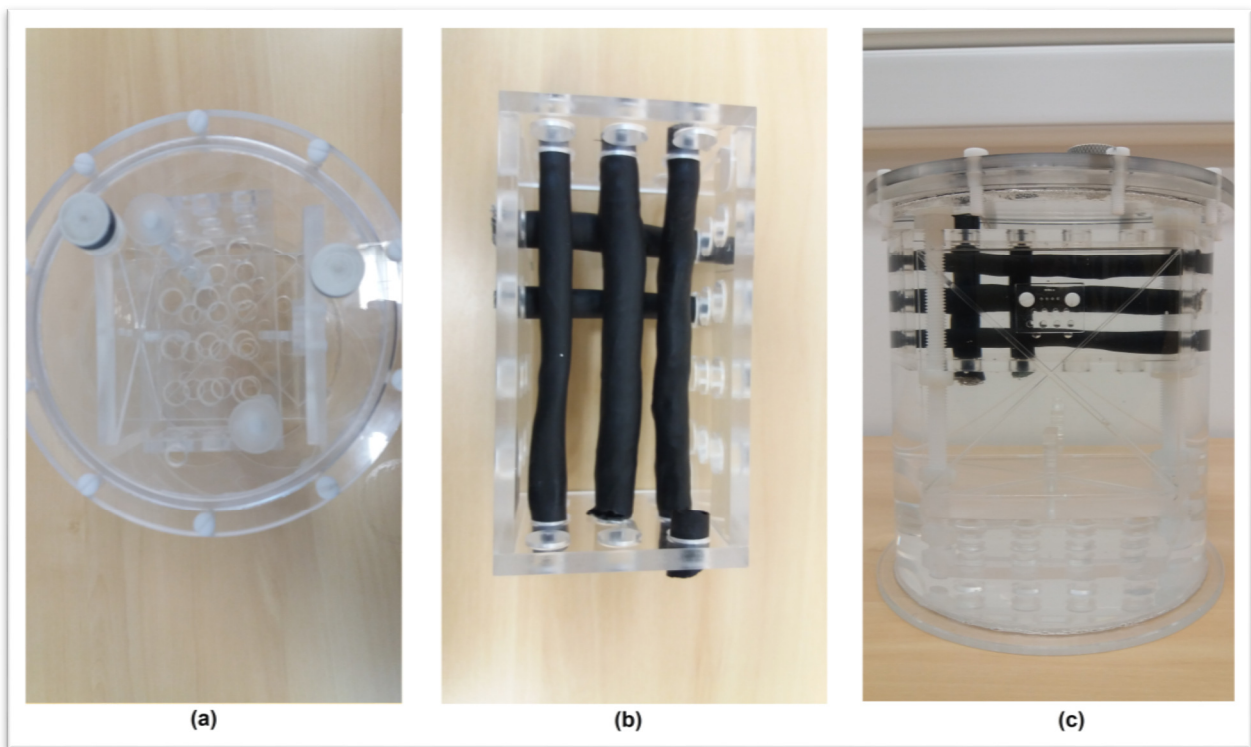
Figure 3.10 - **Pictures of the multipurpose phantom developed.** (a): Modules inside the cylinder, without fiber bundles for DTI QC. (b): DTI module containing the fiber bundles wrapped by shrinking tubes. (c): Phantom with all modules mounted, filled by distilled water and ready for MRI QC acquisitions.

Table 3.4 brings the characteristics of fiber bundles used in acquisitions with the multipurpose phantom.

Table 3.4 - Characteristics of Fishing Line Bundles Implemented in Multipurpose DTI Phantom.

Fiber Bundle	Reference Code	Number of Fibers	Fibers Diameter (mm)	Bundle Diameter (mm)	Bundle Length (mm)
REF	Just a 5-mm length and 10 mm diameter piece of shrinking tube for positional reference; no fibers inside				
SPECTRA	B1	400	0.178	10	100
DYNEEMA 1	B2	300	0.40	10	100
DYNEEMA 2	B3	300	0.35	10	100

3.4.1 Imaging Acquisitions

The evaluation of the multipurpose phantom for MRI QC was performed using an acquisition protocol including T1, T2, PD and DT images. The acquisition parameters are listed in Table 3.5. The total scan time for the protocol was on average 20 minutes.

Table 3.5 - Acquisition parameters for MRI QC protocol using the multipurpose phantom.

Image type	T1	T2	DTI 1	DTI 2
Pulse sequence	SE	SE	SE-EPI	SE-EPI
FOV (mm^3)	180 × 180 × 200	180 × 180 × 200	180 × 180 × 200	180 × 180 × 200
Voxel Size (mm^3)	2 × 2 × 2	2 × 2 × 2	2 × 2 × 2	2 × 2 × 2
Slice Thickness (mm)	2	2	2	2
Number of Slices	100	100	100	100
TR (ms)	400 - 700	Shortest	7000	7000
TE (ms)	65	400	65	65
b (s/mm^2)	--------	--------	1000	2500

The phantom modules were positioned to be at a distance of at least 10 mm from each other and can be adjusted as needed. The DTI module contained three parallel fiber bundles, two of Dyneema® and one of Spectra® fishing lines.

3.4.2 Data Analysis

Measurements for estimation of slice thickness, SNR, spatial resolution and geometric distortions were done using the ImageJ® software. The DTI measurements were performed using the software and computational routines previously described.

3.4.2.1 Measuring the Slice Thickness

Slice thickness was measured using the T1 images of the multipurpose phantom, taking the profile of the gaps in the three squared plates. Given that the slices of this image had 2 mm thickness, up to now only the gaps with this size were used for this evaluation. The slice thickness is defined by the full width at half maximum (FWHM) of the profile taken in a ROI that includes the gap of the square plate.

3.4.2.2 Measuring the SNR

The SNR can be measured by taking the signal (S) to be the mean pixel intensity value in the ROI, and the noise to be the standard deviation (σ) of the pixel intensity of one or multiple ROIs in the background air (free of ghosting artifacts). The SNR is calculated using the following expression:

$$SNR = 0.655 \times \frac{S}{\sigma}. \qquad (3.3)$$

The 0.655 factor is due to the Rician distribution of the background noise in a magnitude image (tending to a Rayleigh distribution as the SNR goes to zero) (50). This arises because noise variations, which can be negative and positive, are all made positive, which artificially reduces σ. In this study, the SNR was evaluated using Equation 3.3, taking slice 49 of the axial T1 phantom image acquired (51, 52). This slice just shows the water filling the cylinder, not showing internal phantom structures.

3.4.2.3 Measuring Geometric Distortions

Geometric variations due to, for example, possible **B₀** inhomogeneity or gradients' instabilities, were evaluated qualitatively using the images of the hole pattern plate and of the hole pattern present in the block where the fiber bundles were fixed. The holes' geometry was checked both in T1 and T2 images.

3.4.2.4 Spatial Resolution Evaluation

Spatial resolution was estimated from the blocks with different hole sizes, located above the squared plates used to measure slice thickness. We evaluated the smallest size of hole visualized in each block.

3.4.2.5 DTI Quality Control

The QC of DTI acquisitions, for residual error evaluation and detection of significant outliers was done using the ExploreDTI software, as described in Section 3.1.2. For all images acquired, the QC and data processing steps were analogous as previously described. Subsequently, the DTIi were calculated for each fiber bundle, for acquisitions using b = 1000 s/mm^2 and b = 2500 s/mm^2. CV values of DTIi were then estimated to evaluate the phantom stability through b variation and the tracts were reconstructed.

4 RESULTS AND DISCUSSION

4.1 PRE-PROCESSING: DTI ACQUISITION QUALITY CONTROL

Before any DTIi calculation or tracts' reconstruction, in all steps of the study, the acquisitions' QC was done using the ExploreDTI software. In this step, residual error graphs and outliers' percentage graphs were calculated, as well as residual maps. Figures 4.1 - 4.6 show the graphs of residual errors obtained for the DT images of the phantom described in Section 3.1 in the experiments to determine how acquisition parameter changes influence the calculated DTIi, when NDGD was changed for 8-channel and 32-channel head coils. The reference parameters mentioned are the values applied in most of clinical protocols.
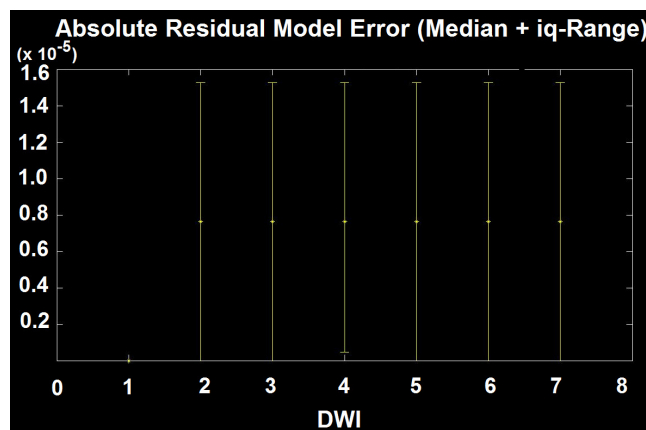
Figure 4.1 – Residual Error Graph for DT image acquired changing NDGD, for the 8-channel coil and NDGD = 6. The reference parameter was NDGD = 32.
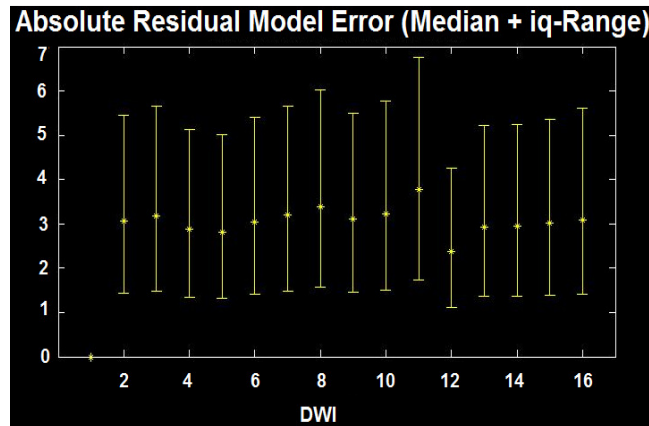
Figure 4.2 – Residual Error Graph for DT image acquired changing NDGD, for the 8-channel coil and NDGD = 15. The reference parameter was NDGD = 32.

Figure 4.3 – Residual Error Graph for DT image acquired changing NDGD, for the 8-channel coil and NDGD = 32 (the reference parameter).
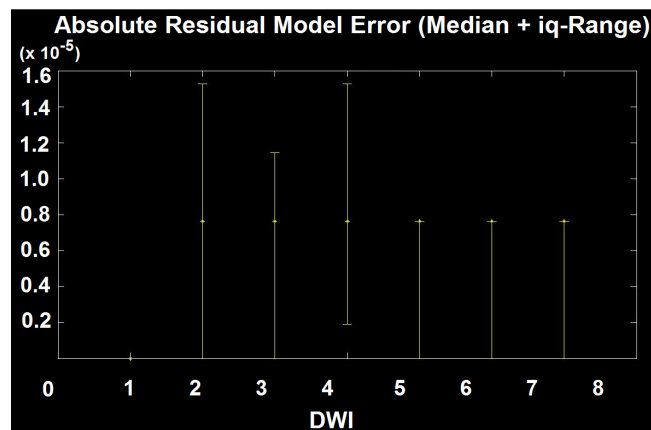
Figure 4.4 - Residual Graph for DT image acquired changing NDGD, for the 32-channel coil and NDGD = 6. The reference parameter was NDGD = 32.
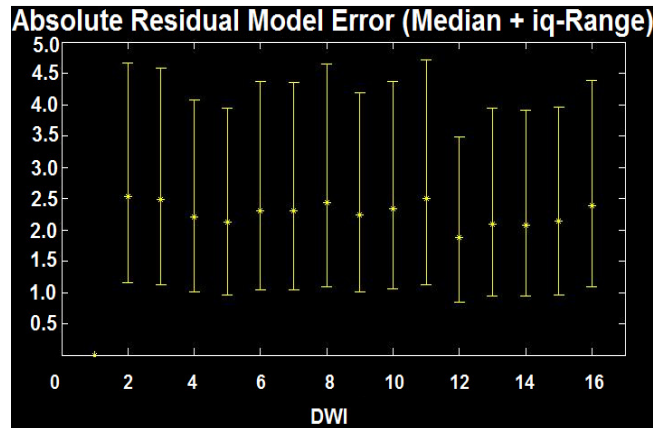
Figure 4.5 – Residual Error Graph for DT image acquired changing NDGD, for the 32-channel coil and NDGD = 15. The reference parameter was NDGD = 32.
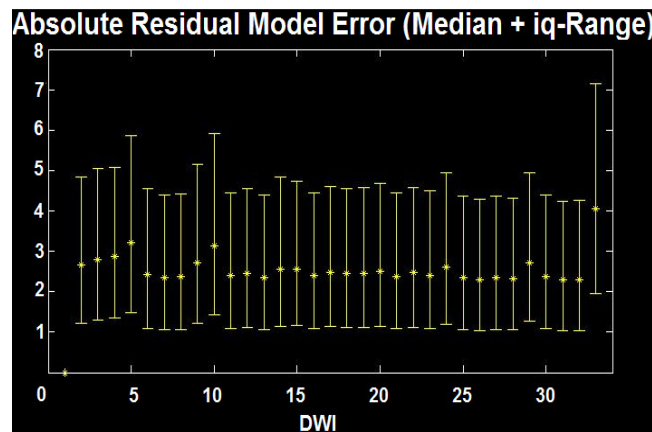
Figure 4.6 – Residual Error Graph for DT image acquired changing NDGD, for the 32-channel coil and NDGD = 32 (the reference parameter).

Recalling that the DWI protocols used acquire DW images in 32 directions, it was observed that the highest values of residual errors or outliers found were for DW image number 33, which is the average of all 32 DW images acquired. This was probably due to error propagation from each DW image to this average image. However, the outliers and residual errors found for all acquisitions were not significant to compromise the results of the analysis. Images that had higher residuals or outliers were discarded.

Despite not existing an established acceptance limit for residual values of DW images or for their ranges for a given DTI acquisition, it is known that residual values must be as small as possible, with minimum variations. For all acquisition parameter changes, the values of the residues' medians were approximately the same (2.5 to 3), for both coils tested. However, for acquisitions with lower NDGD (6 directions), these values were almost 1,000.000 times smaller ($\sim 5 \times 10^{-6}$), as observed in Figures 4.1 and 4.4. It is not

known why this occurs, but the residual values observed are close to those found for the T2 image, the number 1 DW image of all acquisitions. The reduction in the residual error for a smaller NDGD may be due to the lower total duration and magnitude of the diffusion gradients applied, generating less eddy-currents and signal variations (53); but in any case, this must be better investigated.

Figures 4.7-4.9 show the axial residual error maps for DW images acquired changing b-value, for 8-channel head coil. Figures 4.10-4.12 show these maps when the voxel size change, for the same coil. The color bar indicates the magnitude of residual errors. The higher magnitudes of residual errors correspond to clearer points in the images. It is expected that the fiber bundles show higher magnitudes, being highlighted in these maps. The values taken as reference are the most applied in clinical protocols.
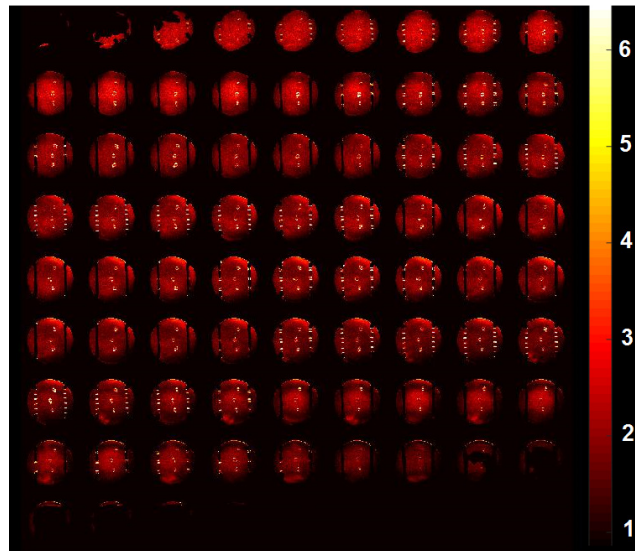
Figure 4.7 – Axial Residual Error Maps for DW images acquired changing the b-value for the 8-channel head coil. b-value applied: 500 s/mm^2. Reference for the b-values: b = 1000 s/mm^2.
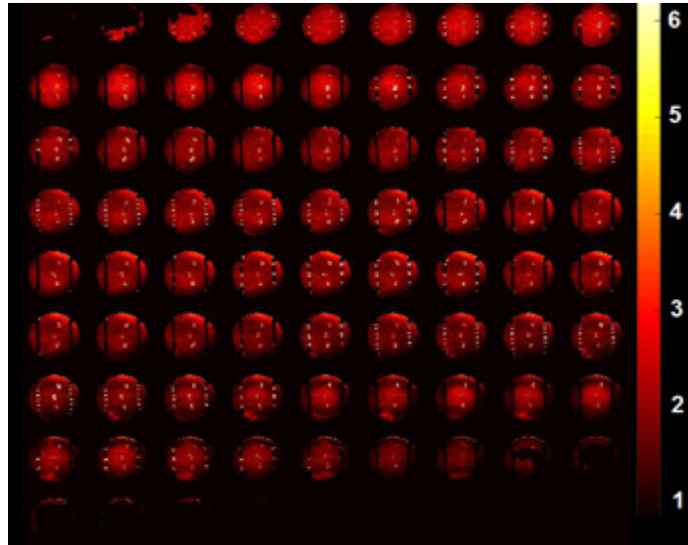
Figure 4.8 - Axial Residual Error Maps for DW images acquired changing the b-value for the 8-channel head coil. b-value applied: 1000 s/mm². This is the reference for b-values.
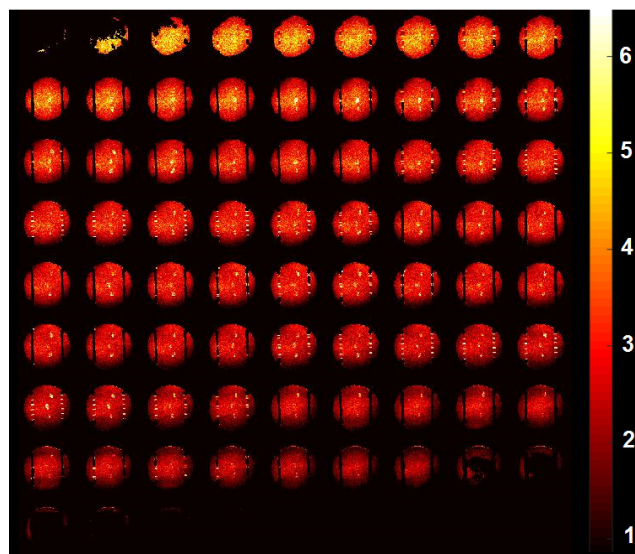
Figure 4.9 - Axial Residual Error Maps for DW images acquired changing the b-value for the 8-channel head coil. b-value applied: 2500 s/mm². Reference for the b-values: b = 1000 s/mm².
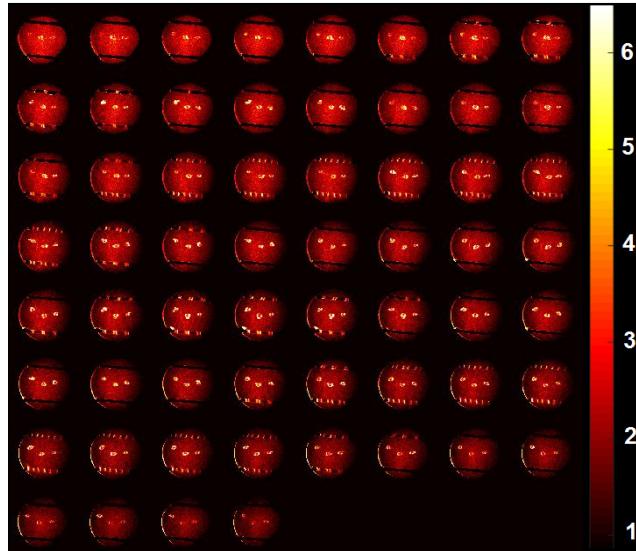
Figure 4.10 - Axial Residual Error Maps for DW images acquired changing the voxel size for the 8-channel head coil. Voxel size applied: 1 mm × 1 mm × 1 mm. Reference for the voxel size: 2 mm × 2 mm × 2 mm.
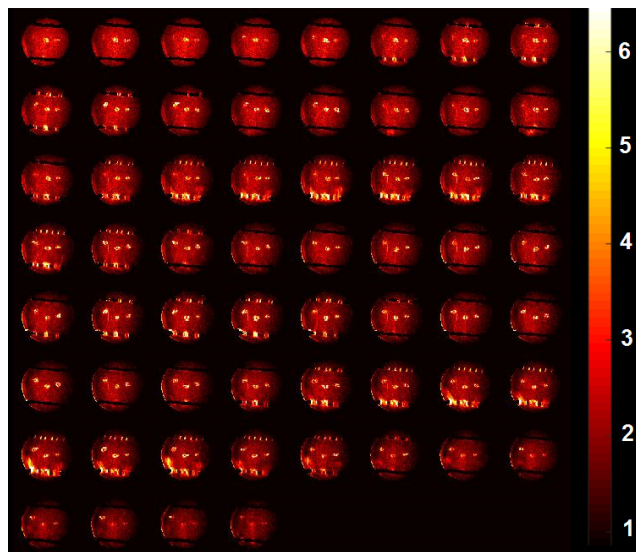
Figure 4.11 - Axial Residual Error Maps for DW images acquired changing the voxel size for the 8-channel head coil. Voxel size applied: 2 mm × 2 mm × 2 mm. This is the reference for the voxel size.
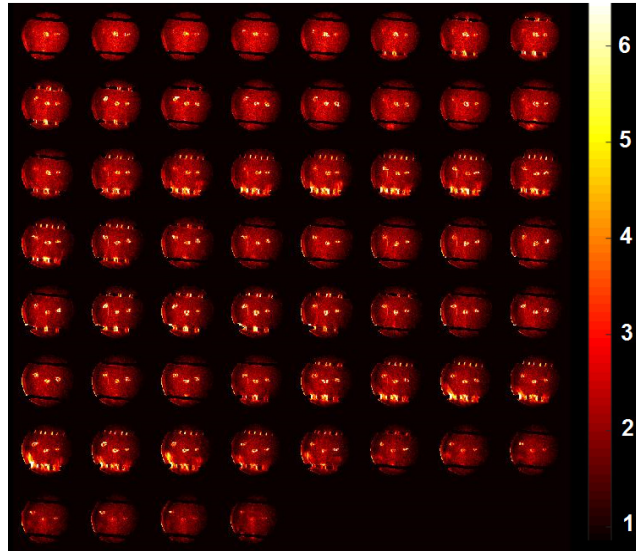
Figure 4.12 - Axial Residual Error Maps for DW images acquired changing the voxel size for the 8-channel head coil. Voxel size applied: 3 mm × 3 mm × 3 mm. Reference voxel size: 2 mm × 2 mm × 2 mm.

From the residual error maps seen in Figures 4.10-4.12, it is possible noting that for larger voxel size the residual error maps show a blurring effect (Figure 4.12). For higher b-value, geometric distortions are observed (Figure 4.9). On the other side, the stronger diffusion-weighting for images acquired using b = 2500 s/mm^2 increases the signal from fiber bundles given that this image acquisition is more sensitive to water diffusion information. Lower NDGD values lead to residual error maps almost homogeneous, corroborating the residual error values seen in the graphs of Figures 4.1 and 4.4. The increase of NDGD created more geometric distortions at residual error maps, given the amount and duration of diffusion gradients applied. For other acquisition parameter changes, there are no other significant findings about residual values.

Figures 4.13-4.15 show the graphs of outliers' percentage for DW images when the b-value is changed, for each slice plane, and the total percentage, considering all planes. It is observed that increasing b-value, the outliers' percentage increases. It may due to higher amplitude of the diffusion gradients applied, which have as advantage an improvement of CNR (9, 47, 54).
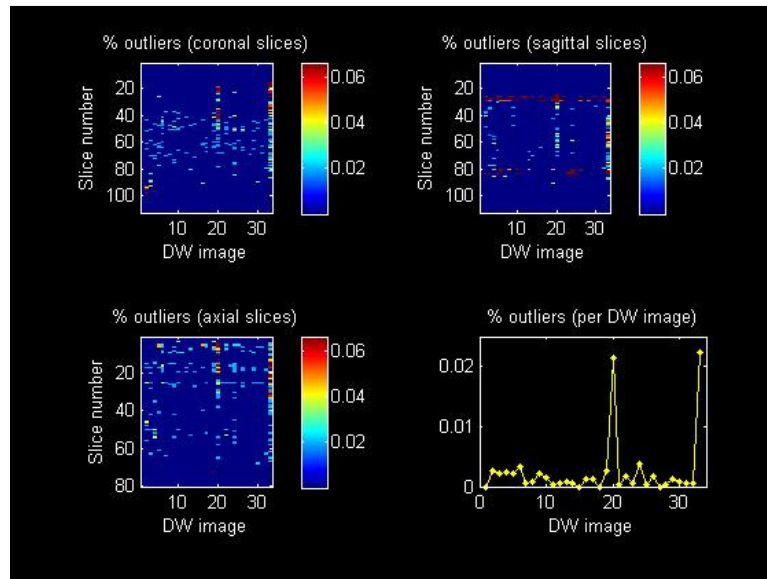
Figure 4.13 - Graphs of Outliers' Percentage for DW images acquired changing b, for the 8-channel coil. b-value applied 500 s/mm². Reference for b-values: b = 1000 s/mm².
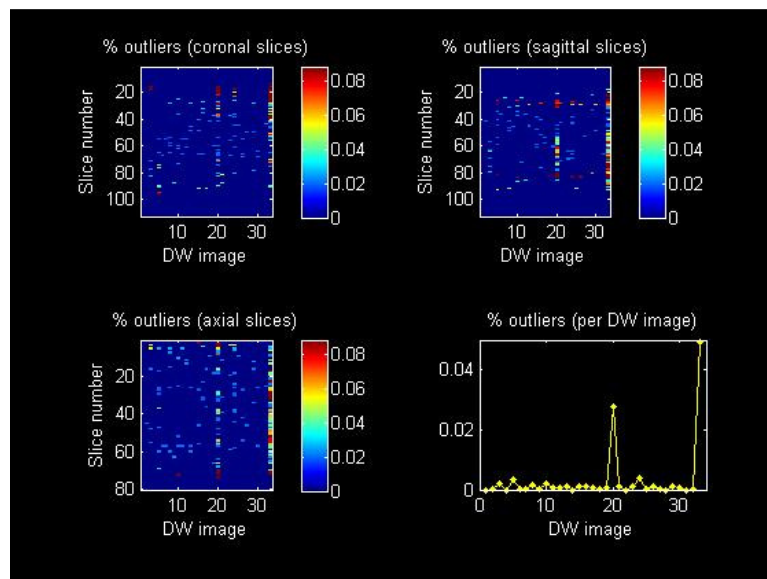
Figure 4.14 - Graphs of Outliers' Percentage for DW images acquired changing b, for the 8-channel coil. b-value applied 1000 s/mm². This is the reference for b-values.
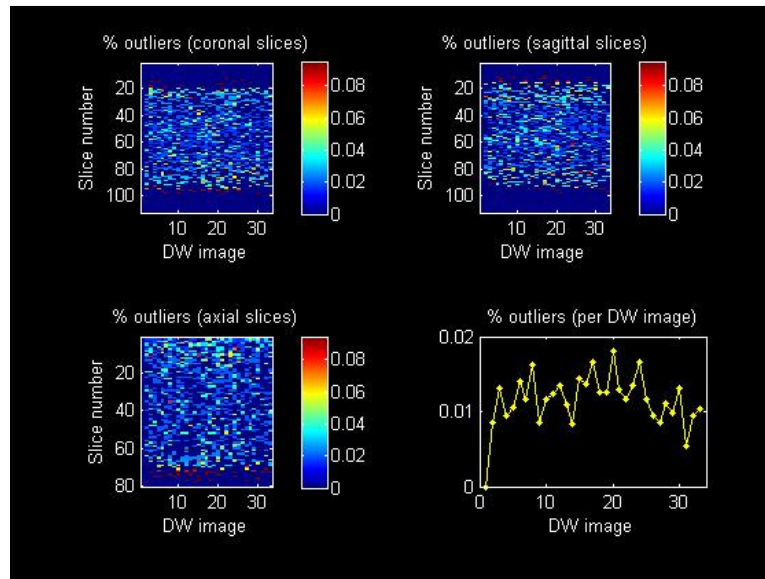
Figure 4.15 - Graphs of Outliers' Percentage for DW images acquired changing b, for the 8-channel coil. b-value applied 2500 s/mm^2. Reference: b = 1000 s/mm^2.

The outliers' percentages found for all acquisitions were lower than 0.1%, which seems acceptable considering the complexity of the presented processes. In many acquisitions, the DW image number 10 showed higher outliers' percentages. This is probably due to directional variations, although there are no significant variations in the magnitude of the diffusion gradients applied in the acquisition of this DWI. This did not occur for DTI using less directions. The DW image number 33, which is the average of all DW images, showed higher outliers' percentage for all acquisitions. Knowledge of the way in which the diffusion gradients were applied and switched in this scanner could help to explain these occurrences.

4.2 FIRST PHANTOM STUDY: INFLUENCE OF ACQUISITION PARAMETERS ON DTII FOR THE 8 AND 32-CHANNEL HEAD COILS

In this section, the results regarding the influence of different acquisition parameters on the DTIi shown in Table 2.1, for the first phantom built, are presented. The objectives of experiments were to evaluate how the acquisition parameters can compromise the DTIi and verify if Dyneema® fishing lines are suitable to build fiber bundles whose FA values are similar to found in brain tracts. There are few studies, performed with human beings or

phantoms, that explore correlations between acquisition parameters, number of coil channels or field intensity and DTIi and most of them were in general focused on MD and FA analysis (55-57). Besides these DTIi being the most used in human brain studies, it is also important to evaluate acquisition parameters' correlations to other DTIi, which bring us information about diffusion geometry, because they are very susceptible to bias due to eddy-currents. Therefore, in addition to MD and FA, this step of the study also evaluated the influence of acquisition parameters on RA, VR, CS, CL and CP.

It is expected that changes in acquisition parameters directly related to diffusion-weighting lead to more variations in the DTIi. Besides acquisition parameters related to diffusion, the other parameters were studied due to their association to SNR, geometry, signal acquisition and codification, and because they are frequently manipulated at clinical and research protocols. It is not expected that changes in these parameters lead to significant changes in DTIi, even though some of them (TE, NSA and SENSE) have influence in the signal.

Figures 4.16 and 4.17 show the mean and standard deviations of each DTIi when the acquisition parameters are changed, for the three Dyneema® fiber bundles described in Section 3.1, and both head coils. For the 8-channel head coil, the FA values for bundle 1, 2 and 3, were, respectively, (0.33 ± 0.01), (0.36 ± 0.02) and (0.42 ± 0.02) (Figure 4.16). For the 32-channel coil, the values were (0.31 ± 0.02), (0.34 ± 0.01) and (0.39 ± 0.02) respectively, considering all acquisition parameter variations. It is known that for the main white matter tracts of the normal brain, the FA values range from 0.4 to 0.8 (58, 59). Thus, the values found here are near to the range found in brain tissues and in the range of cardiac muscle (7, 60). A better compression of bundles tends to improve the FA values, bringing them close to those found in human brain tracts (59). This was indeed done in further experiments, with results described in the next sections. The geometric parameters CS and CL did not show significant differences for different bundles and coils. However, the voxel size variation led to higher CV values of CP for bundles 2 and 3, in the 8-channel head coil. This acquisition parameter is related to spatial resolution and its shape and dimension may affect DTIi. Increasing the voxel size, the number of structures inside it increases, which may lead to changes in tensor geometry and their DTIi. This is relevant especially when the density of fibers or structures per voxel increases or there are crossing fibers in a voxel.

Figures 4.18 and 4.19 show the CV values of DTIi, for all bundles, coils and acquisition parameters varied. Higher CV values were found for the 32-channel head coil and the

DTIi CS, CL and CP, when NSA was changed, for bundle 2 (Figure 4.19). Among these values, the highest CV was observed for CP (3.29). The geometric DTIi (CS, CL and CP) seem more susceptible to variations in DTI acquisition parameters, specially NSA and voxel size. Increasing NSA, the SNR increases, leading to better tensor estimation given a geometry and magnitude. Thus, variations in geometric DTIi because of NSA variation may occur. NSA variations also lead to higher CV values in RA and VR for bundle 3 and for the 32-channel head coil (Figure 4.18). For coils with a higher number of channels, the probability of occurrence of different responses to signal by each channel increases, which may lead to changes in DTIi related to the magnitude of the tensor.
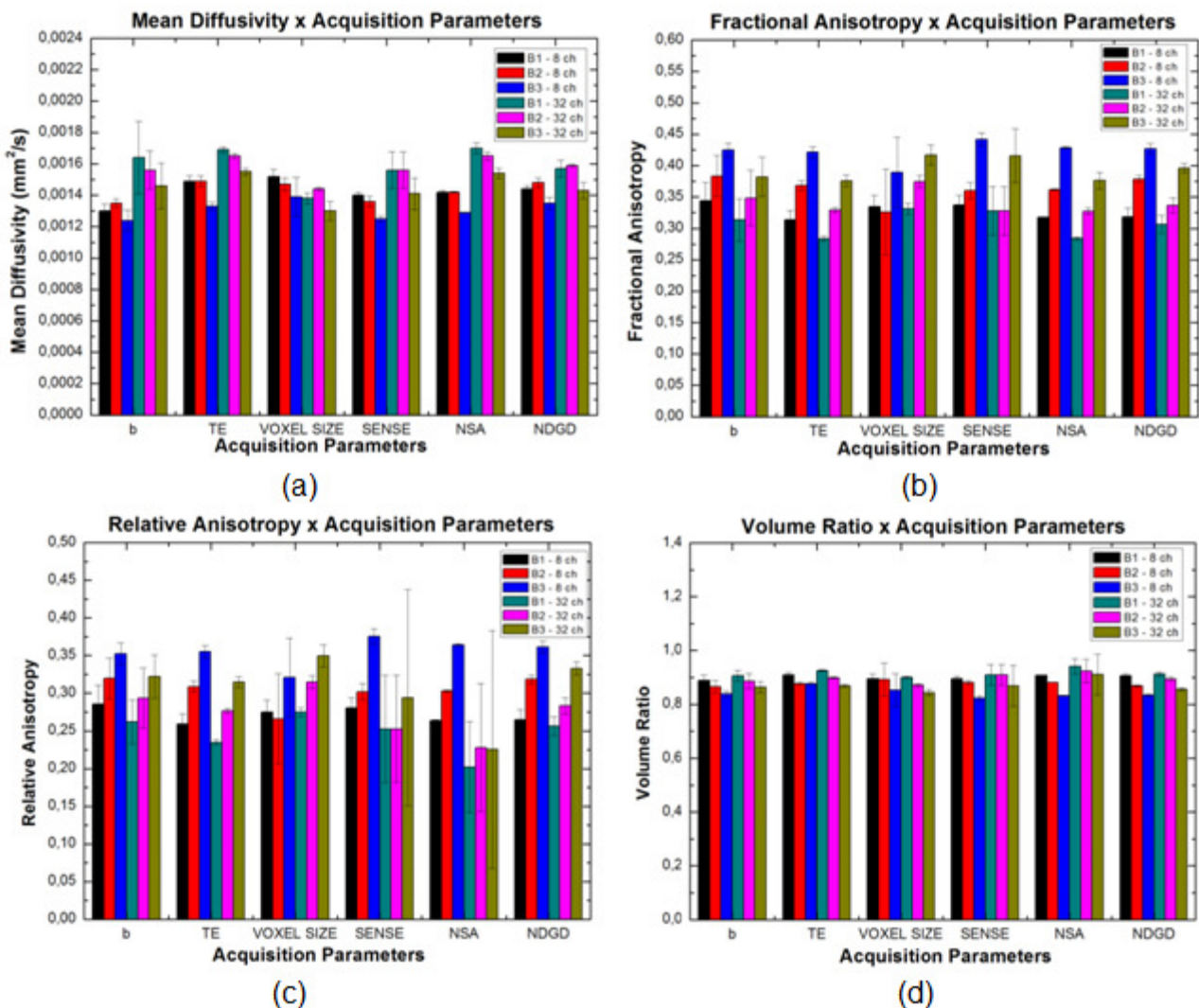
Figure 4.16 - Mean and Standard deviation for (a) MD, (b) FA, (c) RA and (d) VR, for all coils and fiber bundles. Black: fiber bundle 1, red: fiber bundle 2, blue: fiber bundle 3, all for the 8-channel coil; green: bundle 1, pink: bundle 2, brown: bundle 3, all for the 32-channel coil.
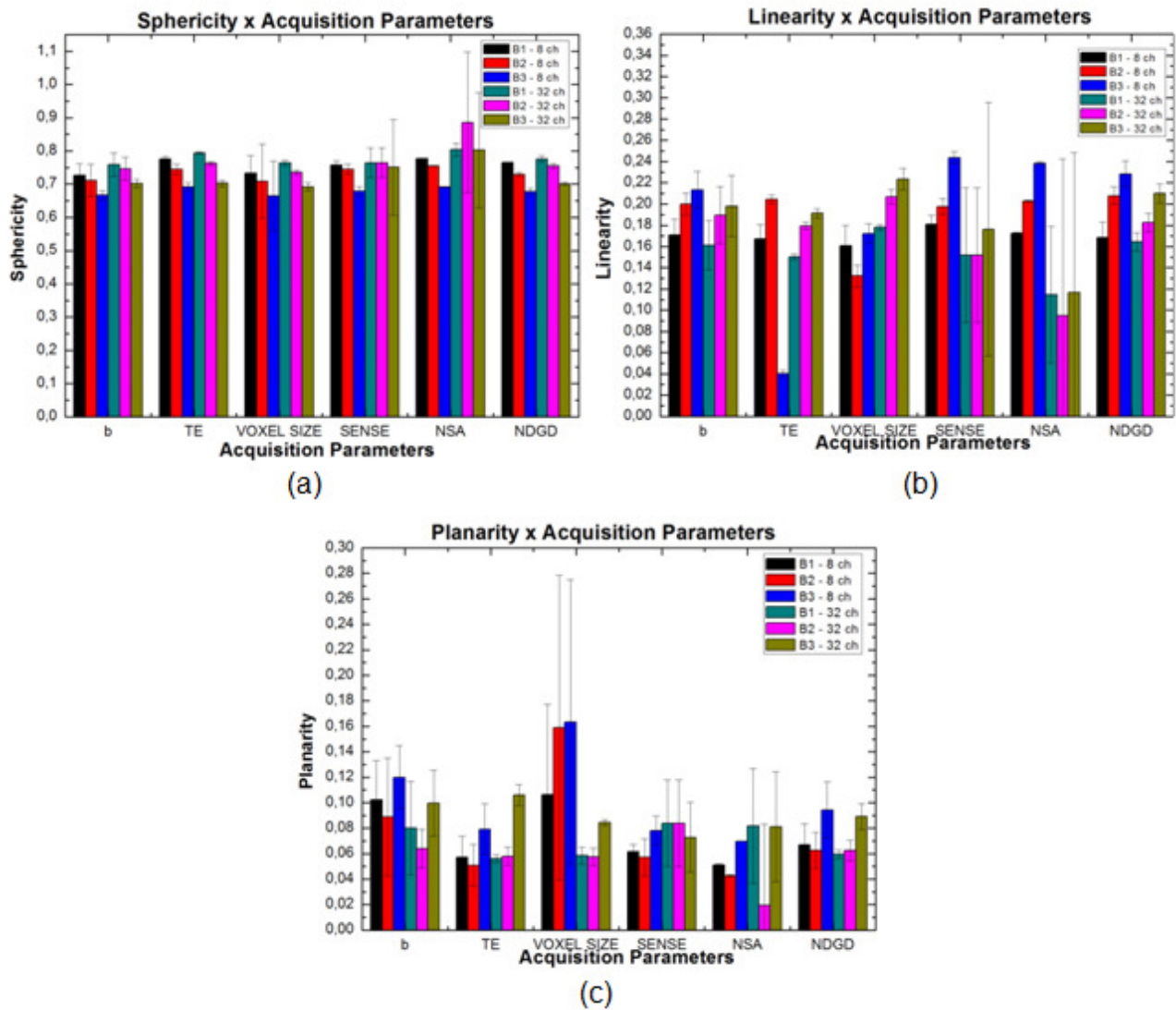
Figure 4.17 - Mean and Standard deviation for (a) CS, (b) CL and (c) CP, for all coils and fiber bundles. The color scale is the same as in Figure 4.16.
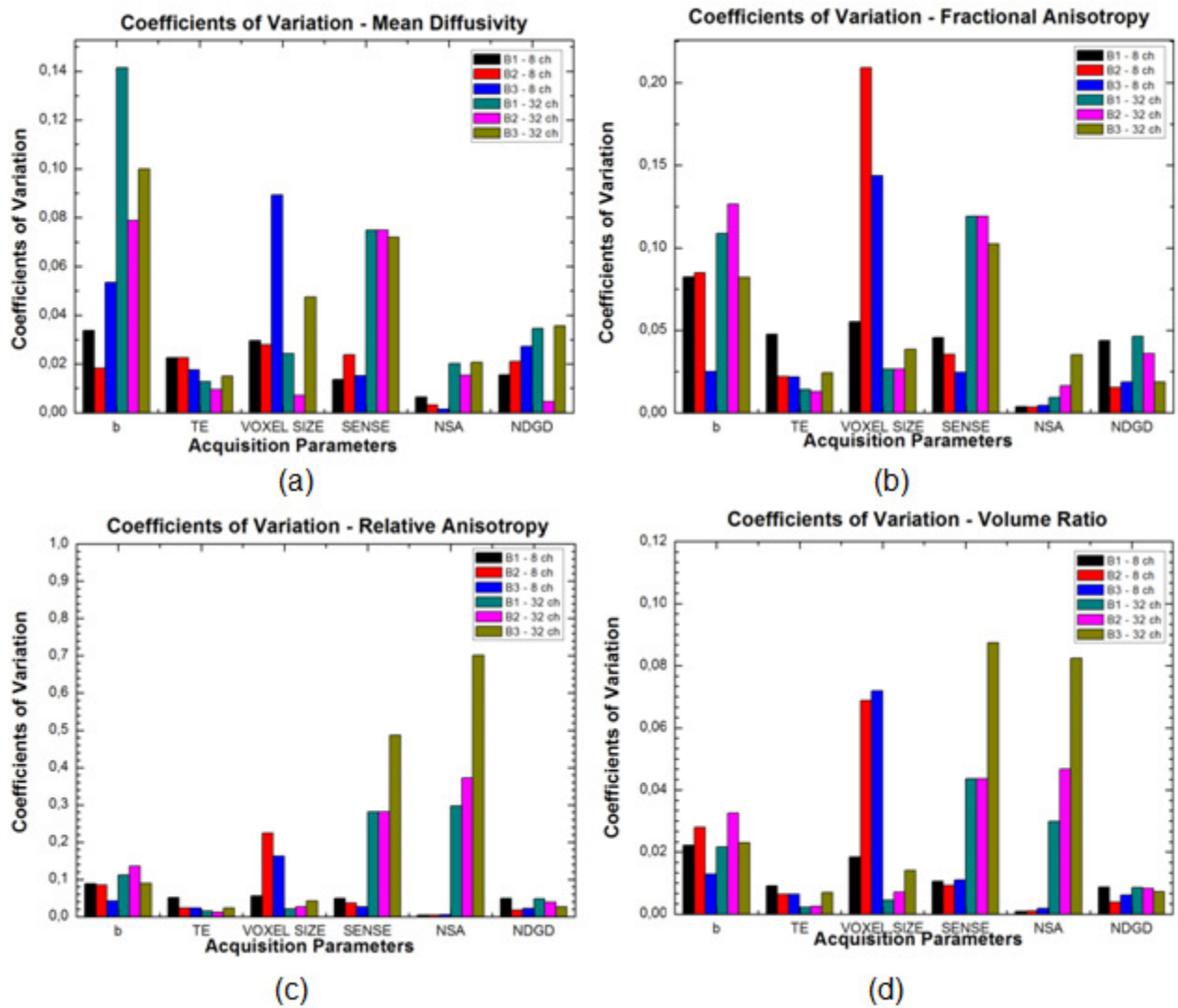
Figure 4.18 - Coefficients of Variation for (a) MD, (b) FA, (c) RA and (d) VR, for all coils and fiber bundles. The color scale is the same as in Figure 4.16.
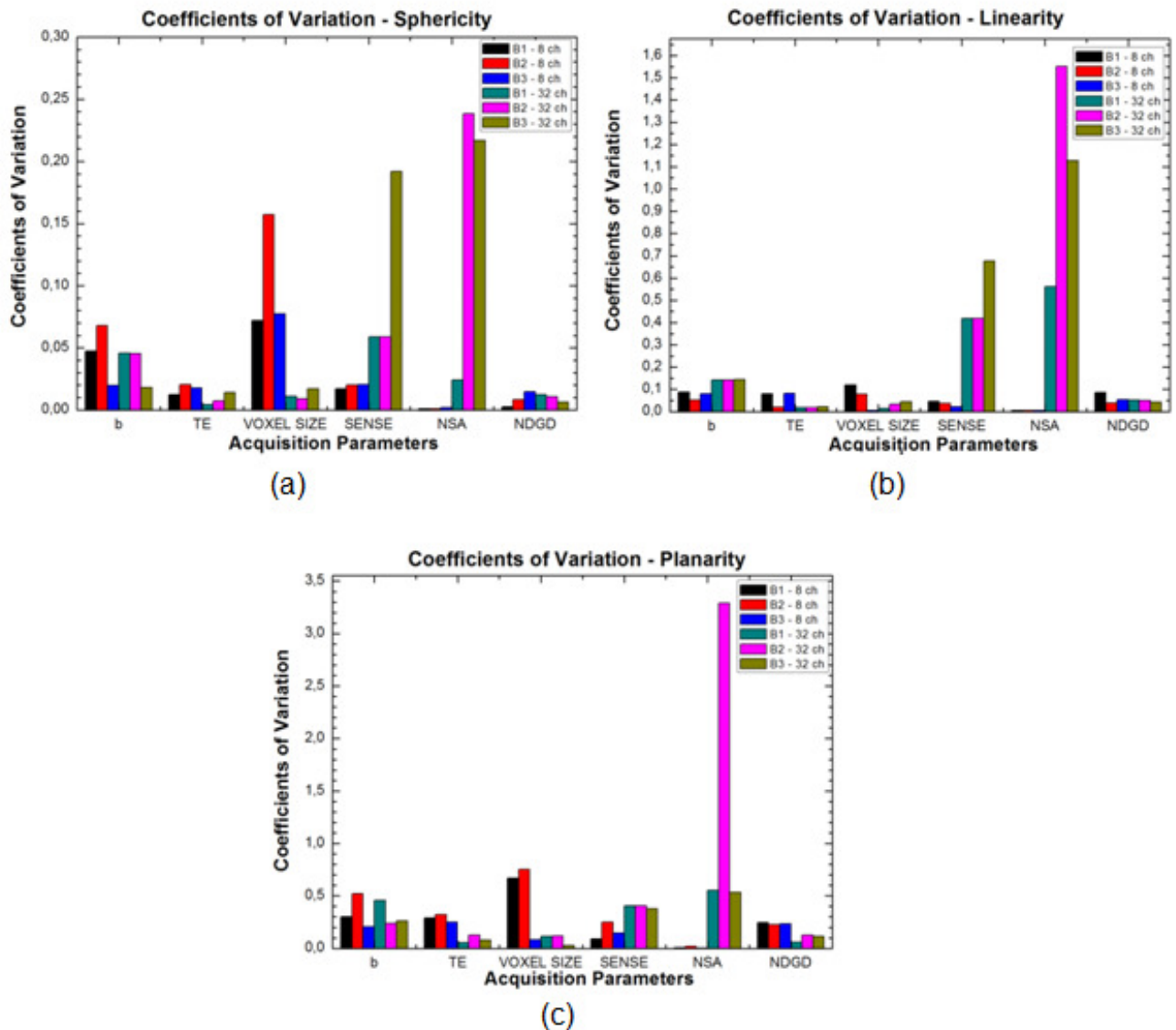
Figure 4.19 - Coefficients of Variation for (a) CS, (b) CL and (c) CP, for all coils and fiber bundles. The color scale is the same as in Figure 4.16.

Tables 4.1 and 4.2 describe, respectively, the results of Spearman's correlation analysis to estimate correlations between acquisition parameters and DTIi values. A non-parametric statistical test was chosen because some data sets follow a Gaussian distribution and others do not. Figures 4.20 and 4.21 bring the correlation graphs for acquisitions using the 8 and 32-channel head coils, respectively.

Table 4.1 - Correlations of MRI scan parameters and DTIi for 8-channel coil.

Scan parameter	Bundle	Spearman's Correlation Parameter	MD	FA	RA	VR	CS	CL	CP
b	1	Rho	-.393	.643	.643	-.643	-.393	.893**	.214
		Sig. (2 tales)	.383	.119	.119	.119	.383	.007	.645
		N	7	7	7	7	7	7	7
	2	Rho	.607	1.000**	1.000**	-1.000**	-.786*	.643	.643
		Sig. (2 tales)	.148				.036	.119	.119
		N	7	7	7	7	7	7	7
	3	Rho	.071	.107	-.357	.286	0.000	-.500	.393
		Sig. (2 tales)	.879	.819	.432	.535	1.000	.253	.383
		N	7	7	7	7	7	7	7
TE	1	Rho	-.700	.700	.700	-.700	.100	.700	-.400
		Sig. (2 tales)	.188	.188	.188	.188	.873	.188	.505
		N	5	5	5	5	5	5	5
	2	Rho	-.300	-.100	-.100	.100	.400	.700	-.700
		Sig. (2 tales)	.624	.873	.873	.873	.505	.188	.188
		N	5	5	5	5	5	5	5
	3	Rho	-.300	.600	.600	-.600	.400	.700	-.900*
		Sig. (2 tales)	.624	.285	.285	.285	.505	.188	.037
		N	5	5	5	5	5	5	5
NSA	1	Rho	.500	1.000**	1.000**	-1.000**	-1.000**	1.000**	-.500
		Sig. (2 tales)	.667						.667
		N	3	3	3	3	3	3	3
	2	Rho	.500	1.000**	1.000**	-1.000**	-1.000**	1.000**	-.500
		Sig. (2 tales)	.667						.667
		N	3	3	3	3	3	3	3
	3	Rho	-1.000**	1.000**	1.000**	-1.000**	-1.000**	1.000**	-1.000**
		Sig. (2 tales)							
		N	3	3	3	3	3	3	3
VOXEL	1	Rho	-.400	-.400	-.400	.400	.900*	1.000**	-1.000**
		Sig. (2 tales)	.505	.505	.505	.505	.037		
		N	5	5	5	5	5	5	5
	2	Rho	.600	-.700	-.700	.700	.900*	1.000**	-.900*
		Sig. (2 tales)	.285	.188	.188	.188	.037		.037
		N	5	5	5	5	5	5	5
	3	Rho	1.000**	-1.000**	-1.000**	1.000**	1.000**	.700	-1.000**
		Sig. (2 tales)						.188	
		N	5	5	5	5	5	5	5
SENSE	1	Rho	-.179	.929**	.929**	-.929**	-.857*	.964**	.500
		Sig. (2 tales)	.702	.003	.003	.003	.014	.000	.253
		N	7	7	7	7	7	7	7
	2	Rho	-.714	0.000	0.000	0.000	-.786*	-.464	.857*
		Sig. (2 tales)	.071	1.000	1.000	1.000	.036	.294	.014
		N	7	7	7	7	7	7	7
	3	Rho	-.714	.036	.071	0.000	.107	-.107	.071
		Sig. (2 tales)	.071	.939	.879	1.000	.819	.819	.879
		N	7	7	7	7	7	7	7
NDGD	1	Rho	-1.000**	1.000**	1.000**	-1.000**	1.000**	1.000**	-1.000**
		Sig. (2 tales)							
		N	3	3	3	3	3	3	3
	2	Rho	-1.000	1.000	1.000	-1.000	1.000	1.000	-1.000
		Sig. (2 tales)	.	.	.	.	.	.	.
		N	3	3	3	3	3	3	3
	3	Rho	-1.000**	.500	.500	-.500	1.000**	1.000**	-1.000**
		Sig. (2 tales)		.667	.667	.667			
		N	3	3	3	3	3	3	3

* The correlation is significant at level 0.05 (2-tailed test). ** The correlation is significant at level 0.01 (2-tailed test)

Figure 4.20 - Scatter plots showing the correlations between acquisition parameters and DTIi for bundles (a) 1, (b) 2 and (c) 3, for the 8-channel coil.

It was observed that there is a higher number of correlations between acquisition parameters and DTIi for the 8-channel head coil and bundle 1 (Table 4.1), for which NDGD

changes are correlated to variations in all DTIi (positive correlations with FA, RA, CS and CL; negative correlations with MD, VR and CP) (Figure 4.19). For this bundle and coil, the SENSE factor and NSA show correlations with all DTIi, except MD, and the geometric indices (CS, CL and CP) are correlated to voxel size (Table 4.1). The voxel size is also correlated to all DTIi for bundle 3 in the 8-channel coil (positive correlation with MD, VR and CS; negative correlation with FA, RA and CP), and to geometric DTIi for bundles 1 and 2 in the same coil (Figure 4.19). Most axon fibers have diameter of a few microns and axon tracts may have diameter of dozens of microns (61), being smaller than the thinnest fiber bundle of this study (bundle 1). Given that this bundle presented the highest number of correlations between acquisition parameters and DTIi, it is important to carefully change the acquisition protocols, as well as avoiding comparisons of data acquired with different setups, without knowledge of data correspondence (without an accurate cross calibration), mainly in studies of low diameter fiber tracts.

Table 4.2 - Correlations of MRI scan parameters and DTIi for 32-channel coil.

Scan parameter	Bundle	Spearman's Correlation Parameter	MD	FA	RA	VR	CS	CL	CP
b	1	Rho	-1.000**	.786*	.786*	-.643	-.214	1.000**	0.000
		Sig. (2 tales)		.036	.036	.119	.645		1.000
		N	7	7	7	7	7	7	7
	2	Rho	-.750	.964**	1.000**	-.964**	-.750	1.000**	.107
		Sig. (2 tales)	.052	.000		.000	.052		.819
		N	7	7	7	7	7	7	7
	3	Rho	-1.000**	.786*	.786*	-.643	-.214	1.000**	0.000
		Sig. (2 tales)		,036	,036	,119	,645		1,000
		N	7	7	7	7	7	7	7
TE	1	Rho	-,700	,700	,700	-,700	,100	,700	-,400
		Sig. (2 tales)	,188	,188	,188	,188	,873	,188	,505
		N	5	5	5	5	5	5	5
	2	Rho	.429	.943**	.886*	-.886*	-.257	.600	-.200
		Sig. (2 tales)	.397	.005	.019	.019	.623	.208	.704
		N	6	6	6	6	6	6	6
	3	Rho	.829*	.829*	.657	-.829*	-.771	.371	.943**
		Sig. (2 tales)	.042	.042	.156	.042	.072	.468	.005
		N	6	6	6	6	6	6	6
NSA	1	Rho	.500	-.500	-.500	.500	.500	.500	-.500
		Sig. (2 tales)	.667	.667	.667	.667	.667	.667	.667
		N	3	3	3	3	3	3	3
	2	Rho	.500	-.500	-.500	.500	.500	-.500	.500
		Sig. (2 tales)	.667	.667	.667	.667	.667	.667	.667
		N	3	3	3	3	3	3	3
	3	Rho	-.500	-1.000**	-.500	.500	.500	-.500	-.500
		Sig. (2 tales)	.667		.667	.667	.667	.667	.667
		N	3	3	3	3	3	3	3
VOXEL	1	Rho	-.949	.316	.316	-.316	-.316	.949	.316
		Sig. (2 tales)	.051	.684	.684	.684	.684	.051	.684
		N	4	4	4	4	4	4	4
	2	Rho	.316	-.316	-.316	.316	-.632	-.316	.949
		Sig. (2 tales)	.684	.684	.684	.684	.368	.684	.051
		N	4	4	4	4	4	4	4
	3	Rho	-.632	.316	.316	-.316	-.316	.316	-.316
		Sig. (2 tales)	.368	.684	.684	.684	.684	.684	.684
		N	4	4	4	4	4	4	4
SENSE	1	Rho	-.700	.400	.400	-.400	-.300	.400	.600
		Sig. (2 tales)	.188	.505	.505	.505	.624	.505	.285
		N	5	5	5	5	5	5	5
	2	Rho	.500	-.200	-.200	.200	-.100	-.800	.100
		Sig. (2 tales)	.391	.747	.747	.747	.873	.104	.873
		N	5	5	5	5	5	5	5
	3	Rho	-.300	.300	.300	-.300	-.300	.300	0.000
		Sig. (2 tales)	.624	.624	.624	.624	.624	.624	1.000
		N	5	5	5	5	5	5	5
NDGD	1	Rho	-1.000**	-.500	-.500	.500	.500	-.500	-1.000**
		Sig. (2 tales)		.667	.667	.667	.667	.667	
		N	3	3	3	3	3	3	3
	2	Rho	-1.000**	-.500	-.500	.500	1.000**	-.500	-.500
		Sig. (2 tales)		.667	.667	.667		.667	.667
		N	3	3	3	3	3	3	3
	3	Rho	-1.000**	-.500	-.500	.500	1.000**	-.500	-.500
		Sig. (2 tales)		.667	.667	.667		.667	.667
		N	3	3	3	3	3	3	3

* The correlation is significant at level 0.05 (2-tailed test). ** The correlation is significant at level 0.01 (2-tailed test)
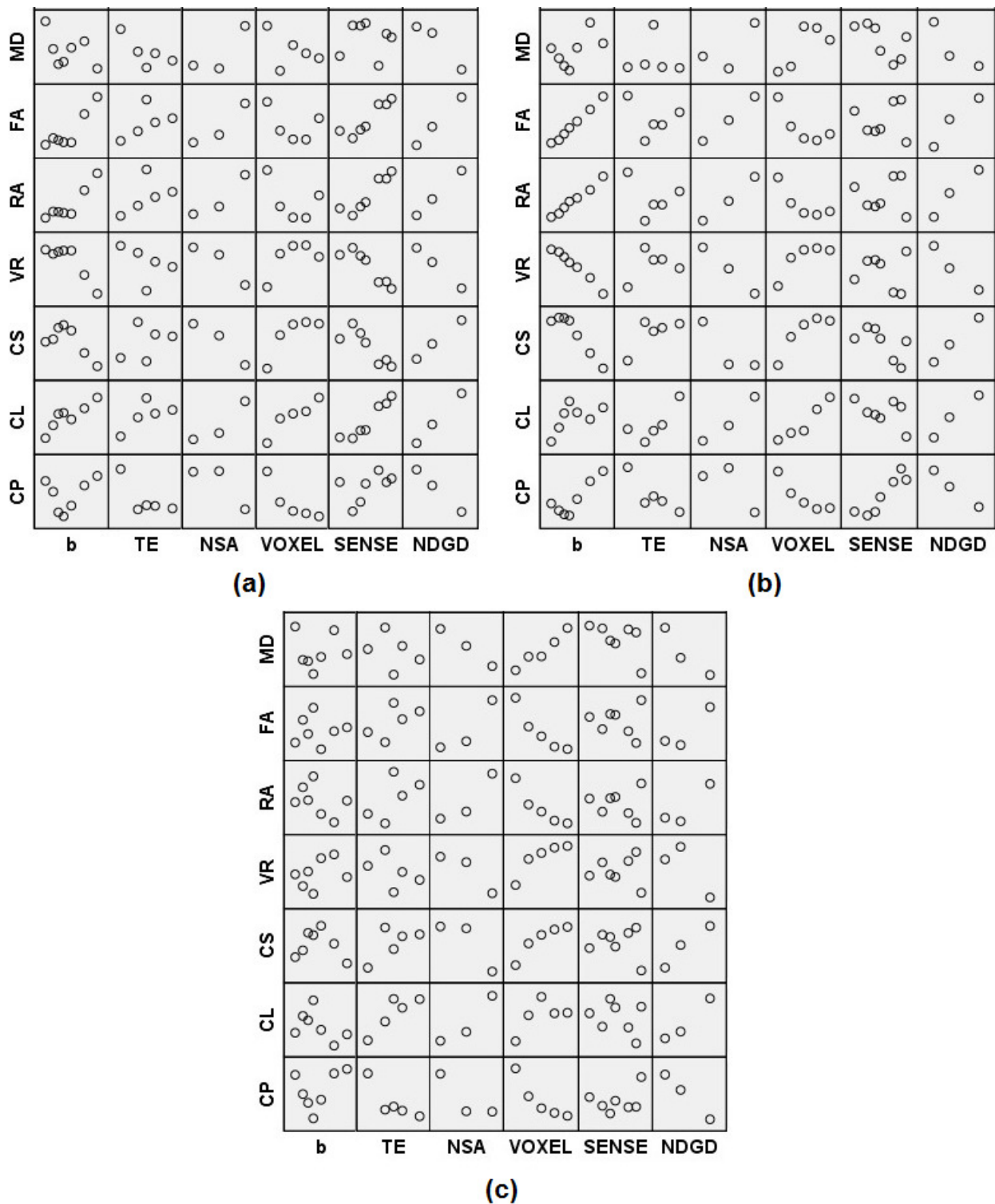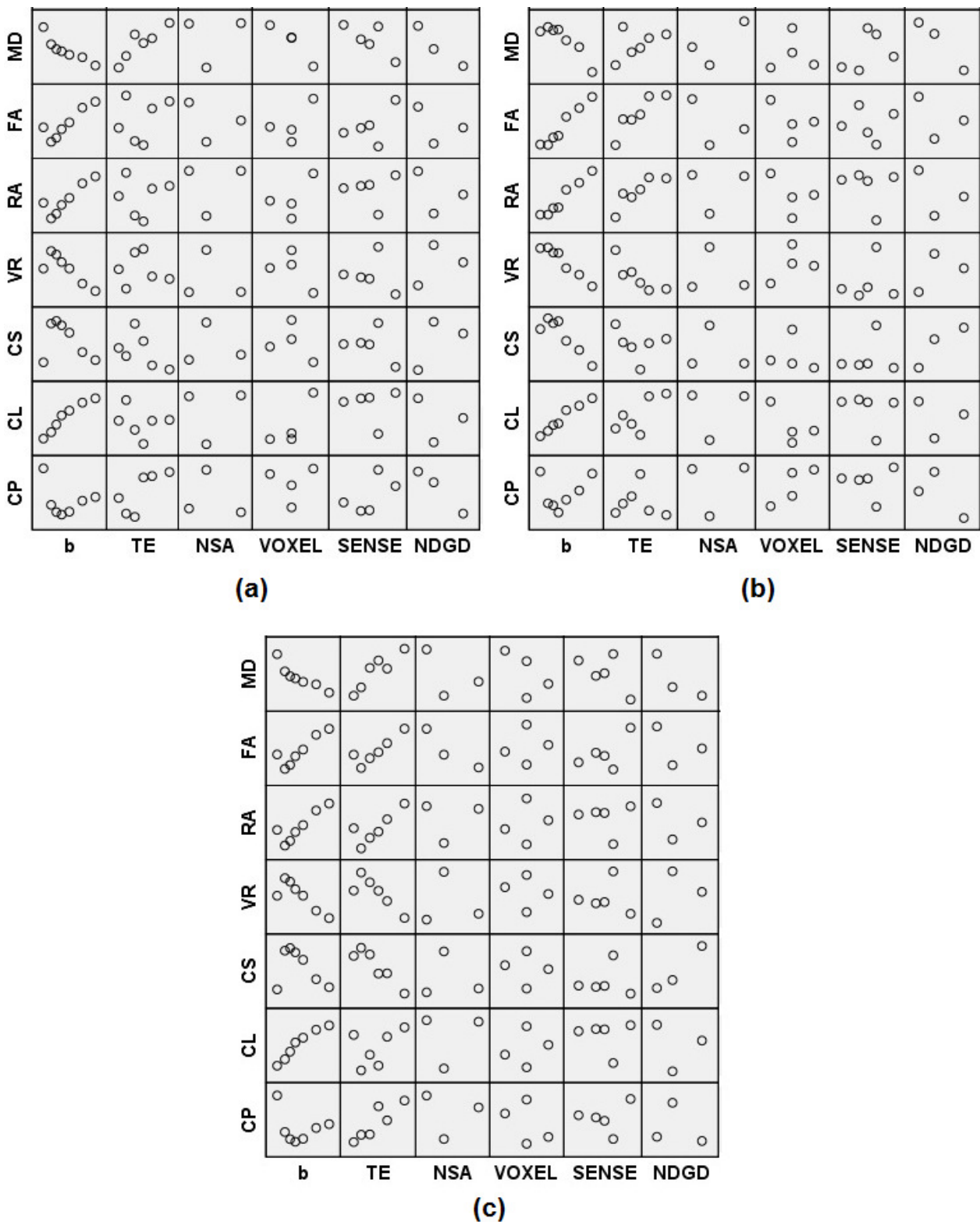
Figure 4.21 - Scatter plots showing the correlations between acquisition parameters and DTIi for bundles (a) 1, (b) 2 and (c) 3, for the 32-channel coil.

Figures 4.20 and 4.21 show significant correlations between b or NDGD (parameters related to diffusion-weighting and tensor calculation) and the DTIi FA, RA and VR, which are related to the magnitude of DTI, as expected. On the other side, voxel size was the parameter predominantly correlated with geometric indexes, which describes the shape of the tensor. Increasing voxel size, the number of structures inside it increases, which can influence the shape of the tensor. The parameter NSA is related to SNR and theoretically it should have low influence on DTIi. However, differences in signal intensities can also lead to changes in DTIi, which must be considered mainly when multi-channel coils are applied. In these coils, this signal intensity variations may lead to contrast degradation and geometric distortions.

The acquisition parameter NDGD exhibits the highest number of correlations with DTIi (24 correlations), most of them for the 8-channel coil and bundles 1 and 2, composed by lower diameter fibers (.25 mm and .35 mm respectively) (Table 4.1). For these bundles and the 8-channel coil, we found negative correlations between NDGD and MD, VR and CP; positive correlations were found for FA, RA, CS and CL (Figure 4.20). For bundle 3, just negative correlations with MD and CP, and positive correlations with CS and CL were found. For the 32-channel coil, there are negative correlations between NDGD and MD and CP for bundle 1, as well as a negative and a positive correlation with MD and CS, respectively, for bundles 2 and 3 (Table 4.2 and Figure 4.21).

On the other hand, b, which is also an acquisition parameter, related to diffusion magnitude, shows the same number of correlations with DTIi as NSA (18), most of them for the 32-channel coil (Figures 4.20 and 4.21). The DTIi more influenced by b are FA, RA and VR, followed by CL and MD. For the 8-channel coil, bundle 2 shows positive correlation between b and FA or RA, and negative correlation between this parameter and VR or CS. Bundle 1 just shows a positive correlation between b and CL. For the 32-channel coil and bundles 1 and 2, there are positive correlations between b and FA, RA or CL; bundle 1 also shows negative correlation between b and MD and bundle 2 between b and VR.

Concerning NSA and the 8-channel coil, there are positive correlations between this parameter and FA, RA or CL and negative correlations with VR and CS, for all bundles. Bundle 3 also shows negative correlations between NSA and MD or CP. For the 32-channel coil, we only found a correlation between this parameter and FA for bundle 3 (Table 4.2).

The voxel size shows more correlations with geometric DTIi, for the 8-channel coil. For bundles 1 and 2, there are positive correlations between this parameter and CS or CL,

and a negative correlation with CP; for bundle 3, there are positive correlations with CS, MD or VR, and negative correlations with RA or CP. For the 32-channel coil no correlation was found.

Correlations between the SENSE factor and DTIi were only found for the 8-channel head coil. For bundle 1, there are positive correlations with FA and CL and negative correlations with RA, VR and CS; for bundle 2, there is a positive correlation with CP and a negative correlation with CS. For bundle 3, there is no correlation between this parameter and DTIi. Possibly, the higher number of channels in the 32-channel head coil tends to improve the SNR, reducing the effect of noise or geometric distortions that may be due to SENSE. The higher number of channels also reduces the noise and distortions due to voxel size variation.

For TE, most correlations were found for the 32-channel coil and bundles 2 and 3. For bundle 2, there are positive correlations with FA or RA and negative correlation with VR; for the bundle 3, we found positive correlations with MD, FA or CP and a negative correlation with VR. For bundle 1, only one correlation was found, between TE and CP, for the 8-channel coil. Diffusion images are T2-weighted, so, variations in DTIi such as MD and FA when TE is changed are expected (62).

Neither the relation between acquisition parameters and DTIi, nor their causes, are yet well-defined. In literature, we can find some reports which explore this subject, specially the relation between acquisition parameters and MD and FA. In general, there is no agreement between different studies because phantoms and acquisition conditions are not the same. The study (42) found no correlations between these DTIi and NSA and MD or FA; other studies (63, 64), (43) found a negative correlation between FA and voxel size and NDGD. Some authors reported a positive correlation between FA and SENSE, b or TE (43, 65, 66), while others reported no correlation (44, 67). Most of those studies used imaging acquisitions of healthy subjects, which is not the best way to explore scanner parameters and performance characteristics, given the variability of human tissues and the fact that we do not know the real body constitution and diffusion aspects of subjects. It is known that depending on the body region or tissue type, different relations between DTI acquisition parameters and DTIi are observed.

Recently, researchers developed a capillary array phantom, measuring 1 cm length and 1 cm in diameter, to be positioned with the patient head inside an 8-channel head coil (40). The phantom is attached to a water-filled bottle and installed in the coil. They tried to define correlations between acquisition parameters and MD and FA, as well as the CV of

these DTIi. No correlations between NDGD and MD were reported, neither between NSA or voxel size and MD and FA; on the other hand, a negative correlation was found between MD and the SENSE factor, and a positive correlation between FA and SENSE or TE. The CV values of MD and FA were relatively high (7.1 % and 2.4 %) when compared to our results. This probably occurs because of the smaller size of their phantom, which turns it more susceptible to B_0 distortions and eddy-currents. Both the present work and previous studies (11, 27) point to macroscopic fiber configurations as a better alternative to DTI QC and long-term follow-up of diffusion protocols. Macroscopic fibers are less susceptible to geometric distortions due to B_0 inhomogeneities and eddy-currents, making it easier to know the characteristics of phantom' structures, besides what occurs with microscopic structures. However, the SNR and B_0 magnitude probably cause changes in DTIi.

Figures 4.22 and 4.23 show respectively the ellipsoids and tracts reconstructed using the ExploreDTI for 8-channel head coil when b = 500 s/mm^2 and b = 2500 s/mm^2. The ellipsoids or tracts of three bundles are seen in different slices because the bundles were not in the same plane intentionally, to simulate the curvature of human brain tracts. However, is possible to detect the anisotropic diffusion in the direction of bundles, which is highlighted when b = 2500 s/mm^2.
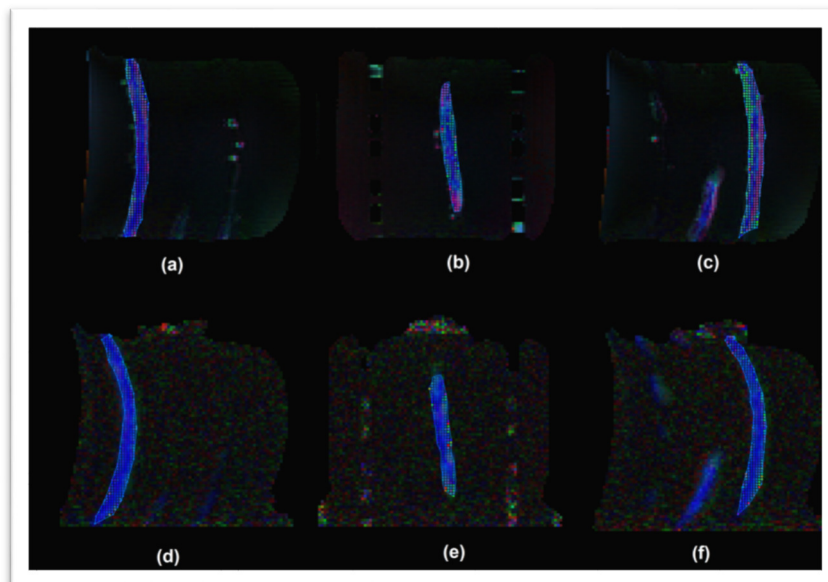
Figure 4.22 – Diffusion ellipsoids of DTI acquired changing b-values. (a), (b) and (c): diffusion ellipsoids of bundles 1, 2 and 3, respectively, for b = 500 s/mm^2. (d), (e) and (f): the ellipsoids of same bundles, for b = 2500 s/mm^2.
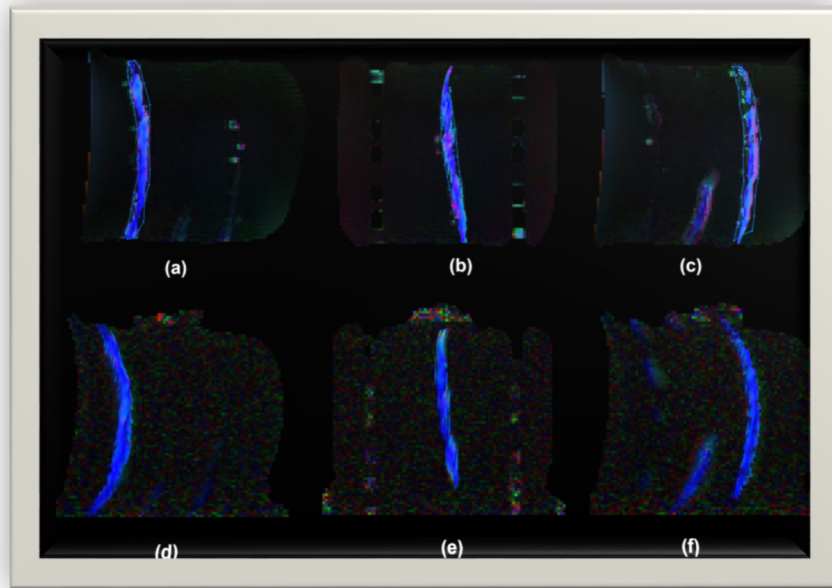
Figure 4.23 – Tracts reconstructed from DTI acquired changing b-values. (a), (b) and (c): tracts of bundles 1, 2 and 3, respectively, for b = 500 s/mm². (d), (e) and (f): the tracts of same bundles, for b = 2500 s/mm².

Figures 4.24-4.26 show the tracts reconstructions when some acquisition parameters are varied. Figure 4.24 shows the reconstructions for changes in b-value, for the 32-channel coil; Figure 4.25 shows reconstructions obtained changing TE and NSA, for both coils; and Figure 4.26 shows the fibers reconstructions when NDGD is changed, for the 8 and 32-channel coils.
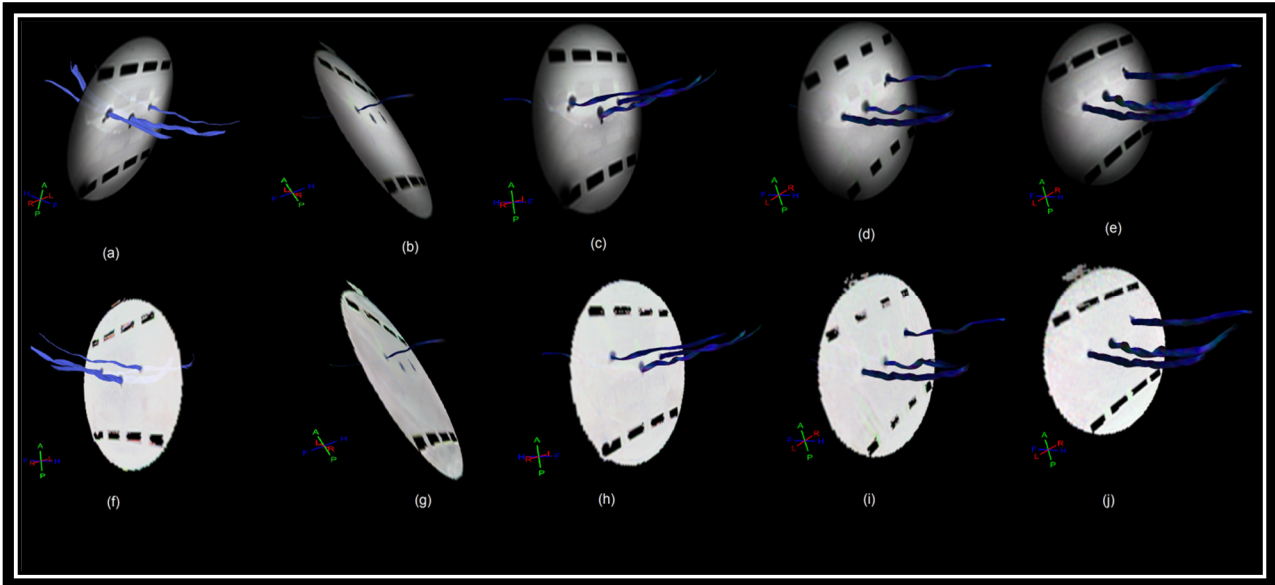
Figure 4.24 - Tracts reconstruction for acquisitions using the 32-channel coil, changing b-value. Top: tracts reconstructions co-registered with T2 images of phantom. Bottom: tracts' reconstructions co-registered with phantom ADC maps. (a) and (f) b = 800 s/mm^2; (b) and (g) b = 500 s/mm^2; (c) and (h) b = 1000 s/mm^2; (d) and (i) b = 1500 s/mm^2; (e) and (j) b = 2500 s/mm^2. The different inclinations of slices in (b) and (g) were applied to highlight the only fiber bundle reconstructed from the low b-value acquisition.

From Figure 4.24 it is possible to see that for b = 500 s/mm^2, two bundles (1 and 2) were not reconstructed, not identified from DTI data. Bundles 1 and 2 (composed by fibers with .25 and .35 mm) had lower water diffusion and consequently were not seen using a lower b-value (the images were less diffusion-weighted). For other b-values, all the bundles can be visualized, with a soft noise increase for b = 2500 s/mm^2.
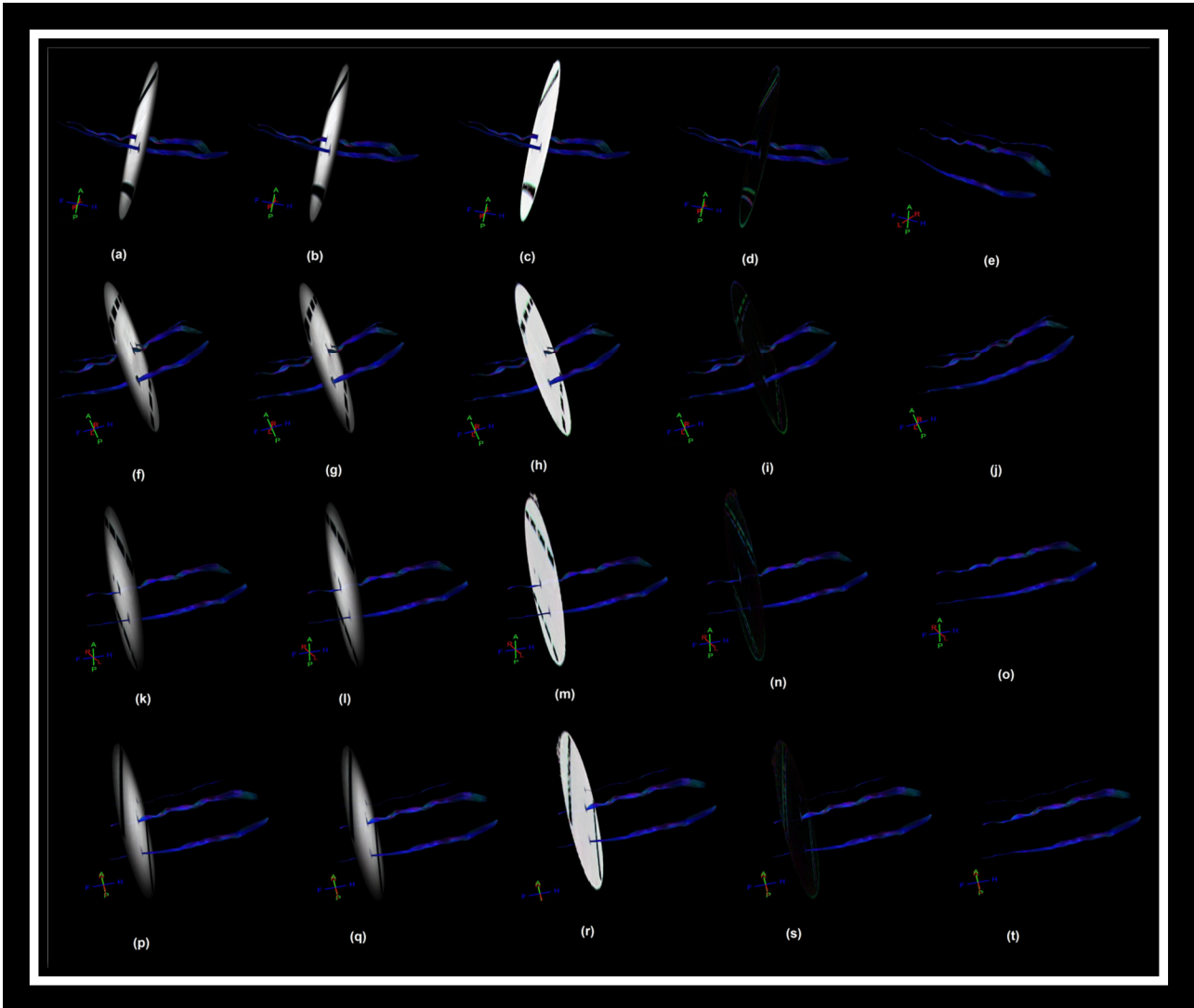
Figure 4.25 - Tracts reconstruction for acquisitions changing TE and NSA, for the 8 and 32-channel head coils. The tracts are co-registered with the T2, DW, ADC map and directional FA map images of the phantom, as well as shown stand alone, respectively, for all rows of this figure. First and second rows correspond to acquisitions changing TE and NSA, respectively, for the 8-channel coil; the following rows correspond to equivalent reconstructions for the 32-channel coil.

For both coils, changes in TE and NSA resulted in non-reconstruction of bundle 1, even though significant correlations had only been found between TE and CP for bundle 3 in the 8-channel head coil and between TE and MD, FA, VR and CP for the same bundle in the 32-channel coil (Figure 4.25). Furthermore, negative correlation is observed between TE and FA, for bundle 3 in the 32-channel coil and; for the 8-channel coil TE showed correlation with almost all DTIi, for all bundles applied. For the range of TE values tested, T2-weighting decreases when TE increases, which can reduce the diffusion-

weighting and consequently the water diffusion detection among the tracts. The increase of NSA may cause signal loss for low-contrast structures, which did not occur for the bundles analyzed.
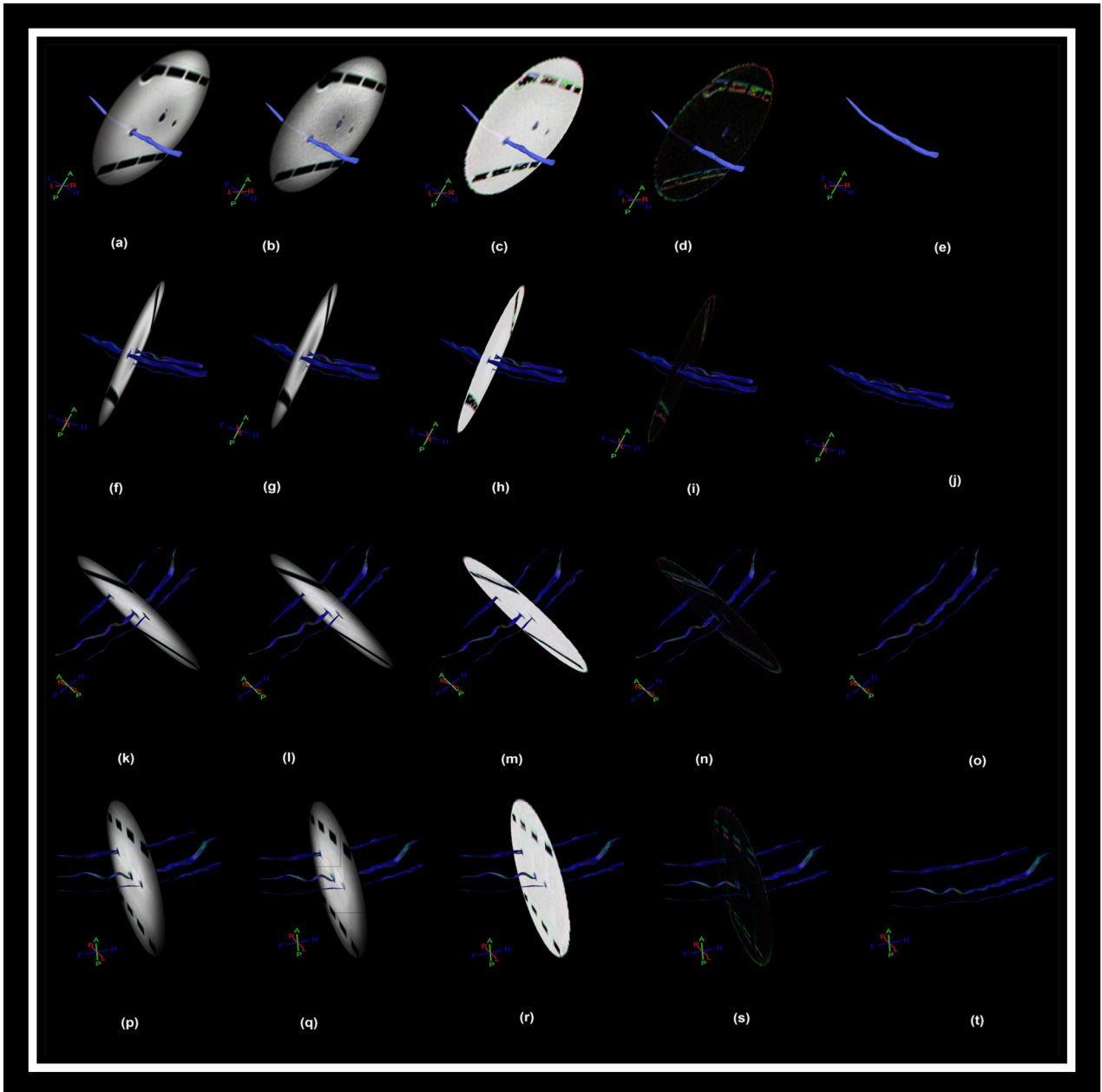
Figure 4.26 - Tracts reconstruction for acquisitions changing NDGD, for the 32 and 8-channel head coil. (a)-(e) tracts reconstructed co-registered with the T2, DW, ADC map and FA map images, as well as stand-alone tracts, respectively for acquisitions with NDGD = 6 using the 32-channel coil; (f)-(j), (k)-(o) and (p)-(t): the same for the 32-channel head coil with NDGD = 32, 8-channel coil with NDGD = 6, and 8-channel coil with NDGD = 32, respectively.

Figure 4.26 shows that for the 32-channel head-coil it was not possible to recon-struct all fiber bundles for NDGD = 6. In this case, bundle 3 (the thickest and made of fi-bers with highest diameter) was well defined, but the others were not found. On the other hand, for the 8-channel coil, all bundles were found for NDGD = 6 and 32.

In the phantom, the bundles were purposely not inserted at the same height, to simulate the tracts variety of shapes and orientations. So, just one or two bundles can be seen in the slice, but in most cases, all bundles can be seen, for all images acquired. Vis-ual changes in tracts are observed, for example, when b or the voxel size are changed. Increasing b, we observed a better visualization of tracts; the drawback is the increase of noise, both in the 8 and 32-channel head coil, as seen in Figure 4.24. Increasing the voxel size, we see a smoothing effect on tracts for both coils.

4.3 TESTING NEW MATERIALS

In this step, other materials than Dyneema® to build anisotropic diffusion phantoms were tested to verify if they are suitable to simulate fibers and tracts of human body. Figure 4.27 shows the images of the phantom described in Section 3.2, where conduits, catheters and fiber bundles of different materials were used.
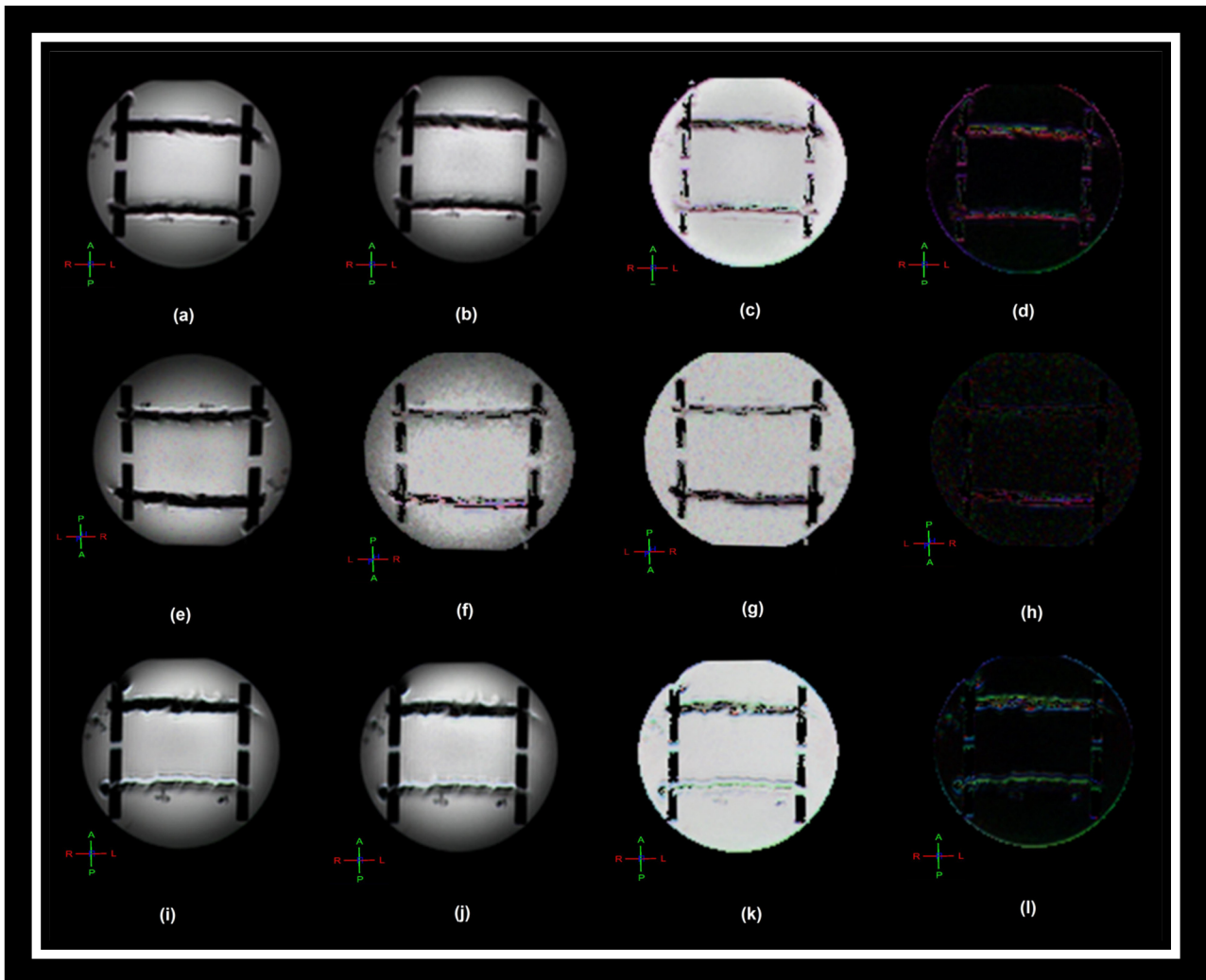
Figure 4.27 - T2, DW image, ADC map and FA map, respectively in each column, for the DTI phantom made with fishing lines, catheters and conduits. Images obtained for NDGD = 6 (a-d), 15 (e-h) and 32 (i-l).

The images of Figure 4.27 show that no tracts are found for this setup. Moreover, it was not possible to calculate any DTIi from these acquisitions. Catheters and conduits do not contribute with anisotropy and add noise to DT images, given that inside these structures there is macroscopic water motion (flux effects), such as occurs in the presence of thicker blood vessels, which can degrade DTI data. The phantom built was extremely noisy, full of structures without similarity to biological tissues in terms of constitution, TR, TE, diffusion and geometry. Catheters and conduits may be useful to compose MRI phantoms, including DWI and DTI phantoms, but in that case, just to simulate blood vessels and evaluate how these structures can change the DTIi of fiber bundles around them.

4.4 FIBER BUNDLES WITH HEAT-SHRINKING TUBES - CLINICAL PROTOCOL TESTS

In this step, the fiber bundles described in Section 3.3 were wrapped using heat-shrinking tubes to evaluate the stability of the setup for different clinical protocols, changing NDGD and b-value. Figure 4.28 shows the tracts reconstruction (co-registered with T1, DWI, ADC, PD, diffusion directionality map and stand-alone bundles for an acquisition with the 8-channel head coil), using b = 1000 s/mm^2 and NDGD = 32.
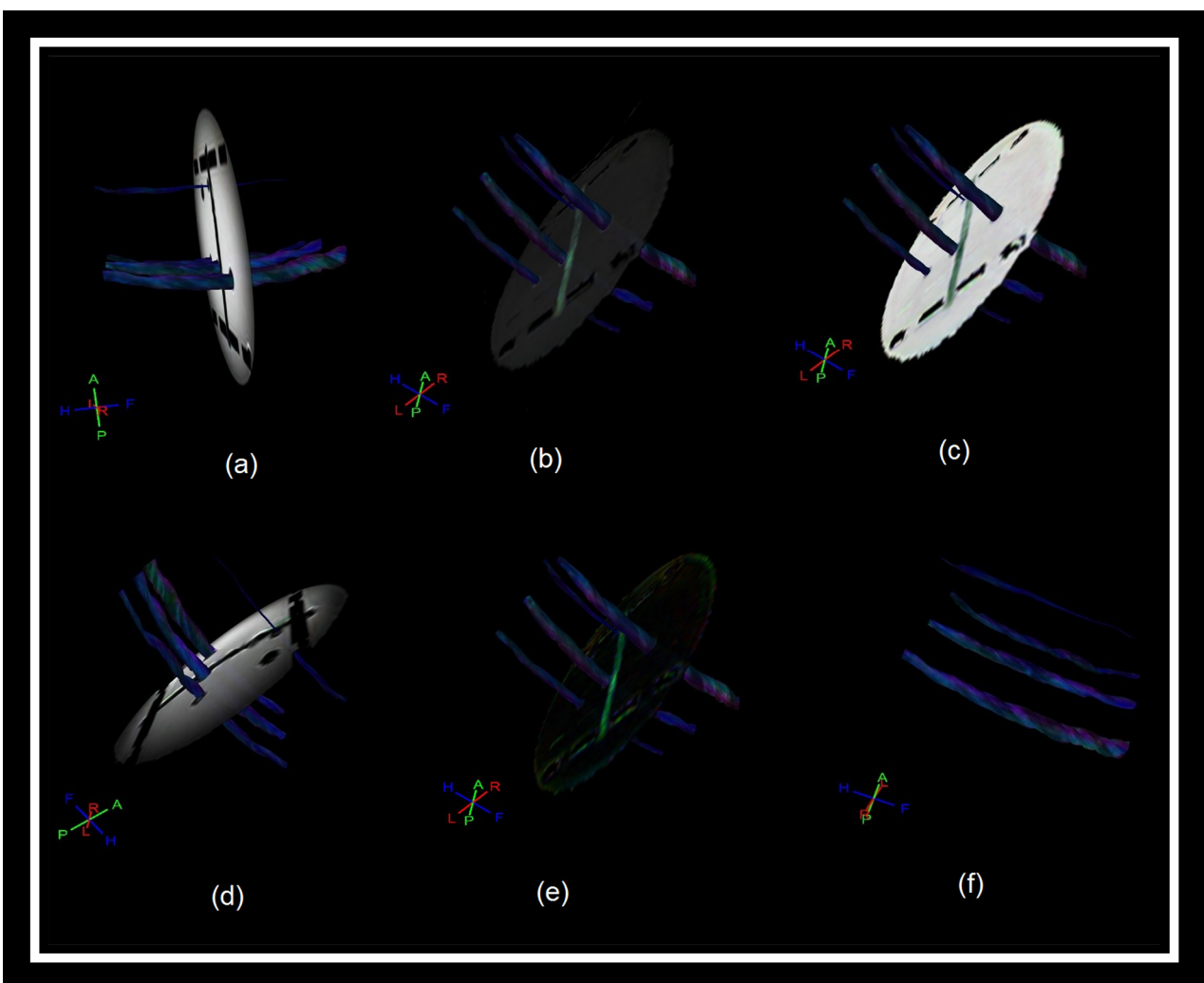
Figure 4.28 - Tracts reconstruction for acquisitions using the 8-channel coil, for fiber bundles wrapped with shrinking tubes. The tracts' images are co-registered with (a) T1, (b) DW, (c) ADC map, (d) PD and (e) directional FA color-coded images. (f) Standalone tracts.

Figure 4.28 shows the tracts with good definition, which is due to the higher FA of fibers when the heat-shrinking tubes were applied. Here, the FA values found are in the range (0.6-0.8), being similar to those found for the main brain tracts. Moreover, shrinking tubes do not introduce any kind of artifacts in the images. So, Dyneema® fiber bundles wrapped with heat-shrinking tubes are a good alternative to simulate high anisotropy body tissue tracts.

Figures 4.29-4.32 show the mean values of DTIi and corresponding CV values, for all six fiber bundles described in Table 3.3. These data were obtained changing NDGD of the DTI protocol and using the clinical protocols for precocious epilepsy and primary brain tumor, implemented in the clinical routine of the tested scanner. The only difference between these clinical protocols was the slice thickness (1 mm for epilepsy and 2 mm for tumor). Figures 4.33 and 4.34 show the corresponding tracts reconstructions.
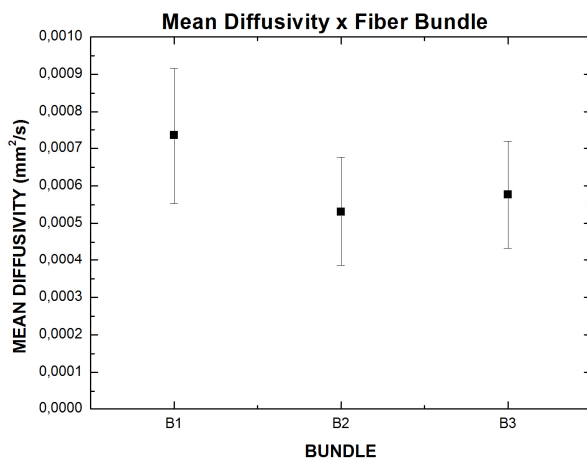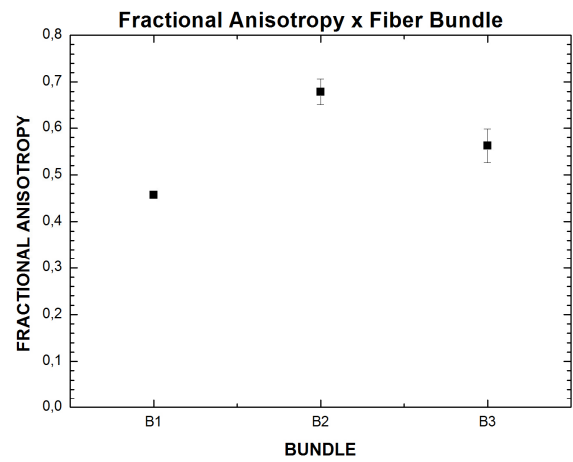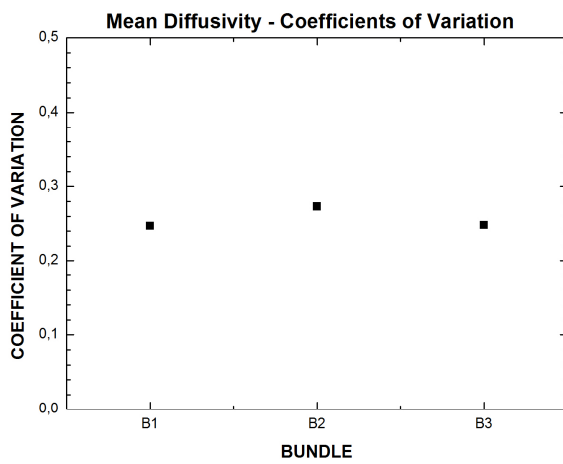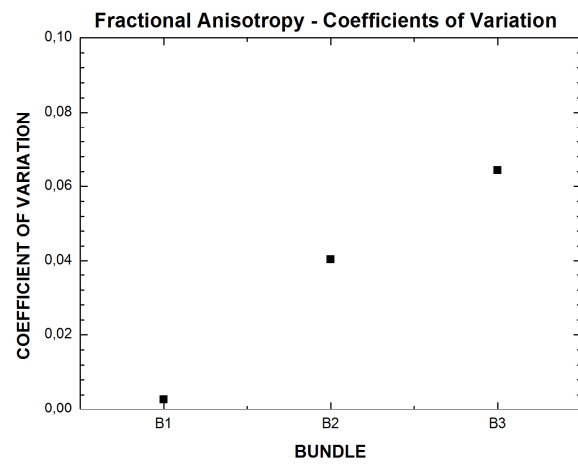
Figure 4.29 - Graphs of DTIi (MD and FA) and their corresponding CV for DTI acquisitions using different protocols. (a) and (b): mean values found for MD and FA, respectively. (c) and (d): CV values for these DTIi.
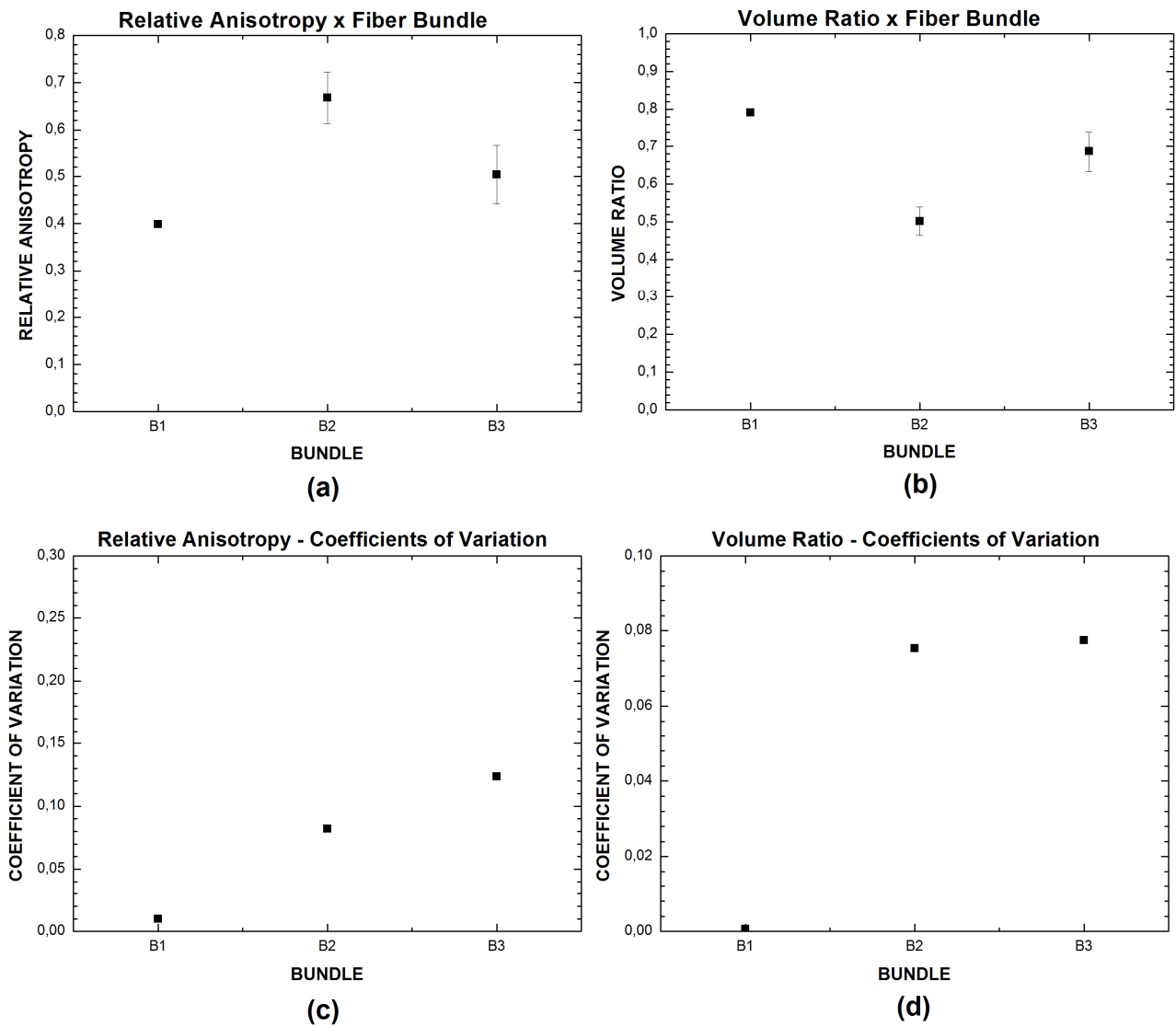
Figure 4.30 - Graphs of DTIi (RA and VR) and their corresponding CV for DTI acquisitions using different protocols. (a) and (b): mean values found for RA and VR, respectively. (c) and (d): CV values for these DTIi.
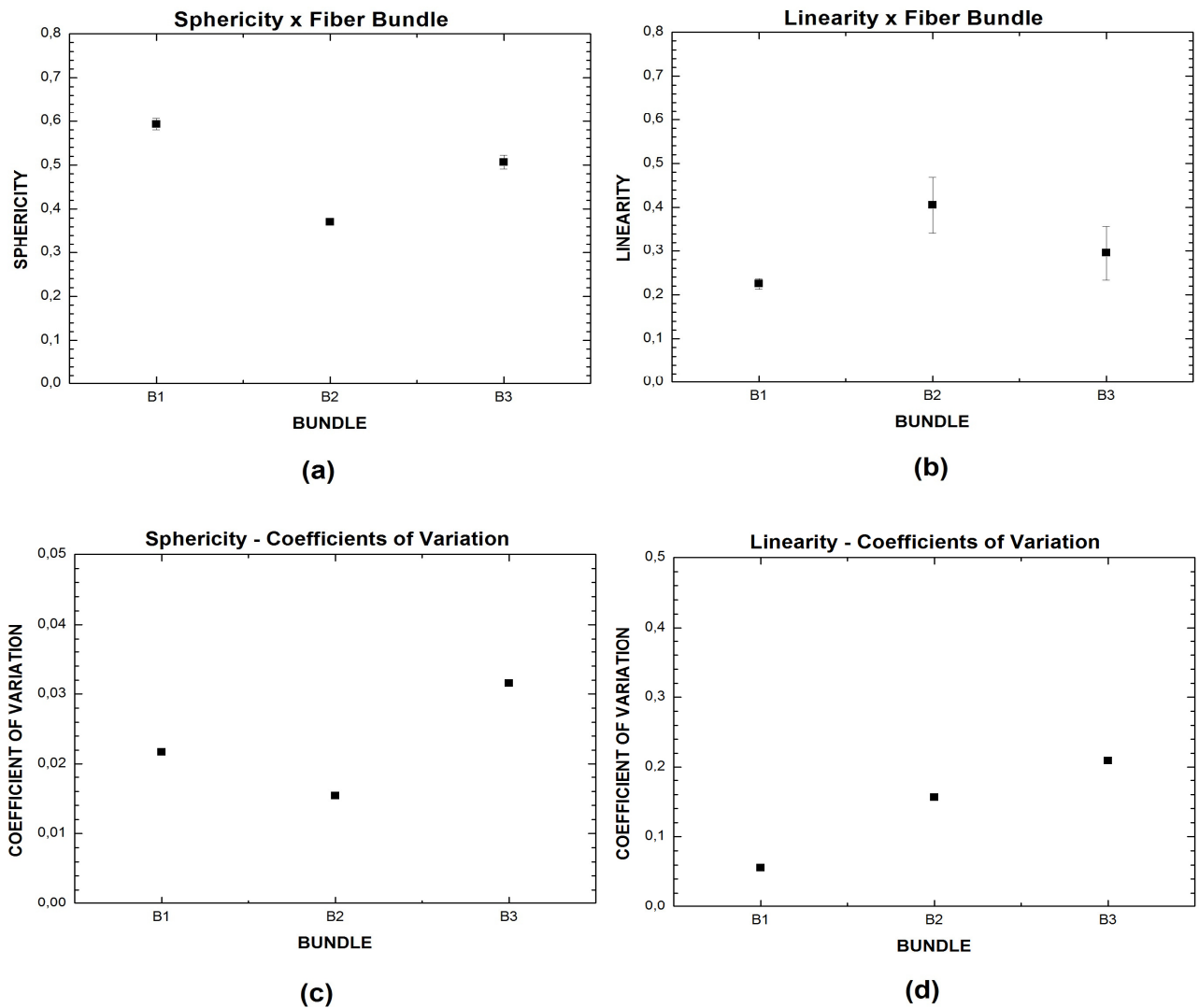
Figure 4.31 - Graphs of DTIi (CS and CL) and their corresponding CV for DTI acquisitions using different protocols. (a) and (b): mean values found for CS and CL, respectively. (c) and (d): CV values for these DTIi.

(a)

(b)
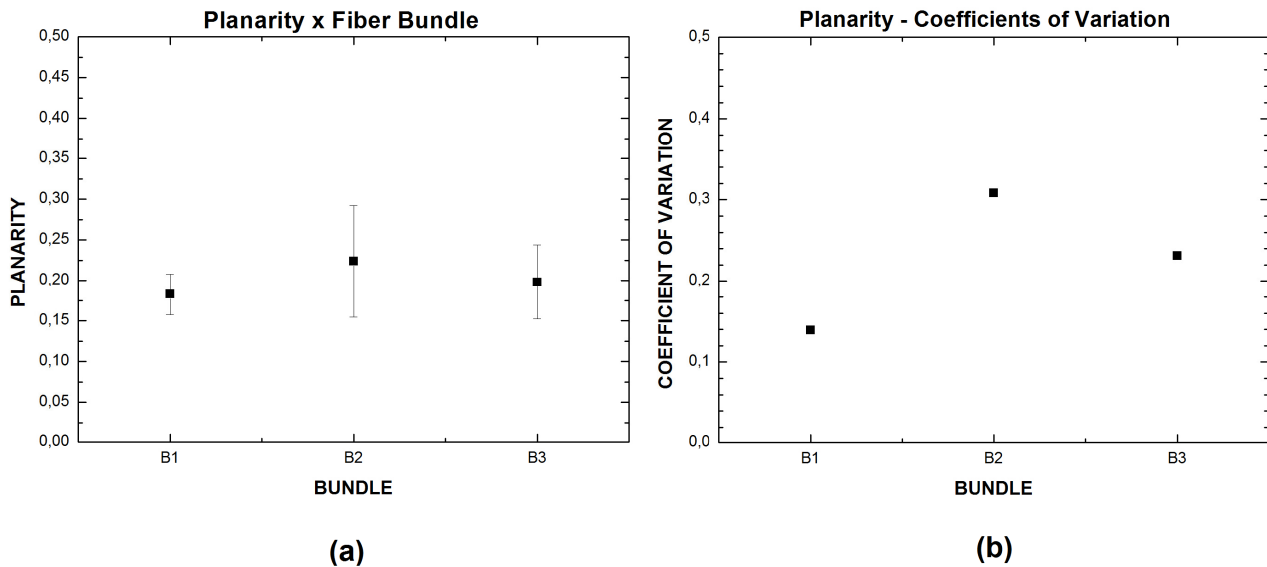
Figure 4.32 - Graphs of DTIi (CP) and their corresponding CV for DTI acquisitions using different protocols. (a) and (b): mean and CV values found for CP.

Considering the setup used for protocol comparisons, heat-shrinking tubes, when applied to fiber bundles, improved significantly the bundles' anisotropy. For example, a Dyneema® bundle when wrapped with these tubes shows FA of (0.72 ± 0.04) and a lower CV value, as seen in Figure 4.29(b) and 4.29(d), respectively. Without heat-shrinking tubes, the best FA value found was (0.42 ± 0.02). The FA value of this bundle when compressed using the tube is similar to those found for corpus callosum in the brain. The tracts definition in Figures 4.33 and 4.34 supports the use of this tubes in DTI phantom designs.

From the graphs in Figure 4.29, it is possible to see that bundle 3 (made of Dyneema® fishing line with 0.40 mm thickness) shows the highest mean FA value, considering the five protocols tested. Bundles 4 and 5, also made of the same material, have respectively the second and third highest mean FA values. Although bundle 1 was also made of multifilament fishing lines (Spectra®), these lines have memory, which makes it difficult building bundles with high anisotropy. The FA value found for the Spectra® bundle is only 3% lower than the one for bundle 5 (made of Dyneema® fishing lines of 0.25 mm thickness). However, the diffusion signal from Dyneema® bundles is higher than from other materials. Although bundle 6 was also made of Dyneema® with 0.40 mm thickness (having the same structure as bundle 3), its mean FA value was the lowest. Probably this is because this bundle was a crossing bundle. This condition is not well solved by the most common DTI algorithms, for which Q-Ball, HARDI or DSI, for example, could be more effective.

Despite the fact that polyamide fibers had already been studied as a raw material for DTI phantoms (27, 38), revealing that this material was not useful for building fiber phantoms, we decided to test the performance of polyamide fishing lines using heat-shrinking tubes to control their memory effects and increase the anisotropy. We found that both memory and composition make it difficult building anisotropic structures with these fishing lines. The mean FA value found was approximately the same of the crossing bundle.

Bundles 3 and 4, which show higher anisotropy, have the lowest CV values for MD, FA, RA and CL (Figures 4.29-4,31; for bundle 6, the highest CV values were found for these DTIi. The mean value of CP does not differ significantly among different bundles (Figure 4.32).
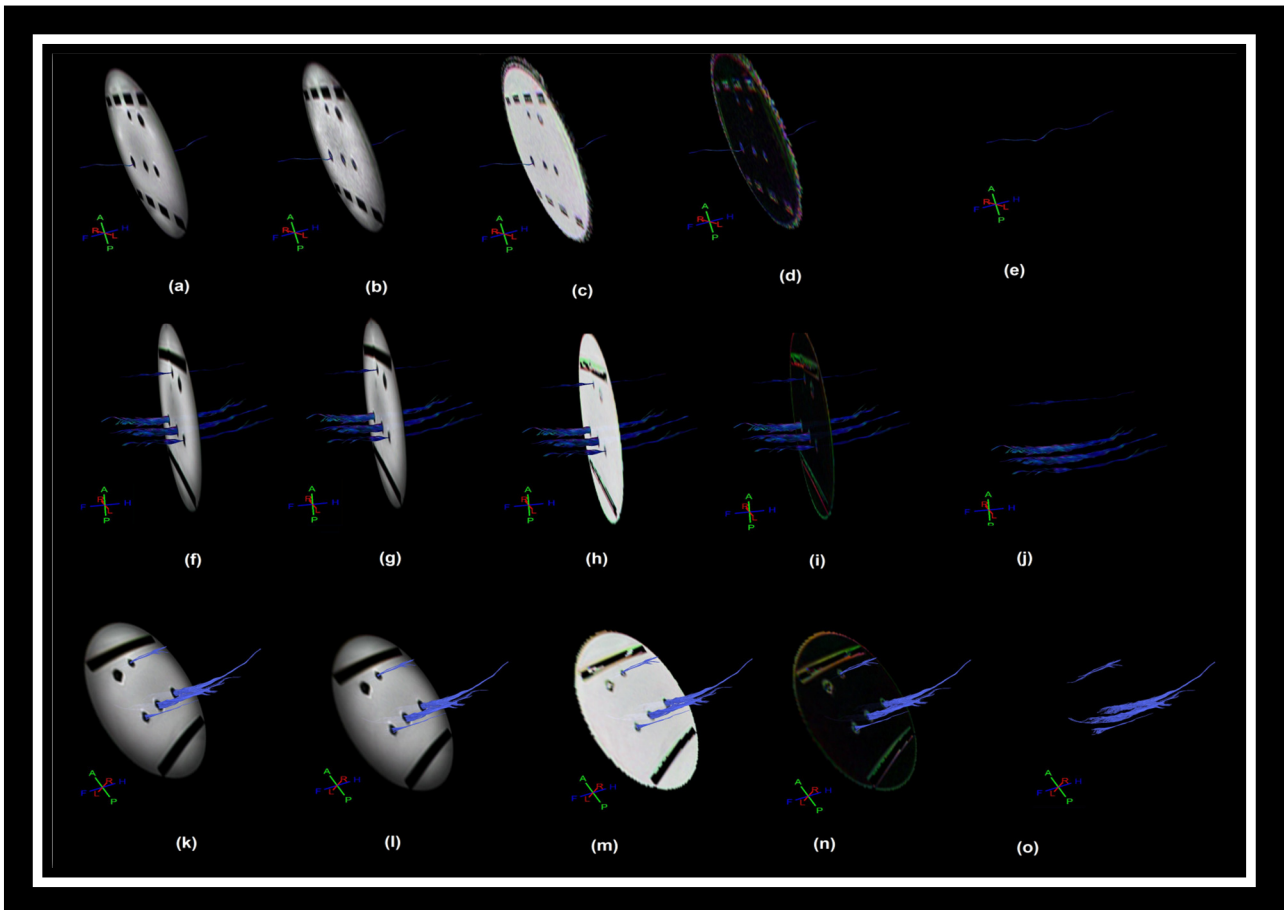
Figure 4.33 - Tracts reconstructed from DTI acquired changing NDGD, for the 8-channel head coil. The tracts are shown co-registered with the T2 image, DW image, ADC map, FA color-coded map, as well as shown stand alone, respectively. Top: NDGD = 6; Middle: NDGD = 15; Bottom: NDGD = 32.

In Figures 4.33 and 4.34 is possible to see that only the Dyneema® fiber bundle was reconstructed for most acquisitions. The Spectra® fiber bundle is seen in acquisitions using test protocols with NDGD of 15 and 32. These protocols can be adapted to clinical routine, with the aim of trying to improve the WM fibers detection. In both clinical protocols, the three Dyneema® bundles are seen.
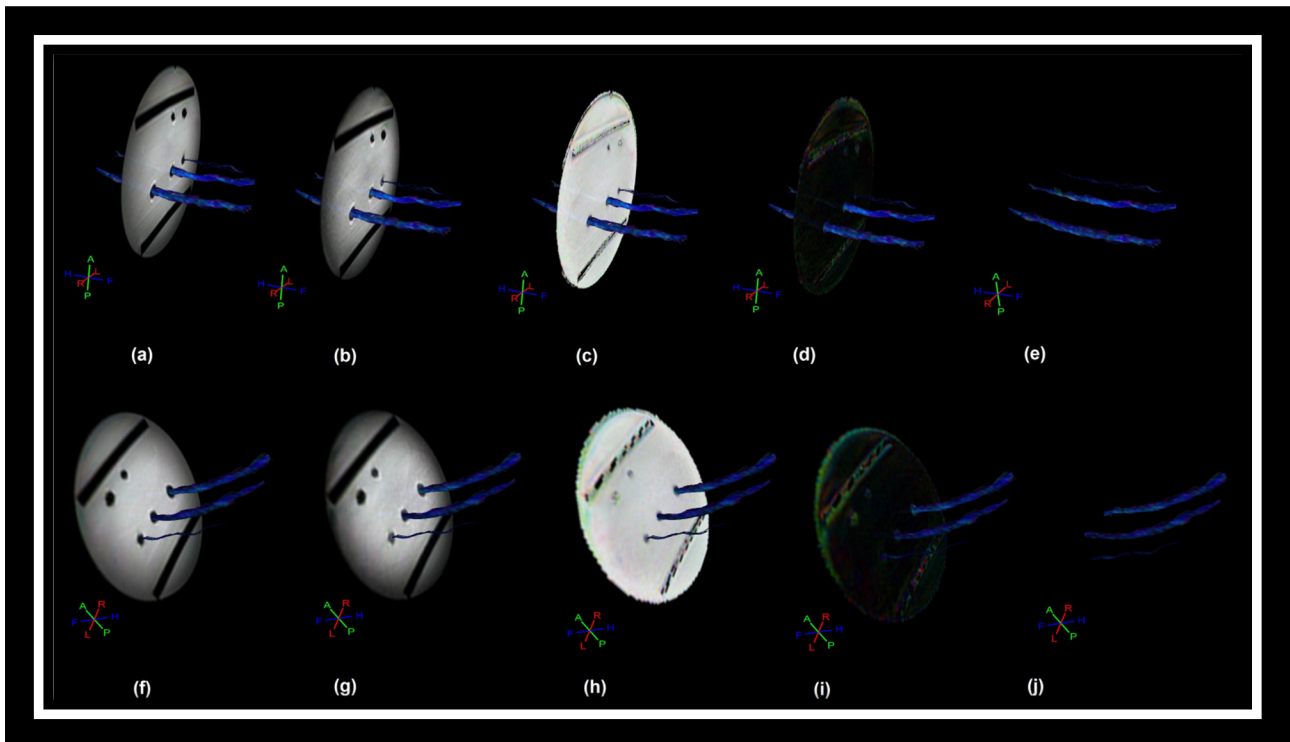
Figure 4.34 - Tracts reconstructed from DTI acquired using protocols for precocious epilepsy (top) and primary brain tumors (bottom), for the 8-channel head coil. The tracts are shown co-registered with the T2 image, DW image, ADC map, FA color-coded map, as well as shown stand alone, respectively.

From the results obtained in this section and until now, it was found that Dyneema® fishing lines of 0.40 mm are the best option to build DTI phantoms. Their bundles are stable even when DTI acquisition parameters change. The heat-shrinking tubes are essential to ensure high anisotropy values. So, phantoms based on these bundles are useful for applications such as cross-calibration of DTIi, considering different protocols, or even different scanners, from different vendors, many B_0 values and different coils.

4.5 MULTIPURPOSE PHANTOM ASSAYS

Figure 4.35 shows the T1 images of the multipurpose phantom developed. With this phantom, it was possible to check scanner performance parameters, by means of specific modules to evaluate spatial resolution, slice thickness, geometric distortions and even SNR, which can be estimated using the homogeneous portion of the phantom. The following sections describe the results obtained from the QC measurements using the device in a 3T MRI scanner. The phantom study was done using the setup and the protocols described in Section 3.4. This section also describes the details of the phantom preparation.

Figure 4.35 shows T1 coronal and axial images of the multipurpose phantom, used to estimate other scanner performance parameters than DTI.
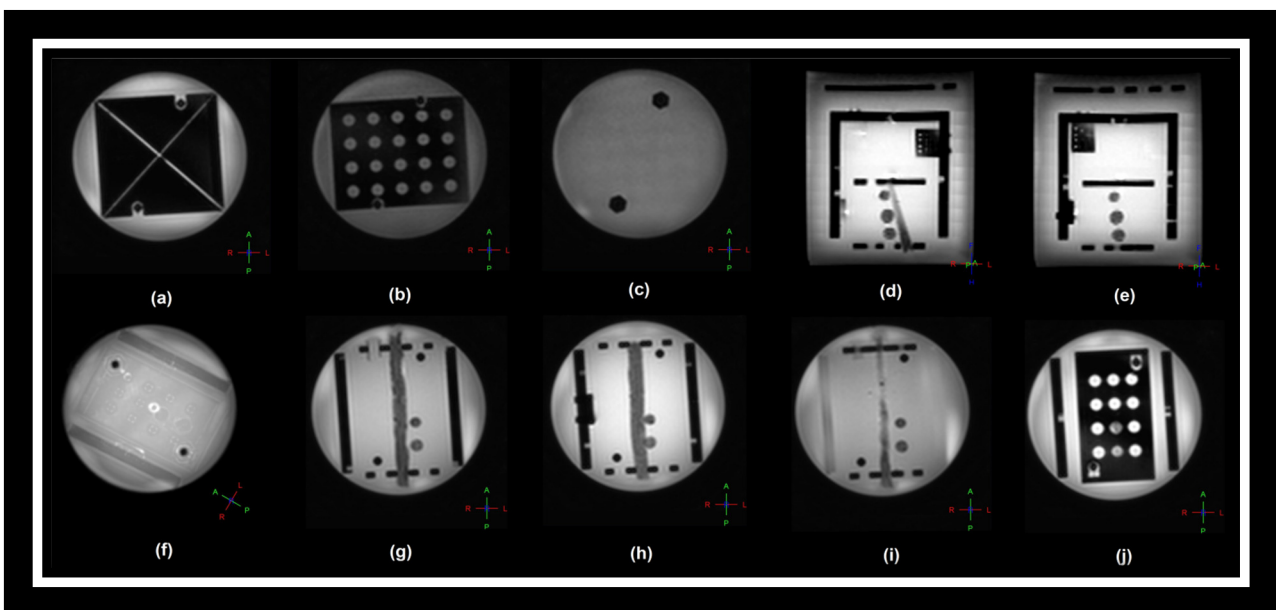
Figure 4.35 - T1 images of the multipurpose phantom. In the images, it is possible seeing the ramps to calculate slice thickness (a), the grid pattern for evaluation of geometric distortions (b), the background to determine SNR (c) and the blocks to evaluate spatial resolution (d) and (e). The fiber bundles can be seen in (g), (h) and (i) (longitudinally) and also in (d) and (e) (axially). The block where the fibers are fixed (j) can also be used to detect geometric distortions patterns. (f) shows a section from a 3D rendering of the phantom.

Figure 4.35 shows that the T1 image of the phantom does not have significant artifacts that could compromise the identification of the structures of each module. There are

some regions of non-homogeneity in the background, which may be balanced using shimming methods and even $CuSO_4$-based solutions that improve SNR. Before any kind of quantification, a visual inspection was done.

In all experiments, it was chosen to fill the phantom with just distilled water, given that water diffusion is the subject of study in DW and DT images. However, conventional MRI phantom filling solutions, such as $CuSO_4$, can improve the SNR and consequently the characterization of other MRI parameters tested with the multipurpose phantom. This kind of assay will be done in the future. The acceptability of the parameters measured was based on patterns of other phantoms, such as the ACR (68) and the AAPM (American Association of Physicists in Medicine) (69), even though the structures present in our multipurpose phantom differ in size and shape from theirs.

4.5.1 Slice Thickness

Figure 4.36 shows the T1 image of the module for evaluation of slice thickness and the profiles obtained for estimation of this parameter.
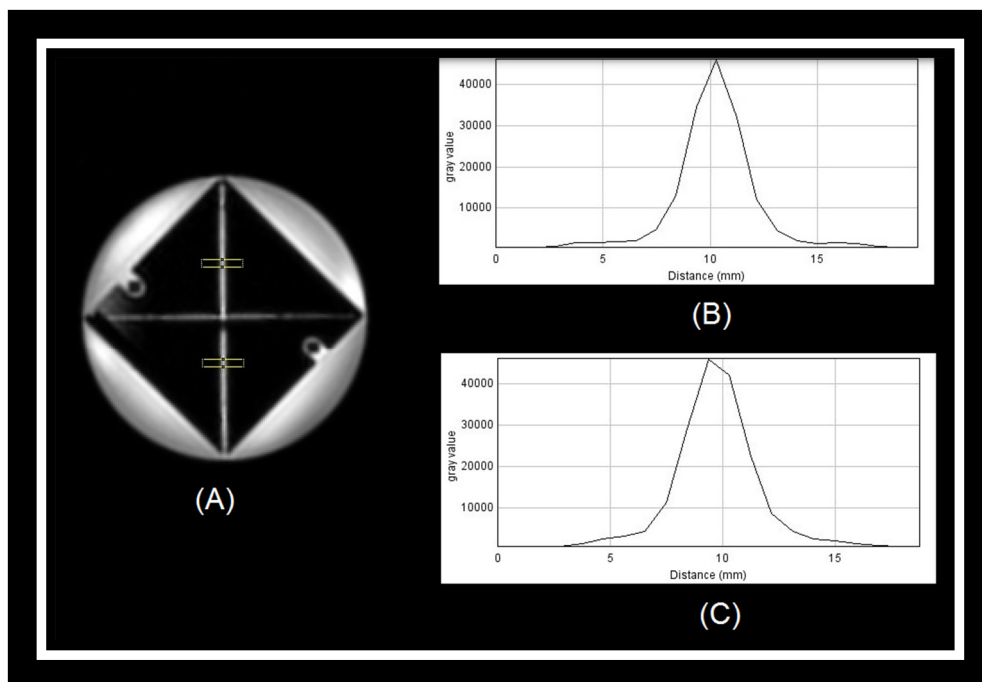
Figure 4.36 - T1 image of the square plate for slice thickness measurement and profiles to estimate this parameter. (a) T1 image showing the ROIs (in yellow) for estima-

tion of profiles. (b) and (c) Profiles found for the ROIs at the top and at the bottom of the image, for the ramps' gap of 2 mm.

The slice thickness was measured from the FWHM of gaps' profiles. The mean and standard deviation of FWHM in both ROIs were taken. From the ROIs in the image of Figure 4.31(a), we obtained a slice thickness of (2.005 ± 0.1768) mm, differing approximately by 0.5% from the real value of the slice thickness used in the acquisition (2 mm). According to literature (68, 70), differences up to 0.7 mm are acceptable, therefore our result is very good. Acquisitions using 1 mm slices were not performed due to time issues. This will be done in future assays.

4.5.2 Signal-to-Noise Ratio

Figure 4.37 shows portions of the multipurpose phantom where few structures are seen. Basically, it is possible to see laterally the ramps for slice thickness measurement and the polyacetal fuses, which did not generate any kind of imaging artifacts, even in images without SENSE. The SNR was measured using the ROIs showed in the center of the phantom (4.37(a)) and outside the phantom (4.37(b)).
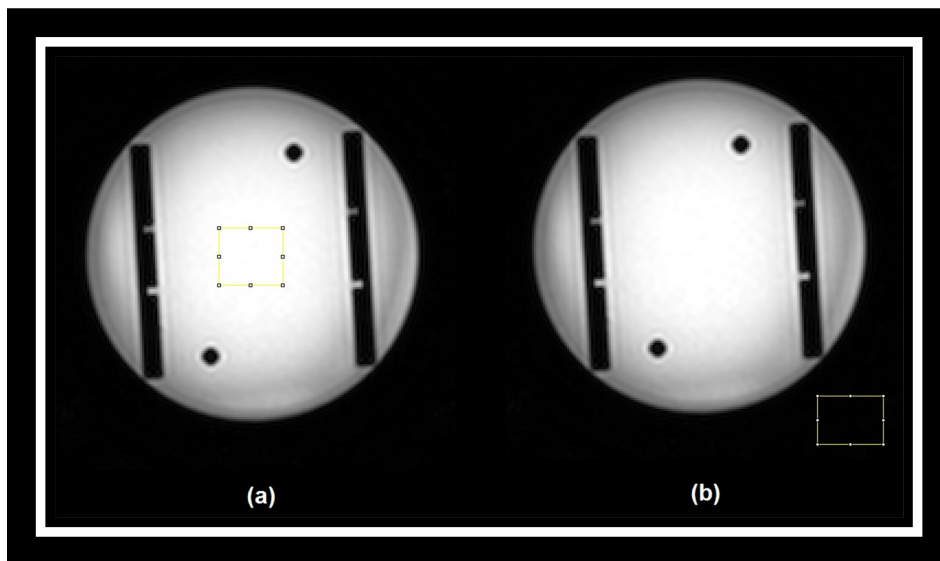
Figure 4.37 - Measuring the SNR using T1 images. T1 image slice showing the ROIs in the center of the phantom (a) and in the background (b) to estimate the SNR.

From the image and ROIs showed in Figure 4.37, we found a SNR of 217, for a signal of 1350 (mean intensity in the center ROI) and a background standard deviation of 4, which is acceptable according to the reference SNR found in literature (52), which should be in the range (130-270).

This image slice would be also useful to estimate the integral uniformity of the image. This will be included in future phantom applications. If the homogeneity of the image is not considered to be good, then the SNR may be derived more accurately using the NEMA method, where two consecutive images are acquired and this parameter is calculated based on subtraction of these images.

4.5.3 Geometric Distortions

Figures 4.38(a) and (b) show coronal views of the block from the DTI module, whose hole pattern can be useful to evaluate geometric distortions. Figure 4.38(c) shows the geometric distortion module (a plate with a hole pattern).
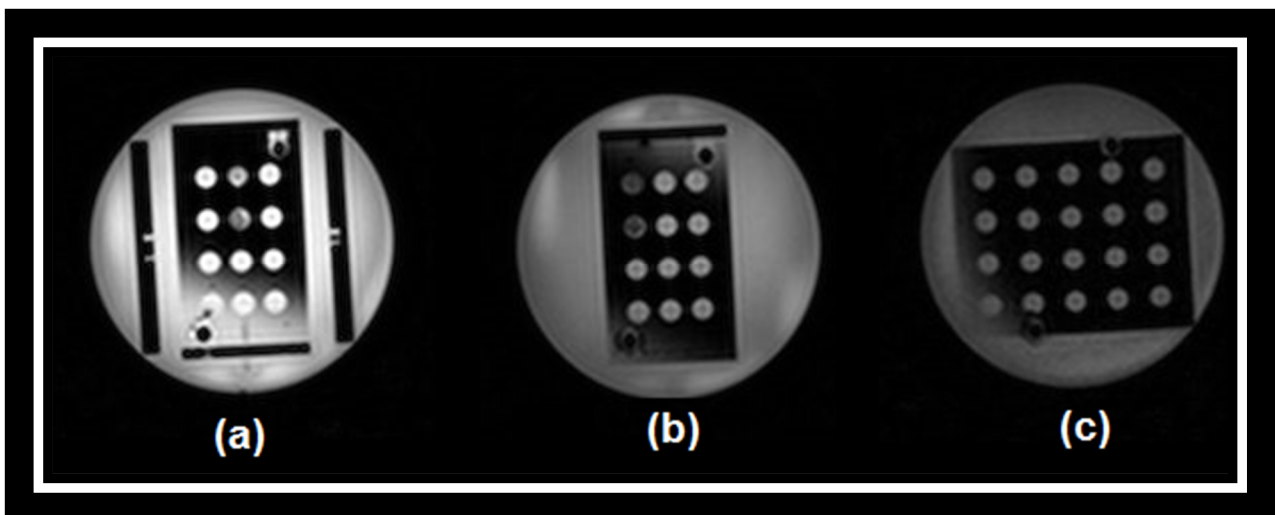
Figure 4.38 - Images for evaluation of geometric distortions. (a) and (b) Hole pattern from the DTI module and (c) from the hole pattern plate of the multipurpose phantom.

It was found that both the hole pattern plate and the block where the fiber bundles are fixed contribute to evaluate this image characteristic. The image of hole patterns showed a soft intensity difference in one of its edges due to position of its structures in the head coil (it was near the edge of the coil), which can be improved by changing its position

in the spindle. The spindles also allow the use of full setup or just one or more modules for MRI QC. Even when acquiring just DT data, the block for fiber bundles is useful to detect geometric distortions due to eddy-currents, for example, which can degrade the results.

4.5.4 Spatial Resolution

Figure 4.39 shows coronal views of the phantom, where it is possible to see the small blocks for spatial resolution estimation, according to the smallest pattern of holes visually distinguished. In both slices, two of three blocks are visualized. Another one is seen in sagittal slices. A module for checking the low-contrast detection performance can also be implemented in the future.
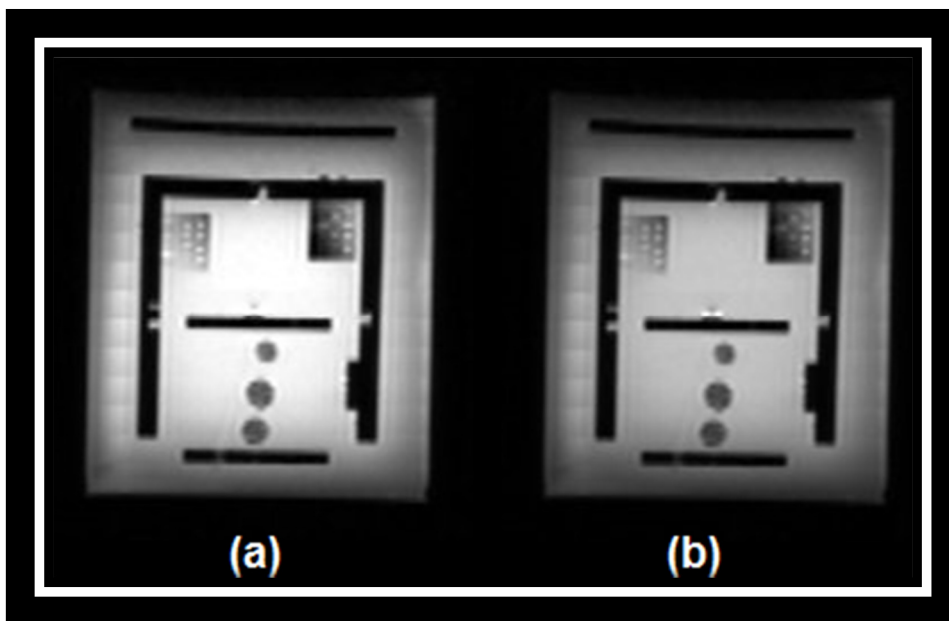
Figure 4.39 - T1 coronal images of the multipurpose phantom. In (a) and (b) it is possible to see two of three blocks for estimation of spatial resolution.

4.5.5 DTI Quality Control

The efficiency of the DTI module for QC of this imaging technique was evaluated by analysis of the DTIi obtained for the setup of Figure 3.10(b), for the 8-channel coil, changing the b-value. Figures 4.35 and 4.36 show the graphs of mean and CV values for each DTIi estimated in this study, for the fiber bundles described in Table 3.4.

(a)

(b)

(c)

(d)
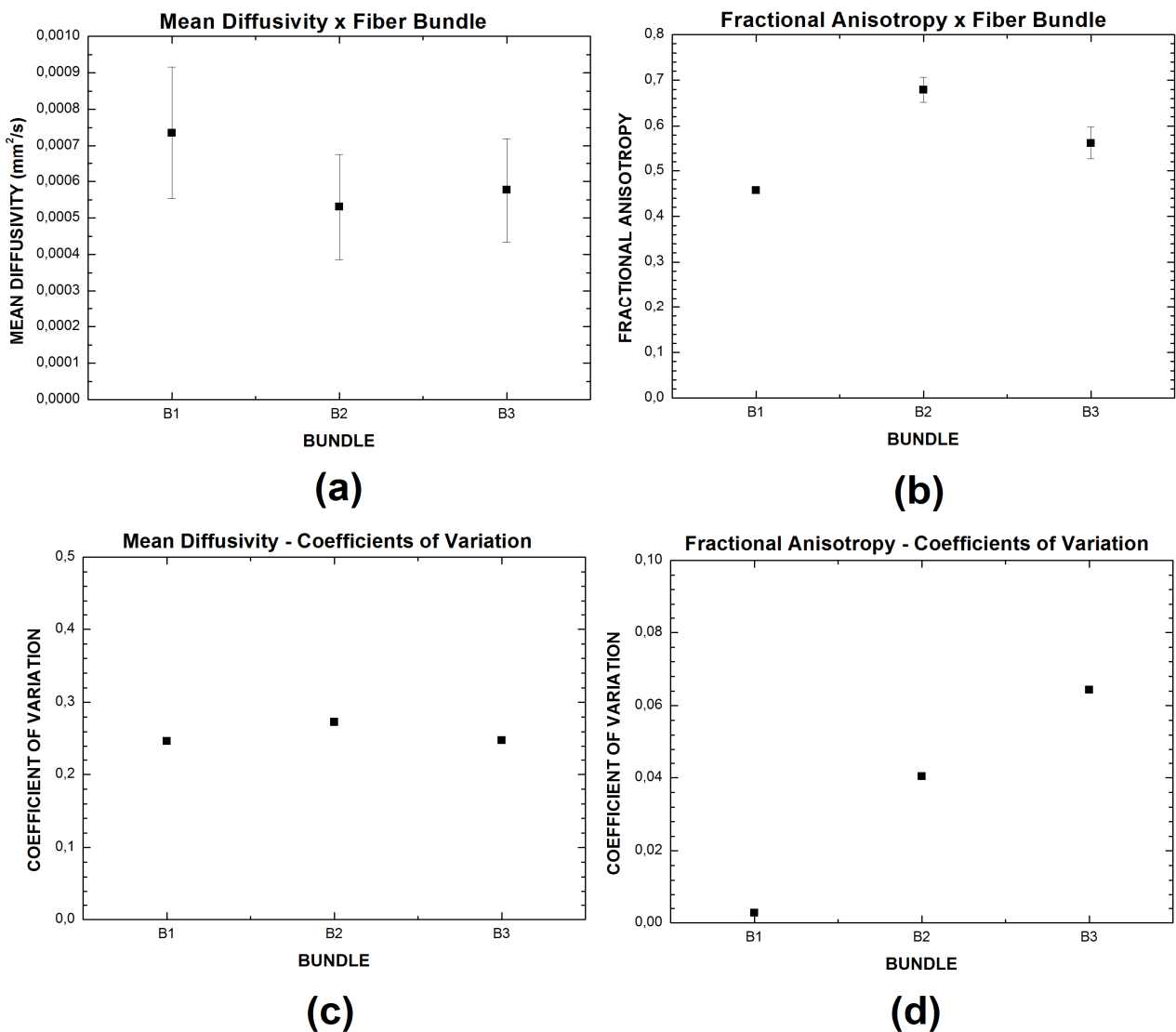
Figure 4.40 - Graphs of DTIi (MD and FA) and their corresponding CV for DTI acquisitions using the multipurpose DTI phantom. b = 1000 s/mm^2 and b = 2500 s/mm^2. (a) and (b): mean values for MD and FA, respectively. (c) and (d): CV values for these DTIi.
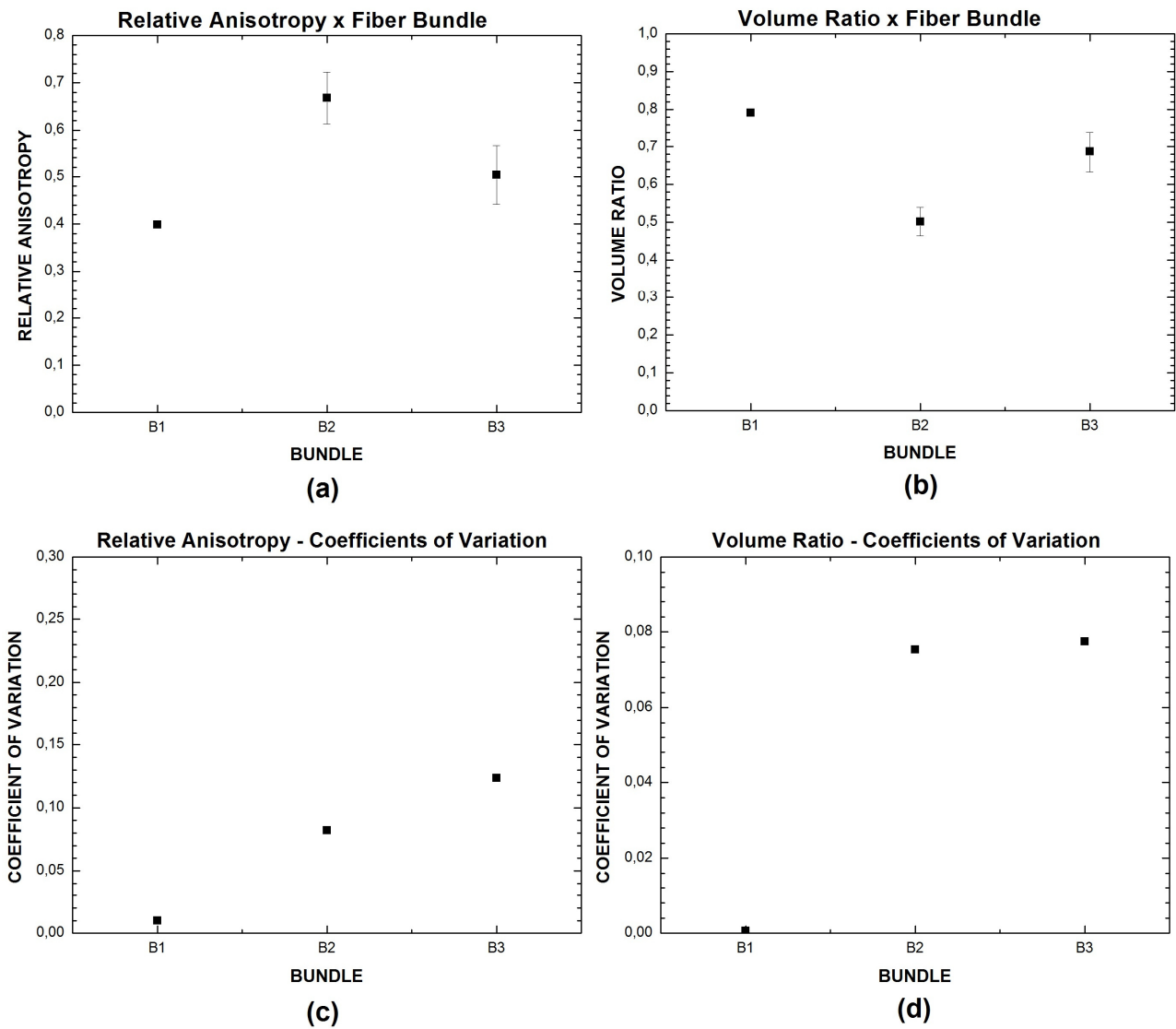
Figure 4.41 - Graphs of DTIi (RA and VR) and their corresponding CV for DTI acquisitions using the multipurpose DTI phantom. b = 1000 s/mm² and b = 2500 s/mm². (a) and (b): mean values for RA and VR, respectively. (c) and (d): CV values for these DTIi.
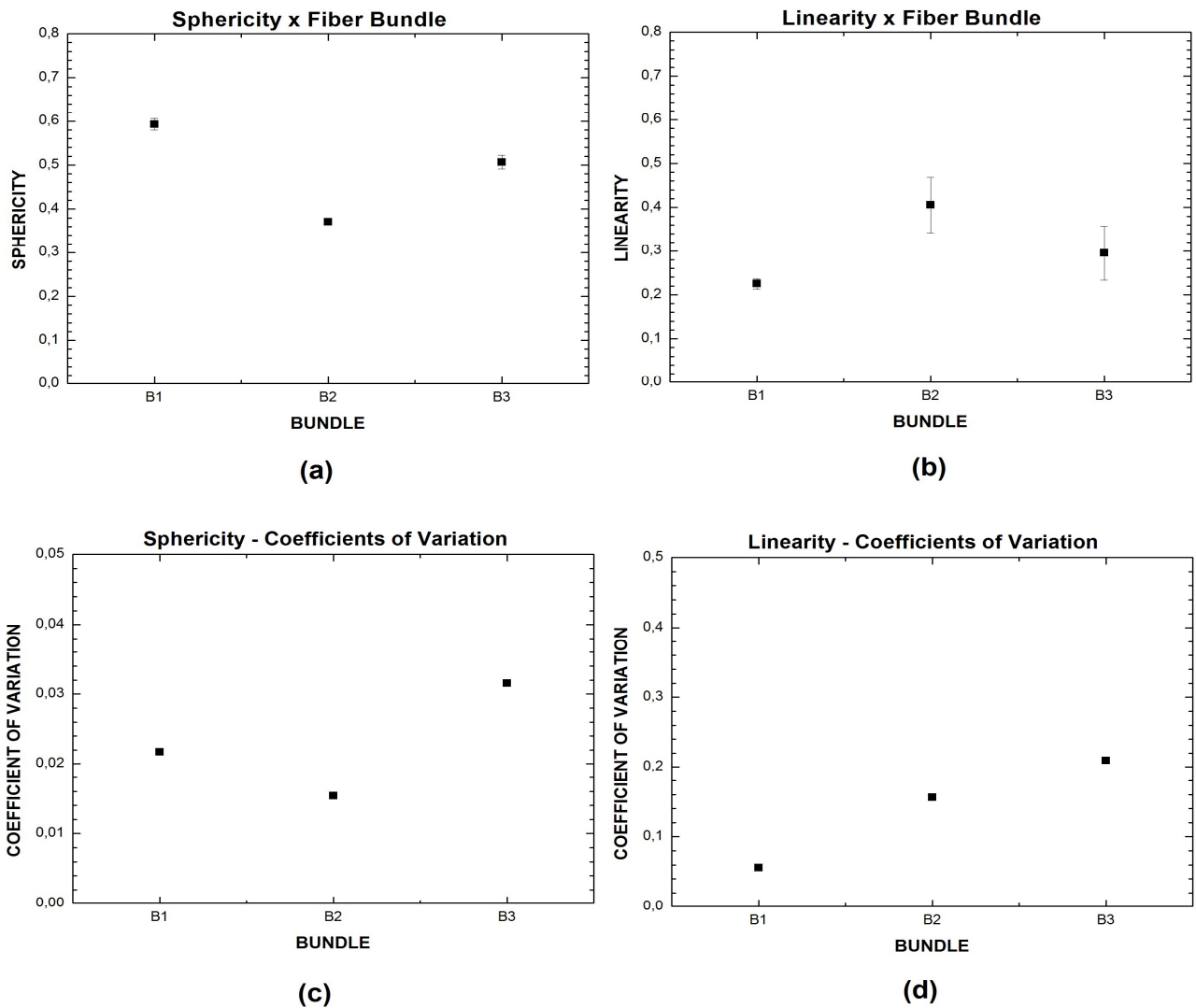
Figure 4.42 - Graphs of DTIi (CS and CL) and their corresponding CV for DTI acquisitions using the multipurpose DTI phantom. b = 1000 s/mm² and b = 2500 s/mm². (a) and (b): mean values for CS and CL, respectively. (c) and (d): CV values for these DTIi.
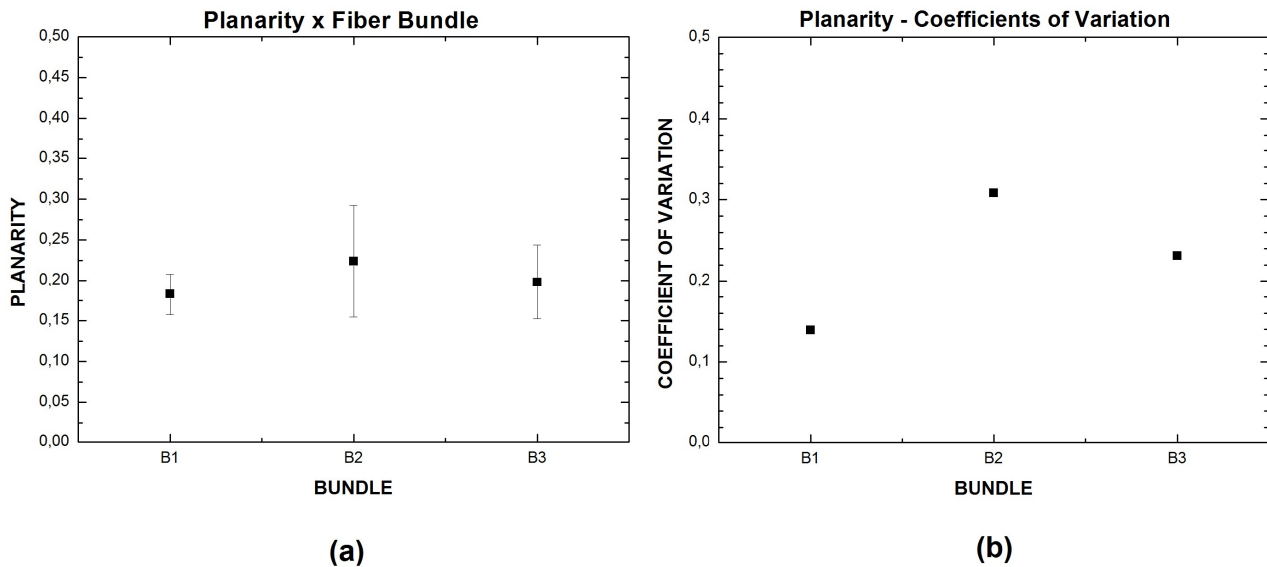
Figure 4.43 - Graphs of DTIi (CP) and their corresponding CV for DTI acquisitions using the multipurpose DTI phantom. b = 1000 s/mm^2 and b = 2500 s/mm^2. (a) and (b): mean and CV values of CP, respectively

The graphs of Figures 4.40-4.43 reveal the same behavior of DTIi seen in Section 4.2. The change of bundle length does not interfere in the DTIi calculated. Bundle 2 showed again higher FA values, which are similar to those found in Figure 4.29. The fibers applied here are the same of Section 4.2 differing from those just by the length (these ones are shorter than those of Section 4.2).

The CV values for all DTIi were smaller for all bundles, pointing to long-term stability of structures, as well as to the applicability of them for cross-calibration studies, protocol design and improvement and routine QC of DTI.

The Spectra® fishing line bundle showed the lowest FA values, having also lower RA and higher MD than other bundles. Even though Dyneema® fibers had already shown the best FA values and SNR for DTI QC, Spectra® was tested again because theses fibers seem useful to build bundles simulating cardiac fibers (MD and FA values are, up to now, the most similar to those found for these muscle fibers) (7, 13, 71). Both kind of fishing lines are composed by the same material, but the manufactures' techniques are different. It can lead to differences in diffusion proprieties of similar fiber bundles composed by one or other kind of fishing line.
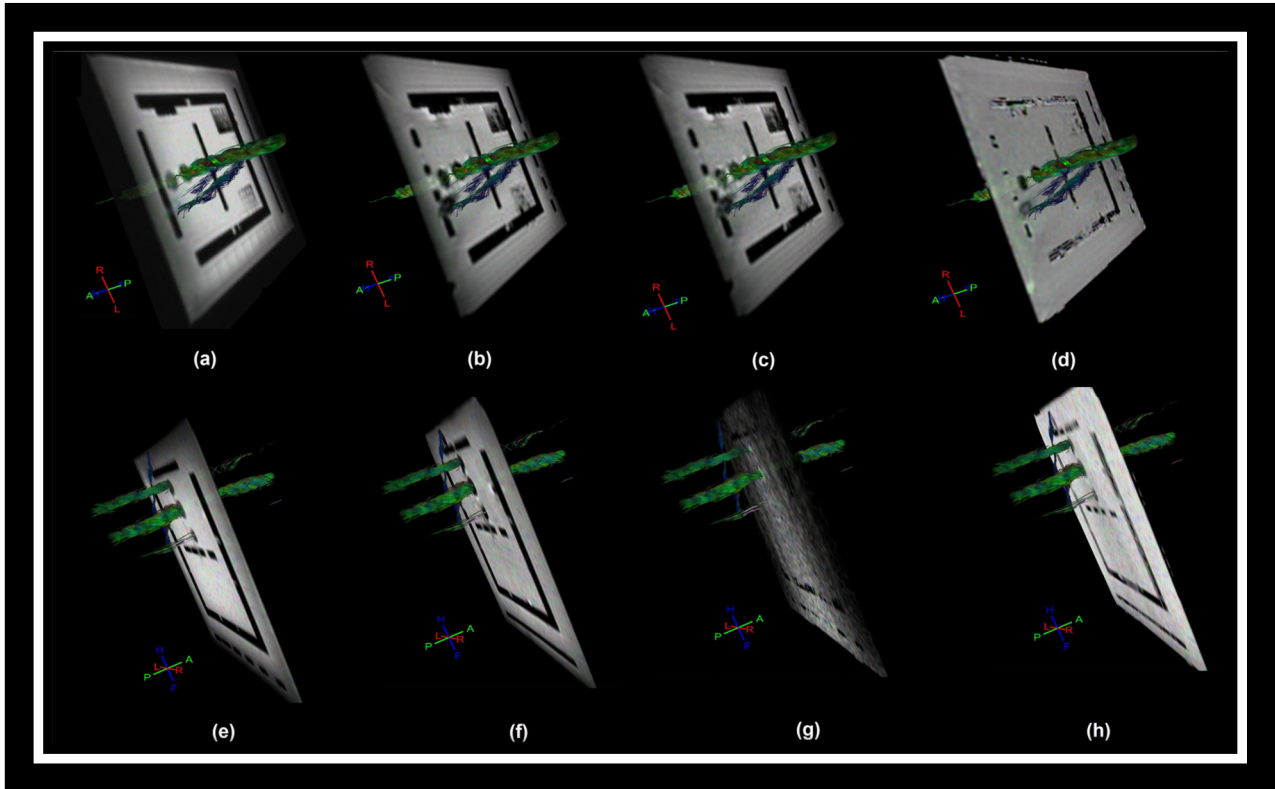
Figure 4.44 - Tracts reconstructed from multipurpose phantom DTI acquisitions. Top: acquisitions with b = 1000 s/mm^2. Bottom: acquisitions with b = 2500 s/mm^2. The tracts were co-registered with T1 images ((a) and (e)), T2 images ((b) and (f))), DW images ((c) and (g)), as well as ADC map ((d) and (h)).

Figure 4.44 shows the reconstructions of fibers for acquisitions with the multipurpose phantom. The fact that the phantom has many other modules does not interfere on DT images and their indices. So, the results found here show that it is possible to build a phantom with modules to evaluate many MRI modalities. The same logic explored here may be explored by researchers trying to develop multimodality MRI phantoms to evaluate, for example, the parameters checked here and spectroscopy, functional or angiographic parameters, as well as PET (Positron Emission Tomography) parameters, being the phantom applicable to PET/MRI scanners QC.

The right periodicity of DTI QC depends on characteristics of each scanner and on stability of DTI pulse sequences applied. However, based on results obtained in this study, it is suggested the weekly running of QC routines as proposed in Table 3.5. However, the pulse sequences and QC routines applied may be adjusted according clinical and/or research imaging acquisitions. Besides the QC of DTI, the phantom proposed is also rec-

ommended for training activities, to teach about diffusion imaging acquisition, processing and the evaluation of other MRI scanner performance aspects.

5 CONCLUSIONS AND FUTURE PERSPECTIVES

This work brings a study about materials and setups for the development of a multi-purpose phantom to evaluate the quality of DT images and other MRI scanner characteristics, such as SNR, spatial resolution, slice thickness and geometric distortions. It is known that there is no standard phantom or QC protocol for these images, which can be degraded by scanner hardware or by software instabilities before T1, T2 or PD images. To reach this aim, materials such as polyamide and Dyneema®, already explored in previous studies, were used to build fiber bundles simulating tracts found in neural and muscular tissues. In addition, materials not yet applied to build fiber phantoms were also explored, such as the multifilament Spectra® fishing lines and Kevlar® fishing lines. The compression of fibers in the bundles was done both using nylon cable ties or heat-shrinking tubes.

Standard QC MRI phantoms applied to T1, T2 and PD acquisitions, such as ACR phantoms, have diffusivities and relaxation parameters different from biological tissues and are isotropic. They can be helpful to follow parameters such as B_0 homogeneity, SNR, CNR, low-contrast structure detectability, uniformity, presence of ghost and distortions, slice thickness and spatial resolution of those images. However, DWI and DTI are more sensitive to bias compared to conventional MRI and consequently data corruption occurs first on these images. That is, when a problem is detected on T1, T2 and PD images, probably DW and DT images are already much degraded.

Although several studies have compared acquired phantom data with control subject or patient data, human or animal images should never be used as a QC tool for any imaging diagnostic technique. This is because unless body necropsy is done after scanning, the real organization and constitution of organs and tissues are unknown, as well as the patient's physiology.

In the first step of our study we verified how the acquisition parameters can change the DTIi, using CV values and analysis of correlation. The first phantom proposed consisted of an acrylic cylinder filled with distilled water where three Dyneema® fishing lines' fiber bundles are positioned in parallel. We found that this phantom could be possibly applied as a reference for checking DTIi over time. Although the phantom built in this step has a simplified design when compared to human brain tissues and their organization, it seems a good and stable DTI model. With this model, it was possible to define how the main DTI acquisition parameters can change DTIi. The fibers used have high anisotropy due to their

impermeability, which enables building of bundles to simulate axon fibers. However, only interstitial diffusion can be studied, given that water does not diffuse across the fibers, just between them. When compared to other phantoms found in literature, our device is cheaper, easier to build, and seems less susceptible to geometric distortions due to EPI, which should be considered in a 3T scanner. Microfabricated phantoms, based on microscopic representation of neurons and capillaries are good proposals to DTI QC. Nonetheless, as described, the B_0 distortions found with this sort of phantoms differ from those observed in human brain images. Furthermore, their MD and FA values are too far from those observed for human brain. It is known that different B_0 intensities and inhomogeneities, as well as pulse sequence parameters, lead to different kinds of B_1 distortions. Nonetheless, the main DTI measures (e.g. MD and FA) depend on phantom architecture and composition. Thus, if the phantom has a homogeneous composition, these measures should not vary significantly when changing acquisition protocols and/or B_0 intensity, considering images from single or multi-scanner studies.

The second step of our study brought the improvement of fiber bundles' characteristics, wrapping them using heat-shrinking tubes. Different materials and setups were tested, until reaching a stable and highly anisotropic configuration to simulate brain tracts. Besides Dyneema®, the fishing lines Kevlar®, Spectra® and polyamide were explored.

Given that Kevlar® is a material seemingly useful to build catheters for use in MRI, and Spectra® is a multifilament material with similar proprieties to Dyneema®, fishing lines of both were built and tested in DTI acquisitions. Kevlar® bundles did not show FA values compatible with those of biological tissues and were not reconstructed in most acquisitions. Despite the fact of Spectra® being a multifilament fiber such as Dyneema®, its handling is more difficult because these fibers have too much memory. Consequently, it is also more difficult to obtain Spectra® fiber bundles with high FA values, such as in the main human brain tracts. Kevlar®, on the other side, has less memory but a lower anisotropy level when compared to other materials. Polyamide, even for bundles with a higher number of fibers (400 to 500), also shows lower anisotropy levels, as expected. The FA and MD values, as well as the tracts appearance of Spectra® fiber bundles, suggest that these fishing lines can be useful to simulate cardiac muscle tissue. The good point is that both Kevlar® and Spectra® fishing lines do not generate imaging distortions and artifacts. So, they may also be suitable to build MRI phantoms.

On the other side, catheters and conduits lead to reduction of SNR in DW and DT images, being impossible to detect fiber tracts and consequently to calculate DTIi. This

occurs independently of NDGD. This kind of structures, even when it has lower diameters (of the order of mm), introduces macroscopic flux effects into images, leading to signal loss and artifacts.

All phantoms here proposed and tested were filled just with distilled water, given that water diffusion is the subject of study in DW and DT images. However, conventional MRI phantom fillings' solutions, such as $CuSO_4$, can improve the SNR and consequently the characterization of other MRI parameters tested by the multipurpose phantom. This kind of essay will be done in the future. Other kinds of solutions, such as n-tridecane-based solutions, have MD similar to brain WM. However, cyclic alkanes are toxic and flammable compounds, hindering their use in clinical routine. On the other side, sugar-based solutions, despite not being toxic, undergo biological degradation and are not useful for long-term follow-up scanning. The same goes for agarose gels, which are degraded despite the addition of anti-septic agents.

In all setups, to avoid air bubbles in the phantom, a syringe was used for inserting the distilled water in the container; also, remaining bubbles can be removed with a vacuum pump. It is important to look for and remove air bubbles to minimize magnetic susceptibility effects. Laundry detergent can remove bubbles, due to its ability to move them to the phantom surface, where they can be eliminated. Regardless of setup and materials applied to DWI and DTI phantoms, some advices can always be considered. First, phantoms filled by water are safer and easier to handle, besides taking a shorter time for thermal equilibrium in the scanner's room. Furthermore, distilled water does not lead to significant signal loss because its T1 and T2 values can match PD dephasing. It is important to watch out for effects of mechanical vibration of the scanner on liquids, which can lead to imaging distortions. For fiber phantoms, whenever possible the bundles should be aligned to **B_0**, avoiding magnetic susceptibility effects. Structural imaging techniques like microscopy and CT or microCT greatly contribute to the knowledge of internal structures of phantoms, identifying small fissures or misalignments.

The tests with the DTI multipurpose phantom show that it is possible to measure DTIi and other MRI parameters using just one device. In an imaging acquisition, total time of approximately 20 minutes it was possible to obtain information about slice thickness, spatial resolution, geometric distortion, SNR and the DTIi. The SNR value found was compatible with the application of the scanner in clinical routine. The SNR can also be measured just with the acrylic cylinder, without internal structures, filled by distilled water or even $CuSO_4$ based solutions. In this case is possible to calculate this parameter for all

slices of the image. Slice thickness and spatial resolution were compatible with the slice thickness and the voxel size of the imaging protocol. Acquisitions in all directions can be done to check these parameters for all slice orientations (axial, sagittal and coronal). Regarding geometric distortions, both plate of hole patterns and hole patterns of the DTI block can be useful to detect this problem.

The multipurpose phantom developed seems useful for low-cost and relatively fast QC of many MRI scanner parameters. The fiber bundles used showed FA values next to those found for the main brain tracts, which did not present high CV when the b-value was changed. From all the tested fishing lines, Dyneema® is the most suitable to build DTI phantoms, agreeing with results of previous studies using Dyneema® fibers (raw material) (11, 27). For these lines, DTIi are stable over time, for different bundles' length or orientation. Furthermore, this material has their lower memory when compared to others and consequently does not introduce any kind of artifacts in DT images.

To complete the validation of the multipurpose phantom, it is necessary to evaluate its performance for different MRI scanners, from different vendors and B_0 intensities. The multipurpose phantom for DTI QC can also be improved by the introduction of mechanical devices to simulate blood flow in veins and arteries, which can also degrade the DTI signal and consequently the DTIi.

Although imaging parameters' evaluation is generally the first thing thought of when talking about MRI QC, it is important to not forget other essential verifications which can avoid imaging damages and injuries to patients. Items to verify include patients' table integrity and motions, the communication systems, "panic button" given to the patient, RF room integrity and shielding (specially doors contacts and windows), emergency chart, safety lights and laser for positioning, MRI-compatible equipment for use in the scanner room, as well as all patient monitors. RF coils must also be checked for damages and cables' integrity. Burnout bulbs must not remain installed in the scanner's room, given that they can induce imaging artifacts. All the safety MRI protocol must also be applied during all the clinical and research routines.

Changes in DTI acquisition parameters can change de values of DTIi calculated. However, the phantom setup must be stable for all kinds of scanners, because DTIi variations detected must be more related to changes in performance characteristics of the MRI scanner than to the acquisition parameters, which can be purposely changed depending on what we want to see using different clinical protocols.

When compared to other DTI phantoms found in literature, this device has lower cost and its construction depends on acrylic structures and fishing lines, the latter being more readily available in shops than Dyneema®, Spectra®, or Kevlar® raw materials. The results obtained with Dyneema® fishing lines are better than those found for Dyneema® raw material of previous studies, because in this work fiber bundles lower than 10 mm diameter could be detected, while with raw material just bundles of higher diameter were detected and reconstructed.

Some authors say that it is impossible to build a multi-purpose MRI phantom (10). They are based on the fact that each technique requires specific structures and materials with T1 and T2 compatible to the studied parameter (e.g. SNR, slice thickness, FA and MD from DTI). However, the results reached in this study suggest that this statement is not be true.

The many modules of the phantom do not interfere significantly with the DT images and their indexes. So, the results found here show that it is possible to build a phantom with modules to evaluate many MRI modalities. The same logic explored here may be explored by researchers trying to develop multimodality MRI phantoms to evaluate, for example, the parameters checked here and also spectroscopy, functional or angiographic MRI scanner performance, as well as PET (Positron Emission Tomography) parameters, being the phantom applicable to PET/MRI scanners QC.

The heat-shrinking tubes are essential to ensure high anisotropy values. So, phantoms based on these bundles are useful for applications such as cross-calibration of DTIi, considering different protocols, or even different scanners, from different vendors, many B_0 values and or coils. The protocol for QC with the multipurpose phantom can be implemented in clinical routine. Furthermore, the device can be improved by implementation of structures that simulate blood flow inside vessels, which can interfere with DTI data. Tests with many scanners of different vendors and of different characteristics must also be done. Moreover, Dyneema® and/or Spectra® fishing lines based-bundles may also be important to simulate cardiac muscle fibers. In this case, less bundle compression is required when compared to brain tracts' simulations. The improvement of cardiac DTI QC will occur by developing a dynamic cardiac phantom based on flexible microstructures with controlled motions and fiber deformations according to real cardiac physiology. This configuration may be obtained by coupling bundles to a mechanical system connected to an electrocardiogram (ECG) simulator. Thus, it is possible to move the bundles at a specific cardiac frequency and at irregular frequencies, simulating the health and pathological cardiac

physiology at the scan time. To avoid motion artifacts, cardiac gating can be applied. Thus, a specific phase of the cardiac cycle can be chosen for image acquisition. In general, gating increases the scan time, but improves the SNR and avoids imaging geometric distortions. For acquisition of patients' data, respiratory and cardiac gating can minimize thorax motion effects.

5.1 SCIENTIFIC PUBLICATIONS FROM THIS WORK

This section brings the references of scientific publications originating from this study.

5.1.1 Scientific Articles

➢ Souza EM, Costa ET, Castellano G. Phantoms for Diffusion-Weighted Imaging and Diffusion Tensor Imaging Quality Control: A Review and New Perspectives. Submitted to Research on Biomedical Engineering (waiting for publication).

➢ Souza EM, Costa ET, Castellano G. How the MRI Acquisition Parameters Changes the DTI Indices? A Fiber-Phantom Study. In preparation for submission to MAGMA (Magnetic Resonance Materials in Medicine and Biology).

5.1.2 Conference Papers

➢ Souza EM, Costa ET, Castellano G. Estudo da Estabilidade de um Phantom para o Controle de Qualidade de Imagens do Tensor de Difusão. XXV Congresso Brasileiro de Engenharia Biomédica (CBEB-2016), October 2016, Foz do Iguaçu-PR, Brazil. Páginas: 1111-1114. https://drive.google.com/drive/folders/0B543adcG1FClQ21ZaFhCUmdwMlk

➢ Souza EM, Costa ET, Castellano G, et al. Estudo Preliminar Visando o Desenvol-vimento de um Protocolo de Controle de Qualidade em DTI. XXIV Congresso Brasi-leiro de Engenharia Biomédica (CBEB-2014), Uberlândia-MG, Brazil. Páginas: 2306-2309. http://www.canal6.com.br/cbeb/2014/index.html

5.1.3 Conference Abstracts

- Souza EM, Costa ET, Castellano G. The Use of Dyneema Fiber Phantom for DTI Quality Control: Influence of Imaging Acquisition Parameters on DTI Indexes. Jour-nal of Epilepsy and Clinical Neurophysiology, 2015, 22(3):106-17 3th BRAINN Con-gress, April 2016, Campinas-SP, Brazil.

- Souza EM, Costa ET, Castellano G, et al. Quality Control of Diffusion Tensor Imag-es: Preliminary Results. Journal of Epilepsy and Clinical Neurophysiology, 2015, 21(2):46. 2th BRAINN Congress, April 2015, Campinas-SP, Brazil.

REFERENCES

1.   Moseley ME, Cohen Y, Mintorovitch J, Chileuitt L, Shimizu H, Kucharczyk J, et al. Early detection of regional cerebral ischemia in cats: comparison of diffusion- and T2-weighted MRI and spectroscopy. Magn Reson Med. 1990;14(2):330-46.

2.   Stejskal EO. Use of Spin Echoes in a Pulsed Magnetic‑Field Gradient to Study Anisotropic, Restricted Diffusion and Flow. 1965.

3.   Bammer R. Basic principles of diffusion-weighted imaging. Eur J Radiol. 2003;45(3):169-84.

4.   Basser P. New histological and physiological stains derived from diffusion-tensor MR images. Ann NY Acad Sci. 1997;820:123-38.

5.   Mori S, Crain BJ, Chacko VP, van Zijl PC. Three-dimensional tracking of axonal projections in the brain by magnetic resonance imaging. Ann Neurol. 1999;45(2):265-9.

6.   Budzik JF, Balbi V, Verclytte S, Pansini V, Le Thuc V, Cotten A. Diffusion tensor imaging in musculoskeletal disorders. Radiographics. 2014;34(3):E56-72.

7.   Poveda F, Gil D, Marti E, Andaluz A, Ballester M, Carreras F. Helical structure of the cardiac ventricular anatomy assessed by diffusion tensor magnetic resonance imaging with multiresolution tractography. Rev Esp Cardiol (Engl Ed). 2013;66(10):782-90.

8.   Oudeman J, Nederveen AJ, Strijkers GJ, Maas M, Luijten PR, Froeling M. Techniques and applications of skeletal muscle diffusion tensor imaging: A review. J Magn Reson Imaging. 2015.

9.   Le Bihan D, Poupon C, Amadon A, Lethimonnier F. Artifacts and pitfalls in diffusion MRI. J Magn Reson Imaging. 2006;24(3):478-88.

10.   Hellerbach A, Schuster V, Jansen A, Sommer J. MRI phantoms - are there alternatives to agar? PLoS One. 2013;8(8):e70343.

11.   Fieremans E. Simulation and experimental verification of the diffusion in an anisotropic fiber phantom. 2008;190(2):189–99.

12.   Hubbard PL, Zhou FL, Eichhorn SJ, Parker GJ. Biomimetic phantom for the validation of diffusion magnetic resonance imaging. Magn Reson Med. 2014.

13.   Teh I, Zhou FL, Hubbard Cristinacce PL, Parker GJ, Schneider JE. Biomimetic Phantom for Cardiac Diffusion MRI. J Magn Reson Imaging. 2015.

14.   DeWerd L, M L. Introduction to Phantoms of Medical and Health Physics. In: DeWerd L, Kissick M, editors. The Phantoms of Medical and Health Physics: Devices for Research and Development. 1. 1 ed. New York, USA: Springer Science + Bussiness; 2014. p. 1-14.

15.   Phantomlab.   Catphan   Phantoms   2017   [Available   from: https://www.phantomlab.com/catphan-phantoms/.

16.   RADIOLOGY ACO. ACR Mammography Accreditation 2017 [Available from: http://www.acraccreditation.org/modalities/mammography.

17.   Bhd HAMSS. Fetal Ultrasound Biometrics Phantom - H&A Medical Supply Sdn Bhd 2017 [Available from: http://www.hnamedical.com/product/radiology/phantoms-cirs/fetal-ultrasound-biometrics-phantom/.

18.   Devices RS, ART. RANDO ANTHROPOMORPHIC PHANTOM 2017 [Available from: http://www.rsdphantoms.com/rt_art.htm.

19.   RADIOLOGY ACO. MRI PHANTOMS FOR ACCREDITATION 2017 [Available from: https://www.acr.org/~/media/ACR%20No%20Index/Documents/QC%20Manual/2015_MR_QCManual_Book.pdf.

20.   Gunter JL, Bernstein MA, Borowski BJ, Ward CP, Britson PJ, Felmlee JP, et al.

Measurement of MRI scanner performance with the ADNI phantom. Med Phys. 2009;36(6):2193-

205.

21.   Kato H, Kuroda M, Yoshimura K, Yoshida A, Hanamoto K, Kawasaki S, et al. Composition of MRI phantom equivalent to human tissues. Med Phys. 2005;32(10):3199-208.
22.   Madsen EL, Fullerton GD. Prospective tissue-mimicking materials for use in NMR imaging phantoms. Magn Reson Imaging. 1982;1(3):135-41.
23.   Tofts PS, Lloyd D, Clark CA, Barker GJ, Parker GJ, McConville P, et al. Test liquids for quantitative MRI measurements of self-diffusion coefficient in vivo. Magn Reson Med. 2000;43(3):368-74.
24.   Pierpaoli C, Sarlls U, Nevo PJ, Basser P, Horkay F, editors. Polyvinylpyrrolidone (PVP) water solutions as isotropic phantoms for diffusion MRI studies. ISMRM 17th Annual Meeting and Exhibition; 2009; Honolulu, Hawaii.
25.   Lavdas I, Behan KC, Papadaki A, McRobbie DW, Aboagye EO. A phantom for diffusion-weighted MRI (DW-MRI). J Magn Reson Imaging. 2013;38(1):173-9.
26.   Laubach HJ, Jakob PM, Loevblad KO, Baird AE, Bovo MP, Edelman RR, et al. A phantom for diffusion-weighted imaging of acute stroke. J Magn Reson Imaging. 1998;8(6):1349-54.
27.   Lorenz R, Kreher BW, Henning J, . PoItSM. Anisotropic Fiber Phantom for DTI validation on a clinical scanner. ISMRM 14th Scientific Meeting; Seattle, USA2006. p. 1226.
28.   Ebrahimi B, Swanson SD, Chupp TE. A microfabricated phantom for quantitative MR perfusion measurements: validation of singular value decomposition deconvolution method. IEEE Trans Biomed Eng. 2010;57(11).
29.   Latt J, Nilsson M, Rydhog A, Wirestam R, Stahlberg F, Brockstedt S. Effects of restricted diffusion in a biological phantom: a q-space diffusion MRI study of asparagus stems at a 3T clinical scanner. Magma. 2007;20(4):213-22.
30.   Komlosh ME, Lizak MJ, Horkay F, Freidlin RZ, Basser PJ. Observation of microscopic diffusion anisotropy in the spinal cord using double-pulsed gradient spin echo MRI. Magn Reson Med. 2008;59(4):803-9.
31.   Chen H, Zhao Y, Zhang T, Zhang H, Kuang H, Li M, et al. Construct and assess multimodal mouse brain connectomes via joint modeling of multi-scale DTI and neuron tracer data. Med Image Comput Comput Assist Interv. 2014;17(Pt 3):273-80.
32.   Wang ZJ, Seo Y, Chia JM, Rollins NK. A quality assurance protocol for diffusion tensor imaging using the head phantom from American College of Radiology. Med Phys. 2011;38(7):4415-21.
33.   Leemans A, Sijbers J, Verhoye M, Van der Linden A, Van Dyck D. Mathematical framework for simulating diffusion tensor MR neural fiber bundles. Magn Reson Med. 2005;53(4):944-53.
34.   Ihalainen TM, Lonnroth NT, Peltonen JI, Uusi-Simola JK, Timonen MH, Kuusela LJ, et al. MRI quality assurance using the ACR phantom in a multi-unit imaging center. Acta Oncol. 2011;50(6):966-72.
35.   Boursianis T, Kalaitzakis G, Veneti S, Pappas E, Damilakis J, Maris TG. MRI Diffusion measurements on phantoms: comparison between EPI and HASTE sequences utilizing two fitting methods in Apparent Diffusion Coefficient (ADC) measurements. 2014;30:e50.
36.   Gatidis S, Schmidt H, Martirosian P, Schwenzer NF. Development of an MRI phantom for diffusion-weighted imaging with independent adjustment of apparent diffusion coefficient values and T2 relaxation times. Magn Reson Med. 2014;72(2):459-63.
37.   Komlosh ME, Ozarslan E, Lizak MJ, Horkay F, Schram V, Shemesh N, et al. Pore diameter mapping using double pulsed-field gradient MRI and its validation using a novel glass capillary array phantom. J Magn Reson. 2011;208(1):128-35.
38.   Lorenz R, Kreher, B.W. & Hennig, J. Anisotropic Phantoms for Quantitative Diffusion Tensor Imaging and Fib. Proceedings of ISMRM 14th Scientific Meeting Seattle, USA. 2006.
39.   Lavdas I, Miquel ME, McRobbie DW, Aboagye EO. Comparison between diffusion-weighted MRI (DW-MRI) at 1.5 and 3 tesla: a phantom study. J Magn Reson Imaging.

2014;40(3):682-90.

40.   Kim SJ, Choi CG, Kim JK, Yun SC, Jahng GH, Jeong HK, et al. Effects of MR parameter changes on the quantification of diffusion anisotropy and apparent diffusion coefficient in diffusion tensor imaging: evaluation using a diffusional anisotropic phantom. Korean J Radiol. 2015;16(2):297-303.

41.   Lee W, Lee SD, Park MY, Foley L, Purcell-Estabrook E, Kim H, et al. Functional and diffusion tensor magnetic resonance imaging of the sheep brain. BMC Vet Res. 2015;11.

42.   Widjaja E, Mahmoodabadi SZ, Rea D, Moineddin R, Vidarsson L, Nilsson D. Effects of gradient encoding and number of signal averages on fractional anisotropy and fiber density index in vivo at 1.5 tesla. Acta Radiol. 2009;50(1):106-13.

43.   Qin W, Yu CS, Zhang F, Du XY, Jiang H, Yan YX, et al. Effects of echo time on diffusion quantification of brain white matter at 1.5 T and 3.0 T. Magn Reson Med. 2009;61(4):755-60.

44.   Melhem ER, Itoh R, Jones L, Barker PB. Diffusion tensor MR imaging of the brain: effect of diffusion weighting on trace and anisotropy measurements. AJNR Am J Neuroradiol. 2000;21(10):1813-20.

45.   Pruessmann KP, Weiger M, Scheidegger MB, Boesiger P. SENSE: sensitivity encoding for fast MRI. Magn Reson Med. 1999;42(5):952-62.

46.   Leemans A JB, Sijbers J, and Jones DK, editor ExploreDTI: a graphical toolbox for processing, analyzing, and visualizing diffusion MR data. 17th Annual Meeting of Intl Soc Mag Reson Med; 2009; Hawaii, USA.

47.   Tournier JD, Mori S, Leemans A. Diffusion tensor imaging and beyond. Magn Reson Med. 2011;65(6):1532-56.

48.   Mori S, Tournier J. Introduction to Diffusion Tensor Imaging and Higher Order Models. second edition ed: Elsevier Science; 2014.

49.   Corporation F. Fluke Biomedical 1995-2017 [

50.   Andersen AH. On the Rician distribution of noisy MRI data. Magn Reson Med. 1996;36(2):331-3.

51.   Wiggins GC, Polimeni JR, Potthast A, Schmitt M, Alagappan V, Wald LL. 96-Channel Receive-Only Head Coil for 3 Tesla: Design Optimization and Evaluation. Magn Reson Med. 2009;62(3):754-62.

52.   Dietrich O, Raya JG, Reeder SB, Reiser MF, Schoenberg SO. Measurement of signal-to-noise ratios in MR images: influence of multichannel coils, parallel imaging, and reconstruction filters. J Magn Reson Imaging. 2007;26(2):375-85.

53.   Jones DK, Cercignani M. Twenty-five pitfalls in the analysis of diffusion MRI data. NMR Biomed. 2010;23(7):803-20.

54.   Teipel SJ, Reuter S, Stieltjes B, Acosta-Cabronero J, Ernemann U, Fellgiebel A, et al. Multicenter stability of diffusion tensor imaging measures: a European clinical and physical phantom study. Psychiatry Res. 2011;194(3):363-71.

55.   Landman BA, Farrell JA, Jones CK, Smith SA, Prince JL, Mori S. Effects of diffusion weighting schemes on the reproducibility of DTI-derived fractional anisotropy, mean diffusivity, and principal eigenvector measurements at 1.5T. Neuroimage. 2007;36(4):1123-38.

56.   Ni H, Kavcic V, Zhu T, Ekholm S, Zhong J. Effects of number of diffusion gradient directions on derived diffusion tensor imaging indices in human brain. AJNR Am J Neuroradiol. 2006;27(8):1776-81.

57.   Papanikolaou N, Karampekios S, Papadaki E, Malamas M, Maris T, Gourtsoyiannis N. Fractional anisotropy and mean diffusivity measurements on normal human brain: comparison between low-and high-resolution diffusion tensor imaging sequences. Eur Radiol. 2006;16(1):187-92.

58.   Bennett IJ, Madden DJ, Vaidya CJ, Howard DV, Howard JH. Age-Related Differences in Multiple Measures of White Matter Integrity: A Diffusion Tensor Imaging Study of Healthy Aging.

Hum Brain Mapp. 2010;31(3):378-90.

59.   Yoshida S, Oishi K, Faria AV, Mori S. Diffusion tensor imaging of normal brain development. Pediatr Radiol. 2013;43(1):15-27.

60.   Qin X, Wang S, Shen M, Zhang X, Wagner MB, Fei B. Mapping Cardiac Fiber Orientations from High-Resolution DTI to High-Frequency 3D Ultrasound. Proc SPIE. 2014;9036:90361O.

61.   Perge JA, Niven JE, Mugnaini E, Balasubramanian V, Sterling P. Why do axons differ in caliber? J Neurosci. 2012;32(2):626-38.

62.   Fushimi Y, Miki Y, Okada T, Yamamoto A, Mori N, Hanakawa T, et al. Fractional anisotropy and mean diffusivity: comparison between 3.0-T and 1.5-T diffusion tensor imaging with parallel imaging using histogram and region of interest analysis. NMR Biomed. 2007;20(8):743-8.

63.   Santarelli X, Garbin G, Ukmar M, Longo R. Dependence of the fractional anisotropy in cervical spine from the number of diffusion gradients, repeated acquisition and voxel size. Magn Reson Imaging. 2010;28(1):70-6.

64.   Giannelli M, Cosottini M, Michelassi MC, Lazzarotti G, Belmonte G, Bartolozzi C, et al. Dependence of brain DTI maps of fractional anisotropy and mean diffusivity on the number of diffusion weighting directions. J Appl Clin Med Phys. 2009;11(1):2927.

65.   Alexander AL, Lee JE, Wu YC, Field AS. Comparison of diffusion tensor imaging measurements at 3.0 T versus 1.5 T with and without parallel imaging. Neuroimaging Clin N Am. 2006;16(2):299-309, xi.

66.   Jones DK, Basser PJ. "Squashing peanuts and smashing pumpkins": how noise distorts diffusion-weighted MR data. Magn Reson Med. 2004;52(5):979-93.

67.   Huisman TA, Loenneker T, Barta G, Bellemann ME, Hennig J, Fischer JE, et al. Quantitative diffusion tensor MR imaging of the brain: field strength related variance of apparent diffusion coefficient (ADC) and fractional anisotropy (FA) scalars. Eur Radiol. 2006;16(8):1651-8.

68.   American College of Radiology. ACR 2015 [Available from: http://www.acr.org/.

69.   American Association of Physicists in Medicine. AAPM 2015 [Available from: http://www.aapm.org/.

70.   Weavers PT, Shu Y, Tao S, Huston J, 3rd, Lee SK, Graziani D, et al. Technical Note: Compact three-tesla magnetic resonance imager with high-performance gradients passes ACR image quality and acoustic noise tests. Med Phys. 2016;43(3):1259-64.

71.   Toussaint N, London KsC, INRIA ARG, nicolas.toussaint@kcl.ac.uk, Sermesant M, London KsC, et al. In vivo Human 3D Cardiac Fibre Architecture: Reconstruction Using Curvilinear Interpolation of Diffusion Tensor Images. 2015:418-25.